

# Low phonon energy glass ceramics for efficient rare-earth luminescence

## Dissertation

zur Erlangung des akademischen Grades

*doctor rerum naturalium (Dr. rer. nat.)*

vorgelegt dem

Institut für Physik  
der Naturwissenschaftlichen Fakultät II  
der Martin-Luther-Universität Halle-Wittenberg

von Frau Dipl.-Phys. Charlotte Pfau  
geboren am 29. Dezember 1982 in Halle

Gutachter

1. Prof. Dr. S. Schweizer, Fachhochschule Südwestfalen
2. Prof. Dr. R. Wehrspohn, Martin-Luther-Universität Halle-Wittenberg
3. Prof. Dr. U. Rogulis, University of Latvia

eingereicht am 31. Juli 2014  
verteidigt am 13. November 2014

*It is not because things are difficult that we  
do not dare, it is because we do not dare that  
they are difficult.*

Lucius Annaeus Seneca

# Contents

<b>1. Introduction</b>	<b>1</b>
<b>2. Fundamentals</b>	<b>5</b>
2.1. Rare-earth luminescence . . . . .	5
2.1.1. Optical transitions in rare-earth ions . . . . .	5
2.1.2. Luminescence efficiency and competing mechanisms . . . . .	7
2.2. Multiphonon relaxation . . . . .	9
2.2.1. Theory of multiphonon processes . . . . .	9
2.2.2. Low phonon materials . . . . .	11
2.2.3. Vibrational properties . . . . .	13
<b>3. Methods</b>	<b>15</b>
3.1. Raman spectroscopy and phonon spectra calculations . . . . .	15
3.1.1. Raman spectroscopy . . . . .	15
3.1.2. First principles calculations . . . . .	18
3.2. Time-resolved and spectrally-resolved photoluminescence . . . . .	19
3.2.1. Photoluminescence experiments . . . . .	19
3.2.2. Generation of selective laser pulses . . . . .	20
3.2.3. Data acquisition and photon counting . . . . .	21
3.3. Additional experimental techniques . . . . .	23
3.3.1. Differential scanning calorimetry . . . . .	23
3.3.2. X-ray diffraction . . . . .	23
3.3.3. Mössbauer spectroscopy . . . . .	24
3.3.4. Transmission spectroscopy . . . . .	25
3.3.5. Absolute quantum yield determination . . . . .	25
<b>4. Crystallization processes in rare-earth doped glasses</b>	<b>27</b>
4.1. Composition and synthesis of fluorozirconate-based glasses . . . . .	27
4.2. Thermal treatment and structural analysis . . . . .	28
4.3. Influence of the rare-earth ions on the crystallization . . . . .	34
<b>5. Investigations on luminescence properties and relaxation dynamics</b>	<b>37</b>
5.1. Spectroscopic properties of Nd <sup>3+</sup> . . . . .	38
5.2. Luminescence enhancement . . . . .	43
5.3. Luminescence decay times . . . . .	46
5.4. Luminescence rise times . . . . .	51
5.5. Temperature dependence of the decay rates . . . . .	54

<b>6. Experimental and theoretical investigations on vibrational spectra</b>	<b>57</b>
6.1. Raman spectra of the glasses and glass ceramics . . . . .	57
6.2. Comparison of BaCl <sub>2</sub> nanocrystals and bulk BaCl <sub>2</sub> . . . . .	58
6.3. Calculated phonon spectra . . . . .	60
6.4. Mode assignment and structural phase transitions . . . . .	62
6.5. Consideration of all optical phonon modes . . . . .	64
6.6. Analysis of the glass-related Raman bands . . . . .	67
6.7. Influence of rare-earth ions on the phonon spectra . . . . .	69
<b>7. Investigation of the oxidation state of rare-earth ions:</b>	
<b>a Mössbauer study</b>	<b>71</b>
7.1. Optimization of Eu-doped glasses and glass ceramics . . . . .	71
7.2. Temperature dependence of the Mössbauer spectra . . . . .	75
<b>8. Discussion</b>	<b>79</b>
8.1. Nanocrystal formation and vibrational spectra . . . . .	79
8.2. Interaction of rare-earth ions with BaCl <sub>2</sub> nanocrystals and effect of their structural phase and size . . . . .	81
8.3. Comparison and energy gap dependence of the multiphonon relaxation rates . . . . .	87
8.4. Quantum efficiencies . . . . .	90
<b>9. Conclusion and outlook</b>	<b>95</b>
<b>Bibliography</b>	<b>99</b>
<b>A. Publications</b>	<b>107</b>
<b>B. Acknowledgment</b>	<b>111</b>
<b>C. Curriculum vitae</b>	<b>113</b>
<b>D. Declaration</b>	<b>115</b>

# 1. Introduction

Since the beginning of the investigations on complex rare-earth luminescence spectra in the 1860s [1], rare-earth doped crystals and glasses have been employed as active media in various kinds of conventional luminescence and frequency converting devices. They are typically used as laser gain media [2, 3] and for ionizing radiation detection [4, 5]. Quite recently rare-earth doped materials also attracted interest for photovoltaic applications, namely as upconverting bottom layers for bifacial silicon solar cells, which can improve solar cell efficiencies by converting infrared (IR) subbandgap photons of the solar spectrum into visible (VIS) photons useable for electrical power generation [6, 7]. Figure 1.1(a) shows the upconverted luminescence in an  $\text{Er}^{3+}$ -doped fluorozirconate (FZ) glass under IR excitation [8].

Glassy rare-earth hosts offer significant advantages over crystals. Their production is less challenging and their achievable size is not limited. For instance, large-area glass plates which can be attached to solar cells would be conceivable. Furthermore, they can be drawn into fibers making many luminescence and laser applications such as rare-earth doped fiber amplifiers possible. As a representative example, an  $\text{Yb}^{3+}$ -doped fiber amplifier is shown in Figure 1.1(b) [9]. However, the best radiative emission quantum efficiencies of rare-earth ions are usually obtained with crystalline host materials, but single crystals are very expensive and polycrystalline media cause scattering losses. Recently, glass ceramics became subject of research interest, being used as alternative host materials that combine the advantages of glasses with the beneficial luminescence properties of crystals [10]. In Refs. [11, 12] it was shown that  $\text{Eu}^{2+}$ -doped transparent fluorochlorozirconate (FCZ) glass ceramics used as X-ray scintillators or storage phosphors provide superior resolution as compared to competing polycrystalline materials owing to lower light scattering. Figure 1.1(c) presents an X-ray scintillation image recorded with such an  $\text{Eu}^{2+}$ -doped FCZ glass ceramic [11].

The present work also deals with FCZ glasses and glass ceramics. FCZ glass ceramics have been developed in the 2000s by the groups of Schweizer, Johnson, and Williams [11, 13, 14]; they have already been proven to be suitable host materials for  $\text{Eu}^{2+}$ . These FZ-based hosts belong to the class of heavy metal fluoride glasses, which was discovered in 1974 by Poulain *et al.* [15]. FZ-based glasses provide high transparency from the near ultraviolet (UV) up to  $7\ \mu\text{m}$  [16] and low maximum phonon energies of about  $600\ \text{cm}^{-1}$  [17] (for convenience given in wavenumbers). The FCZ glass formulation is close to the well-known ZBLAN composition [18], but some fluorides are substituted by chlorides, which

## 1. Introduction

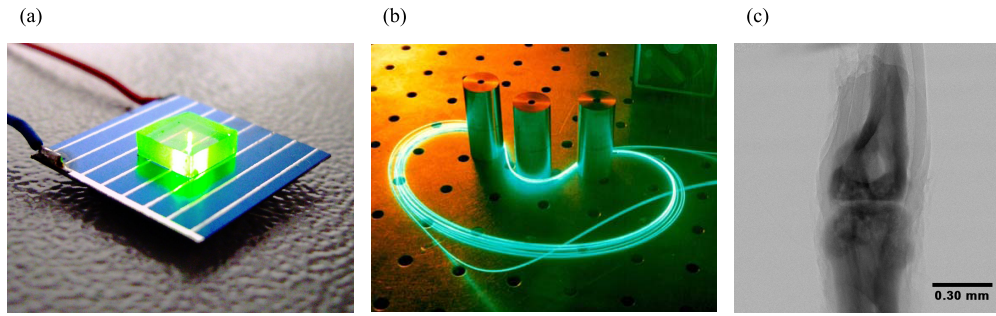


Figure 1.1.: Different applications of rare-earth doped glasses and glass ceramics. (a) Upconverted photoluminescence in an  $\text{Er}^{3+}$ -doped FZ glass excited with an IR laser diode [8], (b)  $\text{Yb}^{3+}$ -doped glass fiber amplifier [9], and (c) scintillation image of a mouse joint recorded with an  $\text{Eu}^{2+}$ -doped FZ-based glass ceramic [11].

initiate the formation of  $\text{BaCl}_2$  nanocrystals within the glass and hence a ceramization upon appropriate thermal processing. The FCZ glass ceramics exhibit mechanical properties similar to ZBLAN glasses [19].  $\text{Eu}^{2+}$ -doped FCZ glass ceramics have been intensively researched [20, 11, 12, 21, 22, 23], because of their high potential for medical imaging applications. It was shown that the growth of the  $\text{BaCl}_2$  nanocrystals results in a strong  $\text{Eu}^{2+}$  luminescence when excited accordingly, which is related to an incorporation of  $\text{Eu}^{2+}$  into the  $\text{BaCl}_2$  nanocrystals [20]. Depending on the annealing conditions the crystallites formed have sizes between about 10 and 100 nm and crystallize either in the orthorhombic (space group  $Pnma$  [24]) or hexagonal (space group  $P\bar{6}2m$  [25]) structure of  $\text{BaCl}_2$ .

It was also possible to induce the growth of hexagonal  $\text{BaCl}_2$  nanocrystals in  $\text{Nd}^{3+}$ -doped FCZ glasses [26]. In Ref. [26] it was shown that this nanocrystal formation leads to enhanced upconverted  $\text{Nd}^{3+}$  photoluminescence (PL). However, the mechanism behind this PL enhancement for trivalent rare-earth ions was not further analyzed. A major luminescence quenching mechanism of trivalent rare-earth ions, especially in glass hosts, is multiphonon relaxation (MPR). It is important to use low phonon energy materials as rare-earth hosts in order to reduce nonradiative losses by MPR. Although FZ glasses are among the glasses with the lowest phonon energies (maximum phonon energy  $\hbar\omega_{\max} \approx 600 \text{ cm}^{-1}$ ), the MPR rates in FZ glasses are for most rare-earth levels at least two orders of magnitude higher than the radiative decay rates of typical  $4f-4f$  transitions in rare-earth ions [27, 28]. Whereas MPR was intensively studied and is well understood in crystals and glasses [29, 30, 31, 32, 27], comparable investigations about MPR in glass ceramics do not exist.

The aim of this thesis is to investigate FCZ glass ceramics as alternative rare-earth host materials in order to be able to optimize them in terms of two different applicational aspects. The first task is to examine the influence of the  $\text{BaCl}_2$  nanocrystals, also in dependence on their phase and size, on the PL properties of trivalent rare-earth ions. Secondly, the oxidation state of embedded

rare-earth ions, which is important for X-ray luminescence (XL)-based medical imaging applications of these glass ceramics, is investigated. For the former purpose, a series of  $\text{Nd}^{3+}$ -doped glasses and glass ceramics is prepared and characterized in the framework of this work (Chapter 4). Effects of luminescence enhancement and related rare-earth relaxation dynamics are examined by time-resolved PL spectroscopy of optical transitions between different rare-earth levels (Chapter 5). The MPR properties, which are basically determined by the rare-earth host material, play an important role here.  $\text{Nd}^{3+}$  is investigated as a model rare-earth ion, since it is particularly suitable for the estimation of MPR rates of various rare-earth electronic levels. The dependence of the MPR rate on the energy gap to the next lower level is investigated as well. An exponential dependence on the energy gap was found for various glasses and crystals [32]. This work answers whether a comparable “energy gap law” exists for the FCZ glass ceramics studied.

In this context, the phonon spectra of the different samples are also investigated (Chapter 6), because the phonon energy of the rare-earth host material has a significant influence on the MPR rates of the rare-earth levels and hence may determine their luminescence efficiencies. Not only the phonon spectra of the base glasses are of interest in this respect, but also those of the nanocrystals protected by the embedding glass matrix. Raman data of  $\text{BaCl}_2$  crystals are rare in literature due to their sensitivity to atmospheric moisture. Thus, there is also fundamental interest in the phonon spectra of these crystals, in particular because the phonon spectra of the occurring metastable hexagonal phase of  $\text{BaCl}_2$ , which cannot be grown as a bulk crystal [33], were not investigated until now. Additionally, the influence of the crystallite size on the phonon spectra is explored. Besides Raman measurements, an *ab initio* study is performed in order to examine whether it is possible to predict the phonon spectra of the different structural phases of  $\text{BaCl}_2$  from density functional theory (DFT) calculations.

Concerning the oxidation state of rare-earth ions it should be noted that Eu occurs in a trivalent as well as in a divalent valence state in solids contrary to most rare-earths. For the use of Eu-doped FCZ glass ceramics as X-ray storage phosphors or scintillators, it is important to avoid the oxidation of  $\text{Eu}^{2+}$  into  $\text{Eu}^{3+}$ ;  $\text{Eu}^{2+}$  shows a strong luminescence upon X-ray excitation. To develop further these materials, Mössbauer spectroscopy is evaluated as a method to determine the  $\text{Eu}^{2+}$ -to- $\text{Eu}^{3+}$  ratio. Furthermore, routes to maximize the divalent Eu content are investigated (Chapter 7).

The physical background and the different experimental and theoretical methods used for this work are introduced in Chapter 2 and 3, respectively. The results presented and analyzed in Chapters 4-7 are discussed in a wider context in Chapter 8. Chapter 9 summarizes the main results of this thesis and gives an outlook for future work.



## 2. Fundamentals

The luminescence properties of rare-earth doped solids depend on various factors. Besides the radiative transition probabilities, interactions of the rare-earth ions among themselves and interactions between the rare-earth ions and the embedding matrix play an important role. For the quantum efficiency optimization of the considered glassy hosts, MPR is a crucial process but controllable process. Since the vibrational properties of the host material determine the rates of MPR losses, they have a significant influence on the luminescence efficiency of the embedded rare-earth ions. This chapter is organized as follows: After a general description of optical transitions in rare-earth ions, the different processes and loss mechanisms that influence the luminescence efficiency are discussed. Subsequently, the basic theory of MPR and the corresponding physical dependencies are presented. At the end of this chapter, the basic physics of vibrations in solids are briefly reviewed.

### 2.1. Rare-earth luminescence

#### 2.1.1. Optical transitions in rare-earth ions

The rare-earths of interest for luminescence applications are the elements of the sixth row of the periodic table with the atomic number varying from 58 (cerium) to 70 (ytterbium). They are characterized by an incompletely filled  $4f$  shell that is shielded by completely filled  $5s^2$  and  $5p^6$  shells. When incorporated into solid hosts, they occur as trivalent, or occasionally as divalent rare-earth ions. Trivalent rare-earths provide interesting luminescence spectra: They exhibit a large number of narrow emission bands covering a wide spectral range from the near UV into the near IR (NIR). Also some divalent rare-earth ions (notably  $\text{Sm}^{2+}$  and  $\text{Eu}^{2+}$ ) exhibit luminescence emissions bands. Figure 2.1 gives an overview on energy levels of trivalent rare-earth ions in crystalline  $\text{LaF}_3$  arranged according to the number  $n$  of  $4f$  electrons ranging from  $n = 1$  (cerium) to  $n = 13$  (ytterbium).

Luminescence from excited trivalent rare-earth ions is caused by radiative transitions between these levels of the  $4f^n$  shell. The spectral positions of the levels arise from a combination of the electrostatic interaction between the carriers, the spin-orbit interaction and the interaction with the crystal field of the environment. The free ion interactions (i.e. all interactions except from the crystal field interaction) yields a set of degenerated terms with the spectroscopic



relatively insensitive to the kind of host material in which they are incorporated.

Electric dipole transitions between  $4f$  states are parity forbidden. However, in most hosts, intra- $4f$  electric dipole transitions of rare-earth ions are observed; they become partially allowed since the crystal field admixes states of opposite parity into the  $4f$  levels [35]. Thus, the crystal field determines the strength of the radiative transitions. Nevertheless, the transition probabilities are low and hence luminescence lifetimes are relatively long (usually  $10^{-6}$  to  $10^{-3}$  s) and the corresponding linewidths are narrow.

The radiative transition probabilities of intra- $4f$  transitions can be obtained by using Judd-Ofelt theory [36, 37]. This theory states that the oscillator strength of a  $4f$ - $4f$  transition can be calculated by a set of three phenomenological host parameters (the Judd-Ofelt parameters) when the quantum states (basically determined by the  $4f^n$  configuration and the quantum numbers  $L$ ,  $S$  and  $J$ ) of the initial and the final level are known. Physically, the Judd-Ofelt parameters completely describe the influence of the crystal field of a particular host on the transition probabilities of intra- $4f$  transitions. These host parameters can be determined by experimental means (e.g. from absorption spectra) or they can be directly calculated when the rare-earth ions occupy a low symmetry site. Once these three parameters are known for a certain rare-earth ion in a given host, the radiative absorption and emission probabilities can be estimated for any pair of levels. The Judd-Ofelt parameters of most host materials are tabulated in the literature.

### 2.1.2. Luminescence efficiency and competing mechanisms

Besides low radiative transition probabilities, various quenching mechanisms can lead to low rare-earth luminescence efficiencies in solid hosts. For illustration, the relaxation from an excited rare-earth level  $j$  that might be populated directly by resonant radiative absorption or via indirect excitation pathways is considered. Basically, two main processes compete with radiative transitions. The first process is the nonradiative decay, where a part of the excitation energy is converted into host vibrations by the emission of phonons; the process is known as MPR and is described in Section 2.2. Secondly, nonradiative energy transfer via ion-ion interactions can reduce the excitation energy. The luminescence lifetime of an excited level  $j$  is given by

$$\tau_j^{-1} = \sum_i (A_{ji} + W_{ji}), \quad (2.1)$$

where  $A_{ji}$  and  $W_{ji}$  are the radiative and the nonradiative transition rates from level  $j$  to levels  $i$ , respectively. The summation is over all final levels  $i$ . Nonradiative processes with the probabilities  $W_{ji}$  include MPR and energy transfer between different ions. In the experiments reported in this work, the rare-earth doping levels are low such that ion-ion interactions are negligible.



## 2.2. Multiphonon relaxation

indirect excitation routes are in principle possible. MPA is the inverse process of the MPR; its probability is usually  $10^2$  times (typical Boltzmann factor for the considered systems) lower than the corresponding MPR process. The ion-ion interaction processes only need to be considered for high rare-earth concentrations ( $> 1$  mol%) [39]. ESA requires that the pump pulse wavelength used for the initial excitation (GSA) is resonant with a possible second excitation step (ESA) from an excited level. Sufficiently low repetition rates allow for a basically complete relaxation of the excited population before the next excitation pulse enters.

Finally, another important quantity is considered. To enable a comparison of the luminescence efficiency of different luminescent materials, the absolute quantum efficiency  $\text{QE}(\lambda_{\text{ex}}, \lambda_{\text{em}})$  is used. It is defined as the number  $N_e$  of photons emitted by the sample in the wavelength range  $\lambda_{\text{em}}$  divided by the number  $N_\nu$  of photons of the excitation light that is absorbed by the sample in the wavelength range  $\lambda_{\text{ex}}$ , i.e.

$$\text{QE}(\lambda_{\text{ex}}, \lambda_{\text{em}}) = \frac{N_e(\lambda_{\text{em}})}{N_\nu(\lambda_{\text{ex}})}. \quad (2.3)$$

$\text{QE}(\lambda_{\text{ex}}, \lambda_{\text{em}})$  depends significantly on the radiative quantum efficiencies  $\eta_j$  of the involved rare-earth levels  $j$ . For the absolute luminescence quantum efficiency, various other processes play a role such as radiative transfers to other ions leading to reabsorption losses. Another principal difference between these two quantities is that the radiative quantum efficiency is related to a certain level  $j$  whereas the absolute quantum efficiency is related to the wavelength ranges  $\lambda_{\text{em}}$  and  $\lambda_{\text{ex}}$ .

## 2.2. Multiphonon relaxation

### 2.2.1. Theory of multiphonon processes

Multiphonon processes of rare-earths in crystals as well as in glasses are well established. Excited electronic levels of rare-earth ions decay nonradiatively by exciting phonons (or local vibrations) of the surrounding host material. When the energy difference of the considered excited level to the next level below is larger than the host's phonon energy, several phonons are emitted to bridge the energy gap. It is recognized that highest energy phonons of the host material determine the nonradiative decay. This is evident, because the highest energy phonons conserve energy in the lowest order and is thus the most probable process. This is not only true for phonons in crystals, but also for vibrational modes in glasses. It was demonstrated that the highest energy vibrations of glasses, i.e. the stretching vibrations of the network former polyhedra, are involved in the MPR rather than the lower energy vibrations of adjacent modes. These lower energy modes may be partially involved when the energy gap is not

## 2. Fundamentals

bridged entirely by the highest energy phonons [38]. Empirically, it was found that the MPR rate decreases exponentially with the energy gap and with the number of bridging phonons, when this number is larger than two. The importance of the highest energy phonons and the exponential dependence of MPR rates on the energy gap are established by numerous experimental investigations of rare-earth doped glasses and crystals [30, 31, 27, 32, 38].

MPR of rare-earth ions in glasses results from the same physical processes as in crystals. Lattice or network vibrations modulate the Stark field which induces nonradiative transitions between rare-earth electronic levels. This is the fundament of the theoretical treatment formulated by Kiel [40] for crystals; it is based on time-dependent perturbation theory in higher orders. As a continuation of Kiel's work, Riseberg and Moos [29] applied a phenomenological approach which explains well the experimental data for crystals [30] and is also applicable for glasses [31]. In the following paragraphs this approach is outlined shortly.

Using a point charge model for the network ions, the interaction of the rare-earth ion with the crystal field modulated by the lattice vibration can be expressed via the following Hamiltonian [29]:

$$H = V_0 + \sum_i V_i Q_i + \sum_{i,j} V_{ij} Q_i Q_j + \dots \quad (2.4)$$

$V_0$  is the static crystal field and the other terms represent the interaction with the vibrating lattice.  $Q_i$  and  $Q_j$  are the network normal mode coordinates, and  $V_i$  and  $V_{i,j}$  are partial derivations of the crystal field with respect to the corresponding normal modes. Riseberg and Moos' [29] treatment yields that the  $p$ -th order MPR rate has the following form:

$$W_{\text{MPR}}^{(p)} = W_{\text{MPR},0} \prod_i (n_i + 1)^{p_i} . \quad (2.5)$$

$W_{\text{MPR},0}$  is the spontaneous MPR rate at  $T = 0$  K.  $p_i$  is the number of emitted phonons with energy  $\hbar\omega_i$ , i.e. the total number of phonons emitted in the transition (order of the process) is  $p = \sum_i p_i$ .  $n_i$  is the Bose-Einstein occupation number of the phonon mode, being

$$n_i = (\exp(\hbar\omega_i/k_B T) + 1)^{-1} . \quad (2.6)$$

Assuming that phonons of single frequency  $\hbar\omega$  ( $i = 1$ ,  $p = p_i$ ) are involved in the decay, Equations 2.5 and 2.6 give the following approximation for the temperature dependence of the MPR rate:

$$W_{\text{MPR}}(T) = W_{\text{MPR},0} \cdot \left( \frac{\exp(\hbar\omega/k_B T)}{\exp(\hbar\omega/k_B T) - 1} \right)^p . \quad (2.7)$$

The dependence of the MPR rate on the energy gap can be described considering the ratio of the  $p$ -order and the  $(p-1)$ -order MPR rates. As a consequence

## 2.2. Multiphonon relaxation

of the convergence of the terms of the perturbation expansion the ratio is small, i.e. [32]

$$\frac{W_{\text{MPR}}^{(p)}}{W_{\text{MPR}}^{(p-1)}} = \varepsilon \ll 1; \quad (2.8)$$

$\varepsilon$  is known as the electron-phonon coupling constant. Consequently, the  $p$ -order MPR rate can be approximated as

$$W_{\text{MPR}}^{(p)} \approx \text{const.} \cdot \varepsilon^p = \text{const.} \cdot \exp(\ln \varepsilon \cdot p). \quad (2.9)$$

This means that the MPR rate decreases exponentially with the total number  $p$  of phonons (note that  $\ln \varepsilon$  is negative). Assuming that the decay is determined by the highest energy phonons, the order  $p$  of the process is approximately determined by the ratio of the energy gap  $\Delta E$  and the cut-off phonon energy  $\hbar\omega_{\text{max}}$  of the material, i.e.

$$p \approx \frac{\Delta E}{\hbar\omega_{\text{max}}}. \quad (2.10)$$

Defining  $\alpha = -\ln \varepsilon / \hbar\omega_{\text{max}}$  gives [32]

$$W_{\text{MPR}} \approx \text{const.} \cdot \exp\left(\frac{\ln \varepsilon}{\hbar\omega_{\text{max}}} \cdot \Delta E\right) = \text{const.} \cdot \exp(-\alpha \cdot \Delta E), \quad (2.11)$$

which shows that the MPR rate decreases exponentially with the energy gap between the emitting level and the next lower level. Apart from the energy gap of the corresponding rare-earth level, the MPR rate does not depend on the specific rare-earth ion chosen.

### 2.2.2. Low phonon materials

Since nonradiative losses by MPR decrease exponentially with the number of phonons required to bridge the energy gap  $\Delta E$  of any rare-earth level to its next lower level, the luminescence of a certain rare-earth level (with a given  $\Delta E$ ) depends significantly on the maximum phonon energy of the host. Thus, it is important to choose low phonon materials as rare-earth hosts. Metal-halide crystals with elements of high atomic mass are often used as rare-earth hosts since they can provide very low phonon energies. However, for certain applications, glasses are more interesting due to their mechanical properties; particularly, the glass fabrication is comparatively easy, the achievable size is not limited, and glasses can be drawn into fibers.

Table 2.1 lists the maximum phonon energies of two typical low phonon energy halide crystals and various common glasses together with their MPR rates for a given energy gap of  $\Delta E = 1,000 \text{ cm}^{-1}$ . The comparison shows the tendency of the MPR rate to decrease with the maximum phonon energy of

## 2. Fundamentals

Table 2.1.: Maximum phonon energies  $\hbar\omega_{\max}$  (given in  $\text{cm}^{-1}$ ) and MPR rates  $W_{\text{MPR}}$  (given in  $\text{s}^{-1}$ ) at  $\Delta E = 1,000 \text{ cm}^{-1}$  of various glasses and halide crystals.

matrix	$\hbar\omega_{\max}$	$W_{\text{MPR}}$	Ref.
borate glass	1,400	$10^{11}$	[41]
phosphate glass	1,200	$10^{10}$	[41]
silicate glass	1,100	$10^{10}$	[27]
germanate glass	900	$10^8$	[41]
tellurite glass	700	$10^8$	[41]
fluorozirconate glass	600	$10^7$	[17], [39]
LaF <sub>3</sub> crystal	350	$10^6$	[29]
PbCl <sub>2</sub> crystal	200	$10^5$	[42], [43]

the matrix material. The listed halide crystals LaF<sub>3</sub> and PbCl<sub>2</sub> with maximum phonon energies of 180 and 350  $\text{cm}^{-1}$  provide the lowest MPR rates, being about  $10^5$  and  $10^6 \text{ s}^{-1}$ , respectively. The maximum phonon energies of the listed glasses range from 600 to 1,400  $\text{cm}^{-1}$ ; the corresponding MPR rates range from  $10^7$  to  $10^{11} \text{ s}^{-1}$ . The fact that the phonon energies of the matrix materials differ by less than one order of magnitude while the corresponding MPR rates differ by six orders of magnitude shows the significance of the host's phonon energy.

The focus of this work is on FZ-based glasses, which are among the lowest phonon energy glasses providing excellent optical and feasible mechanical properties. Besides low MPR losses, low phonon materials provide high transparency until the mid IR, because the spectral position of the IR absorption edge is determined by MPA processes and hence by the material's maximum phonon energy.

The highest energy vibrations in glasses are stretching vibrations between anions and cations in the network former polyhedron. The vibrational energy depends significantly on the bond strength and the mass of the ions making the oscillator. In the harmonic approximation, the vibrational frequency  $\omega$  of two ions with a bond strength  $\kappa$  is given by

$$\omega = \sqrt{\frac{\kappa}{\mu}}, \quad (2.12)$$

where  $\mu$  is the reduced mass of the two ions. Although, the calculation of the vibrational frequencies in a glass network is much more complicated, Equation 2.12 shows a qualitative trend: Heavy elements with weak bonding provide the lowest phonon energy materials. When comparing the masses of the network former ions and the bonding strengths, Table 2.1 reveals the trend. According to this, chloride, bromide or selenide glasses for example can provide even lower phonon energies than fluoride glasses. However, weak bonding also implies low

thermal stability and high sensitivity to atmospheric moisture. For this reason, halide glasses other than fluoride glasses and also chalcogenide glasses provide poor durability and mechanical properties. In this work, an alternative low phonon energy rare-earth host material is examined. It is a FZ-based glass matrix containing BaCl<sub>2</sub> nanocrystals, i.e. a glass-ceramic system.

### 2.2.3. **Vibrational properties**

Atomic motions in amorphous and crystalline solids are organized into vibrational modes. In crystals, these modes are quantized and are known as phonons. This section briefly reviews their general physical properties.

Considering displacements of the lattice atoms around their equilibrium positions in a crystal, plane waves are found as a solution of the equations of motion. According to wave-particle duality, these lattice vibrations also exhibit properties of particles. Considering the interactions with other particles such as photons shows the particle character of the phonons. In the framework of scattering theory for example, the laws of conservation of energy and of momentum (crystal momentum) are valid.

The phonon dispersion relation in a three dimensional crystal with  $N$  atoms per unit cell, i.e. the dependence of the phonon frequency  $\omega$  on the wave vector  $\mathbf{q}$ , has  $3N$  phonon branches:  $3(N - 1)$  optical branches and 3 acoustical branches. One distinguishes between longitudinal acoustical (LA), transversal acoustical (TA), longitudinal optical (LO), and transversal optical (TO) phonon branches. Acoustical phonons have zero phonon frequency at  $\mathbf{q} = 0$  ( $\Gamma$  point, center of the Brillouin zone); and for small  $\mathbf{q}$  values their frequency  $\omega$  exhibits a linear dependence on the wave vector  $\mathbf{q}$ . In acoustical branches, the lattice atoms of an unit cell are vibrating in phase. Optical phonons on the contrary, exhibit non-zero frequency at the  $\Gamma$  point. The lattice atoms of an unit cell are moving out-of-phase, i.e. neighboring atoms are moving in opposite directions.

Since VIS light exhibits only very small wavenumbers, it can only interact with phonons near the  $\Gamma$  point according to the law of conservation of momentum. Thus, for optical spectroscopy, only phonon frequencies at the  $\Gamma$  point are relevant. Since acoustical phonons have zero phonon frequency at the  $\Gamma$  point, they are not further considered here. The phonon spectra (at the  $\Gamma$  point) of crystals or the vibrational spectra of amorphous solids can be experimentally determined by Raman and IR spectroscopy.

In Raman spectroscopy, light is inelastically scattered upon interaction with a vibrational mode. In IR spectroscopy, light is absorbed upon interaction with a vibrational mode. These different physical effects require different mode properties. Raman activity of a phonon requires a change in polarizability during the vibration. IR activity of a phonon requires a change in electric dipole moment during vibration. In both cases, this means that the derivative of the corresponding quantity with respect to the normal mode coordinate is non-zero.

## 2. Fundamentals

Because of the crystal symmetry and the resulting symmetry properties of the vibrations, which cause vanishing or non-vanishing derivatives, the observability of the corresponding phonon modes depends on the scattering geometry (direction and polarization of excitation and detection) of the experiment. According to group theory, lattice vibrations are classified into symmetry adapted mode types. All mode types that exist in each crystal class and all the mode types that are observable in a certain scattering geometry can be taken from Ref. [44].

Besides phonons in crystals, vibrational modes in glasses are investigated in this work. In disordered systems such as amorphous solids, a classification of the vibrational modes as described above is not possible. The vibrational properties of glasses differ from those of crystals. Their detailed understanding is still incomplete. The model of lattice vibrations requires a crystalline order. The disorder in amorphous solids causes a selection rules breakdown in such a way that vibrational modes with other than zero wave vector can also contribute to Raman scattering or IR absorption. Thus, the vibrational spectra of glasses, are not discrete as in crystals, but reveal broad bands. Additionally, the maximum phonon energy of common glasses is higher than in most crystals that are usually used as rare-earth hosts [27]. The highest energy vibrations in glasses are “molecular” stretching vibrations of the network former polyhedron. Besides this, their vibrational spectra contain several additional vibrational modes with lower phonon energies. For convenience, such vibrations in amorphous solids are also called “phonons” even if they are not quantized and delocalized as real phonons which occur only in crystals. This simplification is very common in the literature and is also used in this work.

## 3. Methods

This chapter describes the experimental and theoretical methods used in this work. Since the focus of this work is on the development and investigation of rare-earth doped glasses, whose luminescence properties are improved by the formation of low phonon energy nanocrystals, different methods for an analysis of the crystallization and of the structural, phononic and luminescence properties are employed.

### 3.1. Raman spectroscopy and phonon spectra calculations

#### 3.1.1. Raman spectroscopy

The vibrational spectra of the glasses and glass ceramics (with embedded nanocrystals) were investigated experimentally by Raman spectroscopy. This paragraph will briefly discuss the principle of Raman spectroscopy. In a Raman process, monochromatic light (usually from a laser in the VIS range) is inelastically scattered upon interaction with phonons (or other vibrational/rotational modes or other elementary excitations; for convenience the Raman effect is described in terms of phonons). The energy shift of the incoming and scattered photons corresponds to the energy of a phonon which is absorbed or emitted in the interaction process. The interaction with the incoming light is related to the polarizability of the valence electrons. The incoming electromagnetic wave induces a polarization. The periodic variation of the polarization causes the emission of an electromagnetic wave, which is the scattered light. In classical theory of the Raman effect [45], the scattered light is emitted from oscillating dipoles, which are given by the induced polarization. Besides elastic scattering (Rayleigh scattering) with the energy  $\hbar\omega_0$  of the incident light, the scattered radiation can contain other spectral components: If the polarization is modulated by atomic vibrations with the phonon frequency  $\omega$ , light with the energy  $\hbar(\omega_0 - \omega)$  (Stokes Raman scattering) and  $\hbar(\omega_0 + \omega)$  (anti-Stokes Raman scattering) is emitted symmetrically to the Rayleigh scattering line at  $\hbar\omega_0$ . As illustrated in Figure 3.1, Raman scattering can be described via an excitation into virtual states. In a Stokes Raman scattering process, the incoming light loses part of its energy by exciting vibrations in the system. In an anti-Stokes Raman scattering process, the energy of the incoming light increases by de-exciting lattice vibrations. The Raman shift relative to the laser line with the

### 3. Methods

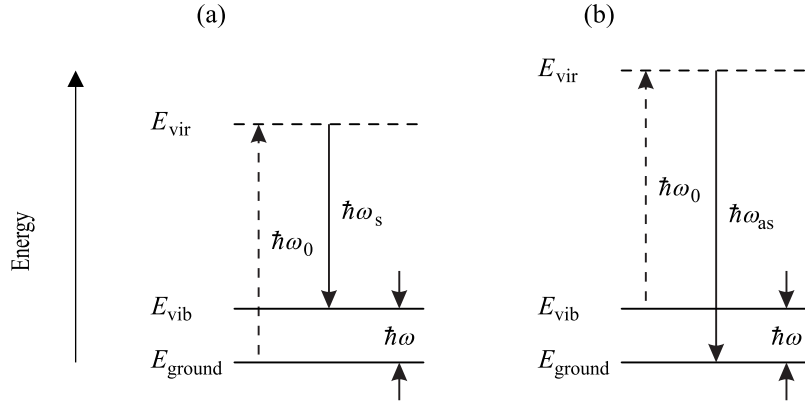


Figure 3.1.: (a) Stokes and (b) anti-Stokes Raman scattering.  $E_{\text{ground}}$  and  $E_{\text{vib}}$  are the ground state and a vibrational state of the scattering system, respectively.  $E_{\text{vir}}$  denotes a virtual state used to describe Raman scattering.

wavelength  $\lambda_0$  is normally given in reciprocal centimeters (relative wavenumber  $\tilde{\nu}$  in  $\text{cm}^{-1}$ ). This relative wavenumber  $\tilde{\nu}$  corresponds to the energy  $\hbar\omega$  of the respective phonon modes and is related to Stokes and anti-Stokes Raman scattering as follows:

$$\begin{aligned} \tilde{\nu}(\text{cm}^{-1}) &= \left( \frac{1}{\lambda_0(\text{nm})} - \frac{1}{\lambda_s(\text{nm})} \right) \cdot \frac{10^7(\text{nm})}{(\text{cm})} = (\hbar\omega_0(\text{eV}) - \hbar\omega_s(\text{eV})) \\ &\cdot \frac{1}{h(\text{eV} \cdot \text{s}) \cdot c(\text{cm/s})} = \hbar\omega(\text{eV}) \cdot \frac{1}{h(\text{eV} \cdot \text{s}) \cdot c(\text{cm/s})} \quad (\text{Stokes}) \end{aligned} \quad (3.1)$$

and

$$\begin{aligned} \tilde{\nu}(\text{cm}^{-1}) &= \left( \frac{1}{\lambda_0(\text{nm})} + \frac{1}{\lambda_{\text{as}}(\text{nm})} \right) \cdot \frac{10^7(\text{nm})}{(\text{cm})} = (\hbar\omega_0(\text{eV}) + \hbar\omega_{\text{as}}(\text{eV})) \\ &\cdot \frac{1}{h(\text{eV} \cdot \text{s}) \cdot c(\text{cm/s})} = \hbar\omega(\text{eV}) \cdot \frac{1}{h(\text{eV} \cdot \text{s}) \cdot c(\text{cm/s})} \quad (\text{anti - Stokes}) \end{aligned} \quad (3.2)$$

where  $\lambda_s$  ( $\lambda_{\text{as}}$ ) and  $\hbar\omega_s$  ( $\hbar\omega_{\text{as}}$ ) are the wavelength and the energy of the Stokes (anti-Stokes) Raman scattered light, respectively. For convenience, the phonon energy  $\hbar\omega$  is usually given in  $\text{cm}^{-1}$  ( $\text{cm}^{-1}$  can be calculated into eV via a constant factor given by the Planck constant  $h$  and the velocity of light  $c$ , see Equations 3.1 and 3.2). Stokes Raman scattering has higher probability than anti-Stokes Raman scattering, because the latter one requires phonons in excited states. According to Boltzmann's law, more phonons are in the ground state than in excited states at ambient temperature. As described in Section 2.2.3, phonons can be measured by Raman spectroscopy if they are Raman-active and if the used scattering symmetry allows for a detection of the symmetry adapted mode type of the corresponding vibration.

For all Raman spectra presented in this work, Stokes Raman scattering is shown. In this paragraph, the Raman setup and the measurement parameters

### 3.1. Raman spectroscopy and phonon spectra calculations

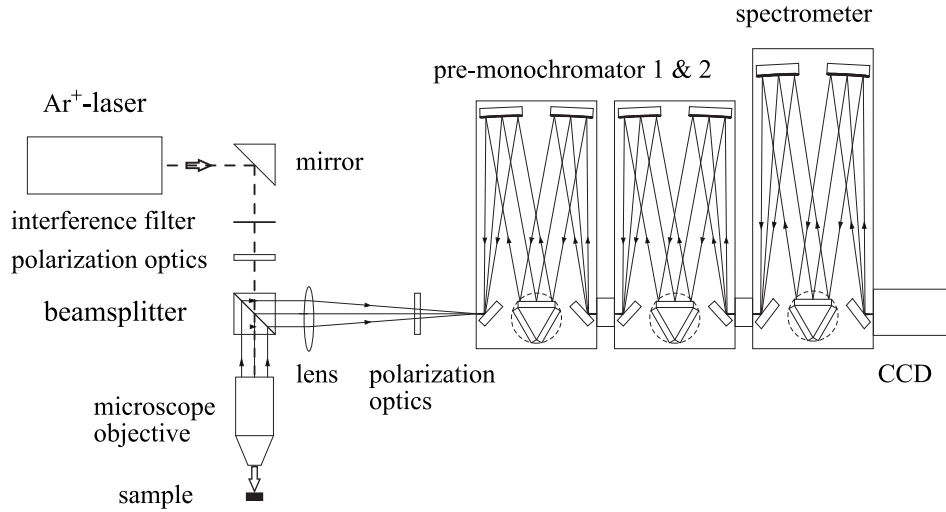


Figure 3.2.: Schematic of the micro-Raman setup. The sample excitation and the signal detection are performed through a microscope objective.

used are described. The measurements were done with a confocal triple 557 TriVista Raman spectrometer (S&I Spectroscopy & Imaging GmbH) in reflection geometry. A schematic of the micro-Raman setup is shown in Figure 3.2. Raman scattering is excited with the 488.0 nm line of an argon ion laser (543-AP-A01 from Melles Griot) with a power level of approximately 50 mW (except for the last Raman measurement in Chapter 6 where the 514.5 nm line of the same laser is used for comparison). The laser output is tuned via the resonator length and an additional intracavity filter. The corresponding laser line is further selected with an external interference filter. The laser is focused on the sample with a 50x/0.75 microscope objective to a spot size of about 2  $\mu\text{m}$ . The scattered light is transmitted through the beam splitter. Scattering near the laser line is rejected with the first two monochromators (both: 900 g/mm grating, focal length of 500 mm; monochromator 1: entrance slit 50  $\mu\text{m}$ , output slit 10,000  $\mu\text{m}$ ; monochromator 2: entrance slit 10,000  $\mu\text{m}$ , output slit 50  $\mu\text{m}$ ) configured in subtractive dispersion mode. In this configuration these two pre-monochromators work as a bandpass filter. A third monochromator (1,500 g/mm grating, focal length of 750 mm, entrance slit 50  $\mu\text{m}$ , output slit 10,000  $\mu\text{m}$ ) is used to disperse the passing light. The Raman spectra are recorded with a nitrogen cooled 1024 x 256 Si-CCD camera. For this work, only unpolarized Raman measurements are performed. The polarization optics (combination of achromatic depolarizers and linear polarizers) are used to depolarize the laser and the scattered light and to remove polarization bias from the optical components.

### 3. Methods

#### 3.1.2. First principles calculations

For a comprehensive investigation of the phononic properties of the nanocrystals, all phonon modes of crystalline  $\text{BaCl}_2$  in hexagonal and orthorhombic symmetry were calculated from first principles. Recent theoretical and computational methods have proven to be capable of a precise description of static properties and dynamical effects in a lattice without using any experimental or empirical input parameters. These methods treat systems of nuclei and electrons on the basis of DFT; they have been implemented in different software packages, such as ABINIT [46, 47] that is used for the calculations presented here. The simulations were performed by Bohley *et al.* [48]; Ref. [48] gives more details about the applied computational approach. This section outlines how the phonon spectra are calculated, once the static parameters (atomic positions and cut-off energies) of a crystal are known. The static parameters were calculated from DFT by structural relaxation. For the implementation in the ABINIT package, the pseudopotentials used for Ba and Cl, and general information about the DFT method, the reader is referred to Ref. [48] and the related literature.

Treating small deformations as perturbations of the potential of the system allows for a calculation of the crystal's phonon modes. The dependency of potential energy  $U$  on small displacements of the atoms around their equilibrium positions can be described via a harmonic approximation. Forces appear upon displacement of the atomic positions. The force constant matrix gives the corresponding linear relations: It allows for a calculation of the force on each atom along a certain direction which is caused by the displacements of the other nuclei (or of itself). The corresponding equations of motion yield the frequencies of the vibrational modes of the system. The wave vector dependent frequencies of the phonon modes are the eigenvalues of the dynamical matrix, which are the Fourier transforms of the force constants. In order to obtain the phonon frequencies of the relevant Raman- and IR-active modes, the dynamical matrix is computed at zero wave vector ( $\Gamma$  point) within a variational approach, treating the deformations by way of perturbation inside DFT. The formalism is known as density functional perturbation theory (DFPT). The local density approximation (LDA) is used for the exchange correlation functional. The applied approximations and the computation of the dynamical matrix within the ABINIT software are described in detail in Ref. [47]. Symmetry considerations allow for a decomposition of the dynamical matrix according to an irreducible representation of the point group of the crystal. Raman and IR phonon modes are identified from this representation.

In order to calculate Raman spectra from the obtained Raman-active modes, the Raman scattering efficiency is considered; it depends on the projection of the Raman susceptibility tensors on the polarization vectors of the incoming and the scattered light. To enable a comparison to the experimental unpolarized

### 3.2. Time-resolved and spectrally-resolved photoluminescence

Raman spectra, which are measured on randomly orientated nanocrystals, the Raman intensities are calculated in analogy to those of powder spectra. For this purpose, the Raman intensities are estimated by performing averages over all possible crystal orientations and over all possible laser polarizations, for the equations used; see Refs. [47] and [49]. The Raman line profiles cannot be obtained from the calculation method. For simplicity, the Raman intensity lines are assumed to be Lorentzian and the line width is adapted to the experimental data.

## 3.2. Time-resolved and spectrally-resolved photoluminescence

### 3.2.1. Photoluminescence experiments

The light emission following a sample excitation by photons is called photoluminescence. In the present case, PL emissions from excited rare-earth ions in glasses and glass ceramics are investigated. Two types of PL measurements are performed: Spectrally-resolved and the time-resolved PL intensities are recorded. The setup used for the detection of both is presented in Figure 3.3. The excitation beam is focused onto the sample by a lens to a spot size of about 0.2 mm. The excitation source is described in Section 3.2.2. For the temperature-controlled measurements the sample is placed into a closed-cycle helium cryostat (Advanced Research Systems CS204\*F-GMX-20-OM) or onto a heating stage (Scientific Instruments Linkam HFS 600). The PL emitted from the sample is collected and subsequently imaged to the entrance of the monochromator by two off-axis parabolic mirrors (both: diameter 100 mm; first mirror: effective focal length 200 mm; second mirror: effective focal length 400 mm). Appropriate longpass filters are mounted in front of the monochromator. A 500 mm (focal length) Czerny-Turner monochromator (Princeton Instruments Acton SP2500) equipped with 600 g/mm VIS and NIR gratings is used. According to the ratio of the focal lengths of the two parabolic mirrors, the monochromator slits are set to approximately 0.4 mm in order to image the illuminated sample area optimally. The resulting spectral resolution is approximately 1 nm. The signal acquisition is done with a GaAs-based photomultiplier tube (PMT) (Hamamatsu R943-02) in the VIS and with a InP/InGaAs-based PMT module (Hamamatsu H10330A-75) in the NIR; both are thermoelectrically cooled. The acquisition technique is described in Section 3.2.3. To exclude any unwanted contribution other than the rare-earth luminescence, a corresponding rare-earth free glass or glass ceramic is always measured as a reference sample.

### 3. Methods

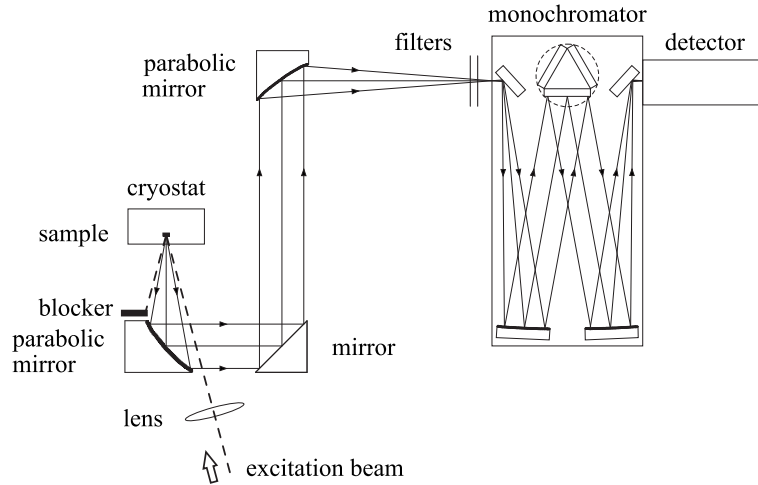


Figure 3.3.: Schematic of the PL detection setup.

#### 3.2.2. Generation of selective laser pulses

A collinear optical parametric amplifier (Light Conversion ORPHEUS) of white-light continuum pumped by a femtosecond (fs) laser system (Light Conversion PHAROS) is employed for PL excitation.

The PHAROS is a compact fs laser system operating at 1030 nm. Its active laser medium is an ytterbium-doped potassium gadolinium tungstate (KGW) crystal that is pumped by laser diode modules. Using the chirped pulse amplification (CPA) method the system provides fs laser pulses with mJ pulse energies at kHz repetition rates. The repetition rate is reduced to 100 Hz or less to avoid ESA in the analyzed samples (see Section 2.1.2). For this purpose, a pulse picker controlled by a frequency division system is used.

The compact housing of the ORPHEUS includes a white-light continuum generation (WLG) module, a second harmonic generation (SHG) module, and two amplification modules. The input waves for the parametric amplification processes are the high energy pump wave ( $\lambda_{\text{pump}} = 515$  nm) and the tunable so-called signal wave ( $\lambda_s$ ), a specific wavelength region of the white light continuum for selective amplification. Pump and signal are obtained from SHG and WLG of the fundamental PHAROS beam, respectively. In parametric amplification, pump photons are converted into signal photons (with the same wavelength as the input signal wave) and the so-called idler photons. According to the law of conservation of energy, the idler wavelength  $\lambda_i$  can be calculated from the pump wavelength  $\lambda_{\text{pump}}$  and the selected signal wavelength  $\lambda_s$  via

$$\frac{1}{\lambda_i} = \frac{1}{\lambda_{\text{pump}}} - \frac{1}{\lambda_s}. \quad (3.3)$$

Accordingly, the ORPHEUS provides two tunable output waves in the spectral ranges of 630 – 950 nm (signal) and 1100 – 2600 nm (idler) and a residual

### 3.2. Time-resolved and spectrally-resolved photoluminescence

pump wave at 515 nm. This widely tunable wavelength range in combination with an external SHG crystal (behind the OPA output) allows for selective excitation of  $\text{Nd}^{3+}$  levels; the whole VIS spectral range and the NIR up to 2.6  $\mu\text{m}$  is covered. Only ultra-short pulses, such as those of fs laser systems, enable sufficiently high efficiency of the nonlinear optical effects needed here. Therefore, the temporal width of the provided pulses is shorter (full width at half maximum (FWHM) of about 200 fs) than necessary and thus, according to Heisenberg's uncertainty principle, exhibit a relatively broad spectral pulse width (FWHM of about 8 nm).

To enable narrow bandwidth excitation and to avoid spectral overlap of excitation and detected emission, the spectral width of the excitation pulses is reduced by about a factor of 2 by passing a monochromator (Bausch & Lomb BM 25/25; focal length of 250 mm, 100 g/mm grating) placed in front of the sample (excitation monochromator). The resulting increased temporal pulse width is still negligibly short (a few hundred fs) in comparison to the investigated dynamical processes in the rare-earth ions ( $\mu\text{s}$  range). Due to the short pulse widths and the low repetition rates, ESA can be excluded here, which is beneficial for the analysis of the MPR dynamics (see Section 2.1.2). To avoid nonlinear optical effects in the samples such as two photon absorption, the pulse energies are kept as low as possible. The average power is reduced to the order of  $10^{-1}$  mW.

Finally, an example is given to illustrate how excitation pulses of a certain wavelength are obtained using the laser source. The generation of the selective laser pulses centered at 576 nm is presented; they are used for the time-resolved PL measurement in Figure 5.10 (excitation at 576 nm, detection at 589 nm). The signal wavelength of the OPA is tuned to about 931 nm in order to obtain an idler wavelength of 1152 nm (see Equation 3.4). To avoid any residual pump light a long pass filter is used (OG590). Due to the collinear nature of the ORPHEUS, the signal beam has to be separated from the idler beam with a wavelength separator, which shifts the signal beam with a high reflectivity dielectric mirror and blocks it by a metal cover. Using the external SHG crystal, the desired 576 nm laser light is generated from the idler beam. Subsequently, the excitation monochromator is used to reduce the spectral width; the spectra of the laser pulses before (FWHM of 8 nm) and after passing (FWHM of 4 nm) the monochromator are presented in Figure 3.4. A bandpass interference filter (central wavelength 577 nm, bandwidth 10 nm) is placed in front of the sample to avoid any wavelength other than the desired excitation. Finally, the excitation intensity is reduced by neutral density filters.

#### 3.2.3. Data acquisition and photon counting

The collection and analysis of the PL emissions entering the monochromator equipped with the PMT is realized with a single-point spectroscopy detec-

### 3. Methods

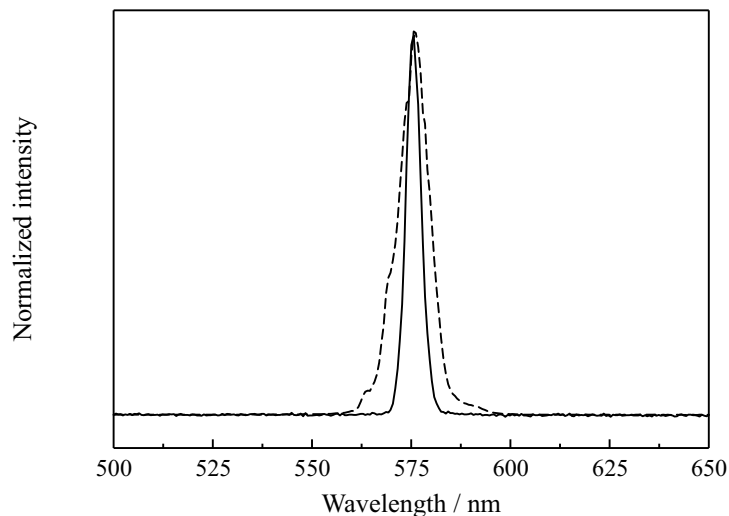


Figure 3.4.: Spectra of laser pulses before (dashed line) and after (solid line) passing the excitation monochromator used for reducing the spectral line width. The pulses are centered at 576 nm.

tion system (Princeton Instruments SpectraHub/SpectraSense package). SpectraHub is a monochromator control module with an A/D converter compatible for PMT detectors and photon counting. The spectra acquisition is performed with the integrated spectroscopy SpectraSense software package. Time-resolved PL is recorded at a specific wavelength using the photon counting technique.

Time-resolved photon counting is a common electronic acquisition technique applied to measure relaxation processes of excited states after their simultaneous excitation. The time difference between individual photon events and the excitation pulse are averaged over many excitation and luminescence cycles to generate a transient PL profile that represents the time dependence of the luminescence intensity. A photon counter (Picoquant NanoHarp 250) supported by a PMT preamplifier (Picoquant PAM 102) and NanoHarp data acquisition software providing high sensitivity is applied here. It is a multichannel (262144 time channels available) scaler with count rates up to 50 million counts per seconds exhibiting a time resolution down to 4 ns. Multichannel scalers process multiple photons per excitation cycle, which reduces the required measurement time. This is, in particular, advantageous if relatively long luminescence decay times are investigated as in the present case, because only low excitation rates can be used accordingly. The digital counter is triggered with an electrical signal supplied by the laser.

### 3.3. Additional experimental techniques

#### 3.3.1. Differential scanning calorimetry

Differential scanning calorimetry (DSC) is a thermoanalytical method that measures the difference in the heat required to change the temperature of a sample and a reference with known heat capacity. DSC measurements show endothermic and exothermic reactions in a sample during heating or cooling. DSC scans provide information about crystallization, fusion and vitrification events.

Here, power compensating DSC is performed. Sample and reference are placed in a thermal isolated oven that is controlled in such a way that sample and reference are maintained at the same temperature. The electrical power required for this is measured as a function of temperature, which changes linearly in time. DSC is measured from 150 to 430 °C with different heating rates of 5, 7.5, 10, 15, 20, and 30 K/min using a NETZSCH DSC 204 F1 Phoenix system. Small pieces of the sample with a mass of about 30 mg are placed into an aluminum crucible; a similar empty crucible is used as a reference .

#### 3.3.2. X-ray diffraction

X-ray diffraction (XRD) is a widespread method used to obtain structural information of solids. Reflections in a diffraction pattern are caused by constructive interference of X-ray waves diffracted on different periodic atomic planes or centers of the sample. Constructive interference is found when the difference in path is equal to an integer multiple of the wavelength  $\lambda$  of the X-ray photons; this is expressed by Bragg's law:

$$2 \cdot d \cdot \sin \Theta = n \cdot \lambda. \quad (3.4)$$

Here,  $d$  is the distance between diffracting planes,  $\Theta$  is the incident as well as the diffraction angle, and  $n$  is any integer. Besides spacing between atomic planes and many other structural parameters, XRD allows for a determination of the mean size of crystallites up to a size of about 100 nm [50]. Neglecting stress and strain effects, the crystallite diameter  $a$  can be calculated from the diffraction angle  $\Theta$  and the corresponding FWHM  $b$  (in radians) of a crystalline reflection by the Scherrer formula [51]:

$$a = \frac{K \cdot \lambda}{b \cdot \cos \Theta}. \quad (3.5)$$

The Scherrer constant  $K$  is a crystallite-shape factor; it is set to 1 as usual for low-order reflections from crystallites with simple regular shapes [52].

XRD measurements were carried out with a Bruker AXS D8 advance diffractometer in the Bragg-Brentano focusing  $2\Theta$  geometry. The diffractometer is equipped with a linear detector (LynxEye). Cu- $K_\alpha$  radiation from a Cu tube operating at 40 kV and 40 mA having a wavelength of  $\lambda = 0.1542$  nm is used.

### 3. Methods

Cu- $K_\beta$  radiation from the tube is attenuated by a nickel filter. The Cu- $K_{\alpha 2}$  components are subtracted from the measured diffraction patterns using the EVA v1.2 XRD analysis software package.

#### 3.3.3. Mössbauer spectroscopy

The Mössbauer measurements on the glasses and glass ceramics were performed at the University of Tennessee Space Institute, Tullahoma, TN, USA.

The Mössbauer effect is known as the recoil-free absorption (or emission) of gamma radiation by an atomic nucleus that is bound in a solid. Due to the extremely high energy of gamma photons, gamma ray absorption (or emission) by a free nucleus causes a considerable recoil effect such that the energy of gamma rays absorbed (or emitted) by a nucleus is shifted with respect to the energy of the corresponding nuclear transition; this shift corresponds to the recoil energy. In contrast, the absorption (or emission) of gamma rays by a nucleus that is bound in a solid, in which atomic motions and the related recoil energy losses are quantized (phonons), can be recoil-free (zero phonon mode). In this case, the momentum is transferred to the whole crystal lattice with practically no recoil energy loss due to the lattice's high mass.

This effect is used in the Mössbauer absorption spectroscopy applied here. The intensity of gamma rays from an appropriate source that are transmitted through a sample is measured. The atoms of the gamma ray source must be a radioactive parent that decays to the same isotope as the analyzed atoms. The energy of the nuclear levels shifts slightly (isomer or chemical shift) with the chemical environment of the atom. In order to bring the  $\gamma$ -rays from the Mössbauer source into resonance with the energy of the nuclei in the sample, the Doppler effect is used. For this purpose, the Mössbauer source is accelerated through a suitable velocity range (typically 1 mm/s corresponds to the sub  $\mu\text{eV}$  energy range). The transmitted intensity is plotted as a function of the velocity of the source. The absorption bands in such a Mössbauer spectrum correspond to nuclear energy levels of the absorbing nuclei. An analysis of the absorption bands provides information about the chemical environment and oxidation state of the nuclei of the atoms or ions in the sample.

The measurements were done with a Mössbauer spectrometer manufactured by SEE Co, Edina, MN, USA. 21.7 keV  $\gamma$ -rays from a  $^{151}\text{SmF}_3$  source are used for the  $^{151}\text{Eu}$  Mössbauer spectroscopy. The source is accelerated with a linear motor through a velocity range of  $\pm 36$  mm/s. The samples are placed in a closed cycle cryostat (Janis, Wilmington, MA and SEE Co), which enables cooling of the samples at temperatures down to 6 K. The detection is carried out with a Kr-filled proportional counter; the integration time used is 3-5 days. The resulting spectra are fitted with a custom Mössbauer fitting program for the  $^{151}\text{Eu}$  (21.7 keV) resonance; a Lorentzian line profile is used in the fitting procedure.

#### **3.3.4. Transmission spectroscopy**

Optical transmittance spectra give the ratio of the light intensity in front of and behind a sample as a function of the wavelength. Transmission spectroscopy was performed with a UV/VIS/NIR double beam, double monochromator, ratio-recording spectrophotometer (Perkin Elmer Lambda 1050). The spectrophotometer is equipped with a pre-aligned tungsten-halogen and deuterium light source and coupled to a 150 mm integrating sphere. A photomultiplier and peltier-cooled InGaAs detector is used for the detection in the entire UV/VIS and in the NIR (above 860 nm) range, respectively. The spectra are recorded between 250 and 1,000 nm with a spectral resolution of approximately 0.1 nm.

#### **3.3.5. Absolute quantum yield determination**

The quantum efficiency measurements on the Nd<sup>3+</sup>-doped samples were performed at the South Westphalia University of Applied Sciences, Soest, Germany.

The absolute quantum efficiency that is defined in Section 2.1.2 by Equation 2.3 is measured with a Hamamatsu C9920-02G precision quantum yield evaluation system for luminescence materials. This compact system employs the PL method (see Section 2.1.2). It is equipped with a 150 W Xe lamp and a monochromator for excitation. The sample luminescence is measured inside a spectralon integrating sphere. The detection is realized with a photonic multi-channel analyzer spectrograph (Hamamatsu PMA-12) which is equipped with a compact Czerny-Turner monochromator and a highly sensitive back thinned CCD (BT-CCD). In order to obtain a sufficiently high signal-to-noise ratio, relatively large monochromator slit widths corresponding to a spectral resolution of about 5 nm are used.



## 4. Crystallization processes in rare-earth doped glasses

The preparation of the FZ-based glasses and glass ceramics studied and their basic characterization are presented in this chapter. The glass ceramics are produced through a thermal postprocessing of the as-made glasses inducing the formation of  $\text{BaCl}_2$  nanocrystals. Besides the composition, synthesis and basic properties of the glasses, the crystallization behavior, the thermal treatment and the structural characterization of the formed nanocrystals are described here. The MPR rates, which are of particular interest in this work, depend basically on the host material and on the energy difference of the considered rare-earth level to its next lower level, but not on the specific rare-earth ion used.  $\text{Nd}^{3+}$  is investigated as a representative trivalent rare-earth ion, because it has suitable spectroscopic properties for the analysis of MPR dynamics of rare-earth ions in these host materials. In order to avoid ion-ion interaction processes a low doping concentration is chosen, which further facilitates the investigation of the host-dependent MPR dynamics. Some parts of this chapter have already been published in Ref. [53].

### 4.1. Composition and synthesis of fluorozirconate-based glasses

The chemical composition used for the glasses and glass ceramics is based on the well-known ZBLAN ( $\text{ZrF}_4\text{-BaF}_2\text{-LaF}_3\text{-AlF}_3\text{-NaF}$ ) formulation, which is the most stable composition of heavy metal fluoride glasses (HMFG) [18]. Besides low phonon energies and high transparency from the near UV to the mid IR, HMFG glasses provide low refractive index, low material dispersion, and the best mechanical properties among halide glasses making them applicable as optical fibers and rare-earth host materials [54, 18]. In comparison with oxide glasses, halide glasses are sensitive to moisture. However, it was found that the effect of atmospheric moisture on fluoride glasses is very weak and that they provide very long durabilities when used in practical environments [55]. Table 4.1 gives the chemical compositions of the samples prepared in the framework of this thesis. The FCZ glass composition used here is close to the standard ZBLAN formulation, but some fluorides are substituted by chlorides, which initiate the growth of  $\text{BaCl}_2$  nanocrystals upon thermal processing

#### 4. Crystallization processes in rare-earth doped glasses

Table 4.1.: Compositions of the FCZ and FZ glasses prepared in this work. Different rare-earth (RE) doping concentrations  $x = 0, 0.1, \text{ and } 1.0$  are used. For FCZ glasses doped with trivalent rare-earth ions charge compensation is required ( $y = 1$  for rare-earth doped glasses and  $y = 0$  rare-earth free glasses). All fractions of the components are given in mol%.

	ZrF <sub>4</sub>	BaF <sub>2</sub>	BaCl <sub>2</sub>	NaF	NaCl	LaF <sub>3</sub>	AlF <sub>3</sub>	InF <sub>3</sub>	KCl	RE-F <sub>3</sub>
FCZ	53- $y$	10	10	-	20- $x$	3.5	3	0.5	$y$	$x$
FZ	53- $x$	20	-	20	-	3.5	3	0.5	-	$x$

(see next section). Besides FCZ glasses, FZ (chlorine-free) glasses are produced for comparison. Various FZ and FCZ glass samples with different rare-earth doping concentrations  $x = 0, 0.1, \text{ and } 1.0$  mol% are made. The focus of this work is on 1 mol% Nd<sup>3+</sup>-doped FCZ samples. All other samples which are prepared for the purpose of comparison are produced in an analogous manner. In addition, europium-doped samples are also prepared.

The constituent high purity chemicals are pulverized and mixed in a mortar. The mixture is melted in a glassy carbon crucible at 745 °C and then poured into a brass mold that is at a temperature of 200 °C, i.e. below the glass transition temperature of an FZ-based glass [18], before being slowly cooled down to room temperature. All glasses are prepared inside a glove box with an inert argon atmosphere to avoid oxygen and moisture contamination.

The europium-doped samples used for the Mössbauer investigations were prepared at the University of Tennessee Space Institute under comparable conditions (see Chapter 7).

## 4.2. Thermal treatment and structural analysis

The crystallization behavior is investigated by DSC. Figure 4.1 shows the DSC measurement of the 1 mol% Nd<sup>3+</sup>-doped FCZ glass for a heating rate  $\alpha$  of 10 K/min. Points of interest are indicated in the graph. Table 4.2 lists the temperatures of these points and the corresponding thermal stability parameters for all heating rates. Two endothermic peaks are found. The one at about 220 °C is caused by the glass transition ( $T_g$  indicates the glass transition temperature). The other one is correlated with the glass melting which sets in at  $T_m \approx 410$  °C. These characteristic temperatures are slightly below those of pure FZ glasses, for which  $T_g$  and  $T_m$  are about 260 °C and 500 °C for a heating rate of 10 K/min, respectively [18, 56]. Additionally, several exothermic peaks occur, which are related to various crystallization processes. The huge peak at 310 °C is caused by a partial crystallization of the glass matrix; it can be assigned to the formation of  $\beta$ -BaZrF<sub>6</sub> and NaZrF<sub>5</sub> [18, 57]. An important crystallization peak is the one at about 240 °C. It is associated with the formation of BaCl<sub>2</sub>

#### 4.2. Thermal treatment and structural analysis

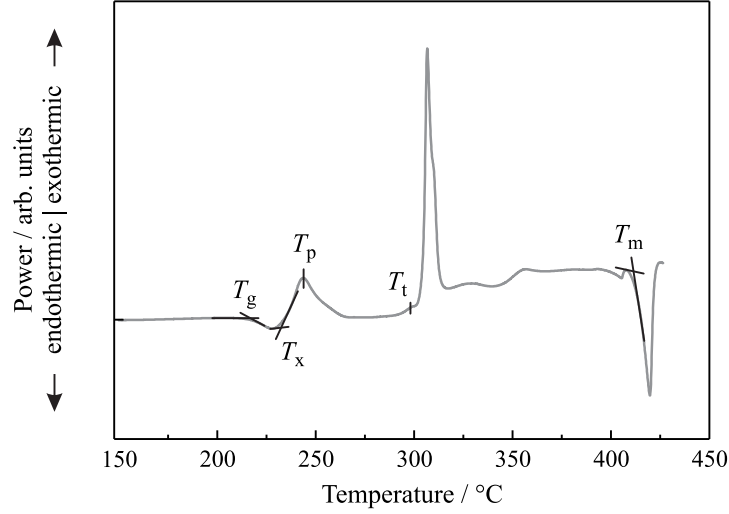


Figure 4.1.: DSC data of the 1 mol% Nd<sup>3+</sup>-doped FCZ glass. The heating rate was 10 K/min.

nanocrystals. At about 300 °C, directly before the huge crystallization peak, an exothermic peak  $T_t$  is found; it is related to a phase transition of the BaCl<sub>2</sub> nanocrystals. These two peaks are not observed in chlorine-free FZ glasses [58]; the BaCl<sub>2</sub> crystallization is initiated by the addition of chlorine ions.

$T_x$  is defined as the onset of the first crystallization peak. Its peak temperature is called  $T_p$ . Two thermal stability parameters are defined as

$$\Delta T = T_x - T_g \quad (4.1)$$

and

$$H_r = \frac{\Delta T}{T_m - T_x}. \quad (4.2)$$

$\Delta T$  characterizes the devitrification tendency of the glass. The Hruby constant  $H_r$  [59] gives information about the nucleation rate of the crystals in the temperature range from  $T_x$  to  $T_g$  and the growth rate between  $T_m$  and  $T_x$  [56]. Both parameters are listed in Table 4.2.

Additionally, DSC measurements performed at different heating rates allow for a determination of the apparent activation energy  $E_a$  of crystallization using the Kissinger's method:

$$\frac{d \left( \ln \left( \alpha / T_p^2 \right) \right)}{d \left( 1 / T_p \right)} = - \frac{E_a}{R}; \quad (4.3)$$

$R$  is the gas constant.  $E_a$  is the slope of the plot  $\ln(\alpha/T_p^2)$  vs.  $1/T_p$  which is shown in Figure 4.2. The activation energy is determined to be approximately 250 kJ/mol. The influence of the rare-earth ions and the crystallization behavior on the related parameters will be handled in the next section.

#### 4. Crystallization processes in rare-earth doped glasses

Table 4.2.: Characteristic temperatures and thermal stability parameters of the 1 mol% Nd<sup>3+</sup>-doped FCZ glass for different heating rates  $\alpha$ .

$\alpha$ (K/min)	$T_g$ (°C)	$T_x$ (°C)	$T_p$ (°C)	$T_t$ (°C)	$T_m$ (°C)	$\Delta T$ (K)	$H_r$
5	212.9	227.7	237.9	292.7	412.4	14.8	0.08
7.5	213.9	230.3	241.5	296.7	413.4	16.7	0.091
10	217.0	232.4	243.6	298.9	412.2	15.4	0.086
15	218.3	234.8	247.2	303.5	410.5	16.5	0.094
20	222.5	237.2	249.7	305.4	409.3	14.7	0.085
25	224.7	240.2	251.8	308.1	410.0	15.5	0.092

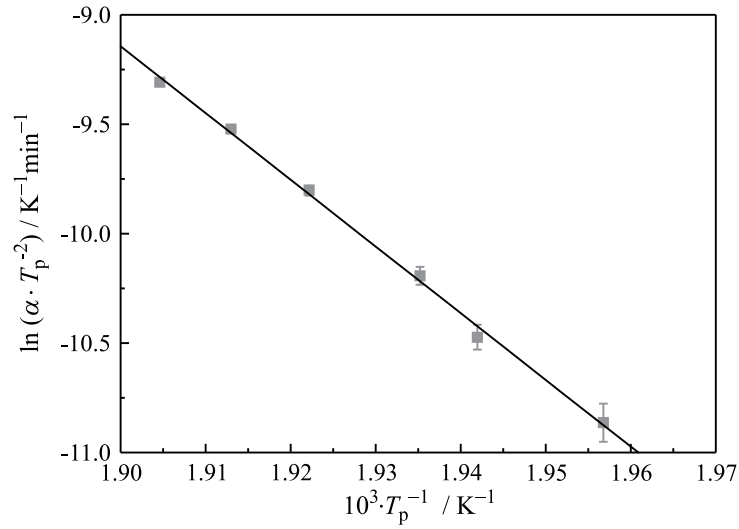


Figure 4.2.: Arrhenius plot for the 1 mol% Nd<sup>3+</sup>-doped FCZ glass. The slope gives the apparent activation energy  $E_a$ .

Before the thermal treatment, the glass was cut into six pieces with sizes of approximately 6 mm x 8 mm x 1.6 mm. In order to induce the formation of BaCl<sub>2</sub> nanocrystals of different size and phase, the glasses were annealed at different temperatures between 240 °C and 280 °C. The annealing time was 20 min for each sample. The annealing procedures were also performed in inert argon atmosphere. An as-made glass was kept for comparison. The visual appearance is transparent for the as-made and the 240 °C to 260 °C samples; for higher annealing temperatures the samples look more and more milky white. Figure 4.3 shows the resulting sample series under UV illumination. The average crystallite size increases with the annealing temperature and increasing scattering effects can be observed.

The nanocrystal size and phase as well as the volume fraction of the crystallites in the amorphous glass matrix was investigated by XRD. The XRD data of the 1 mol% Nd<sup>3+</sup>-doped FCZ sample series is shown in Figure 4.4. The corresponding powder diffraction file (PDF) data is shown for comparison. The

## 4.2. Thermal treatment and structural analysis

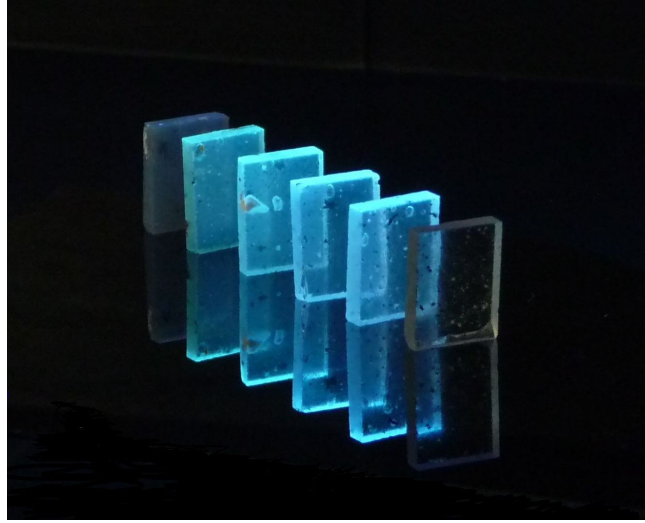


Figure 4.3.: Digital photograph of the 1 mol% Nd<sup>3+</sup>-doped FCZ glasses and glass ceramics under UV illumination. From front to back: as-made FCZ and FCZ annealed at 240, 250, 260, 270, and 280 °C.

Table 4.3.: Average sizes and volume fractions of BaCl<sub>2</sub> nanocrystals in the 1 mol% Nd<sup>3+</sup>-doped FCZ glasses annealed at different temperatures.

annealing temperature (°C)	240	250	260	270	280
crystallite size (nm)	10	10	15	41	62
volume fraction (%)	16	16	19	18	15

crystalline reflections are superimposed on the amorphous glass background characterized by two broad bands at 24° and 46°, which is typical for FZ-based glasses [60]. Though the as-made FCZ sample does not show any crystalline reflections, the XRD data of the 240 °C to 260 °C samples comprise reflections that can be assigned to hexagonal BaCl<sub>2</sub> (bottom bar graph, PDF 45-1313). Upon annealing at 270 °C, additional reflections appear that can be assigned to orthorhombic BaCl<sub>2</sub> (top bar graph, PDF 24-0094). The 280 °C sample shows reflections only from orthorhombic BaCl<sub>2</sub>; the hexagonal BaCl<sub>2</sub> reflections have completely disappeared. The observed phase changes can be correlated to the exothermic peaks found in the DSC measurements for this temperature range. However, a phase transition to orthorhombic phase BaCl<sub>2</sub> has not been observed before in Nd<sup>3+</sup>-doped FCZ glasses [26].

There is a systematic increase in linewidth with decreasing annealing temperature. However, some XRD patterns show reflections that cannot be assigned to hexagonal or orthorhombic phase barium halide nanocrystals, indicating a negligible concentration of additional phases. The origin of these reflections is unclear. The XRD reflections are wider than the instrumental resolution, suggesting size-broadening effects.

#### 4. Crystallization processes in rare-earth doped glasses

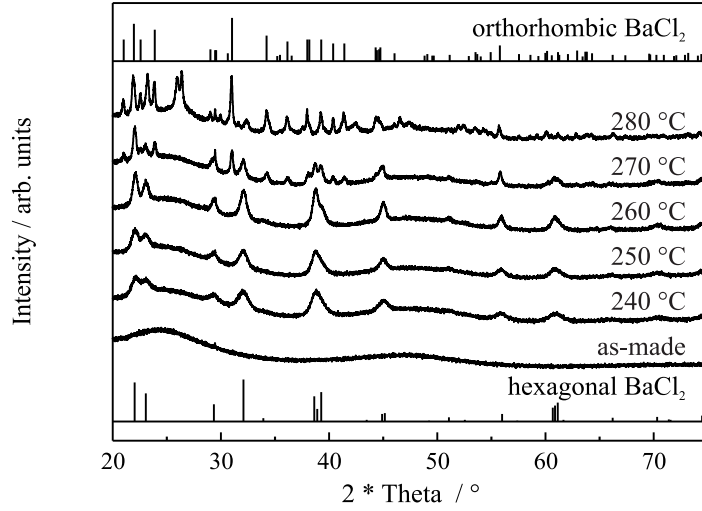


Figure 4.4.: XRD data of the 1 mol%  $\text{Nd}^{3+}$ -doped FCZ glasses and glass ceramics. From bottom to top: as-made FCZ and FCZ annealed at 240, 250, 260, 270, and 280 °C. The diffraction patterns are vertically displaced for clarity. The line patterns of hexagonal phase  $\text{BaCl}_2$  (PDF 45-1313) and orthorhombic phase  $\text{BaCl}_2$  (PDF 24-0094) are shown for comparison.

Although the XRD linewidths of the bigger orthorhombic barium halide nanocrystals are too close to the instrumental resolution to allow a precise estimate of the particle size, the Scherrer analysis of the XRD pattern provides a first estimate. The crystallite sizes were determined with the Scherrer formula (see Section 3.3), assuming no stress or strain effects. The Scherrer formula is applied to the reflection at about  $32^\circ$  and  $31^\circ$  of hexagonal and orthorhombic  $\text{BaCl}_2$ , respectively. The line profile is fitted by a Lorentzian. The average nanocrystal diameters are listed in Table 4.3. The diameter of the  $\text{BaCl}_2$  crystals in the FCZ glasses is approximately 10 nm after annealing at 240 °C and 250 °C; annealing at 260 °C yields a slightly higher average crystallite diameter of about 15 nm. For processing temperatures of 270 °C and 280 °C, the crystals grow rapidly, and their diameter expands up to about 60 nm. There is a trend toward bigger crystals for higher annealing temperatures.

According to Ref. [62], the volume fractions of the  $\text{BaCl}_2$  nanocrystals in the glass ceramics are determined from the ratio of the area of the crystalline reflections and the total XRD graph area including the broad amorphous glass bands, whereas comparable X-ray absorption properties of the different materials and phases are assumed. The estimated volume fraction is given for the different heat-treated samples in Table 4.3; it is about 20 % for all glass ceramics indicating complete crystallization of the  $\text{BaCl}_2$ .

For completeness, the structural parameters are summarized in the following. The lattice constants of  $\text{BaCl}_2$  in hexagonal and orthorhombic symmetry are given in Table 4.4. These parameters taken from Haase *et al.* [25] are in

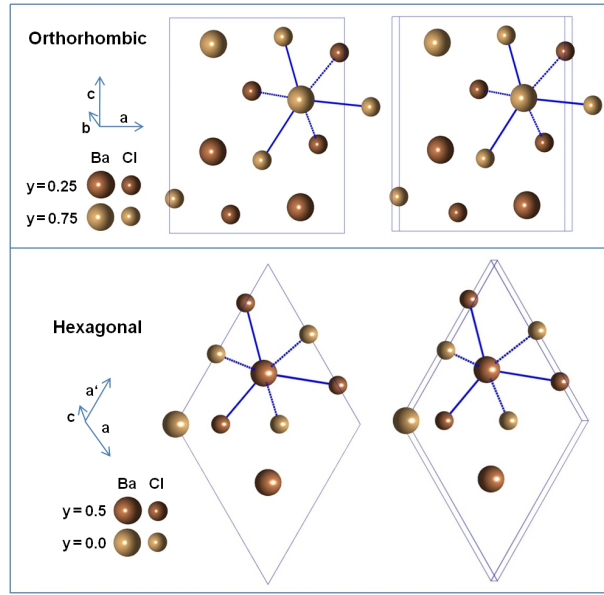


Figure 4.5.: Stereo view of atomic positions and unit cells of hexagonal (bottom) and orthorhombic (top)  $\text{BaCl}_2$ . The y numbers in the legends are the altitudes in the projection plane. Connecting bond lines between Ba and Cl atoms are added in order to emphasize the similarity of both structures [48].

Table 4.4.: Lattice constants of hexagonal ( $P\bar{6}2m$  structure) and orthorhombic ( $Pnma$  structure)  $\text{BaCl}_2$  [63].

structural group	$a$ ( $\text{\AA}$ )	$b$ ( $\text{\AA}$ )	$c$ ( $\text{\AA}$ )
$P\bar{6}2m$	8.11	8.11	4.65
$Pnma$	7.88	4.73	9.44

agreement with the XRD data and with calculations performed from DFT by structural relaxation in Bohley *et al.* [48]. Figure 4.5 shows a stereo view of the atomic positions in the corresponding cells [48]. The unit cell of orthorhombic  $\text{BaCl}_2$  contains four formula units (four Ba and eight Cl atoms), while the unit cell of hexagonal  $\text{BaCl}_2$  contains three  $\text{BaCl}_2$  units (three Ba and six Cl atoms). Each  $\text{Ba}^{2+}$  ion has nine neighboring  $\text{Cl}^-$  ions; three of which in the same crystallographic plane (projection plane in Figure 4.5), three are lying in a plane behind, and three lie in a plane in front of that plane. Figure 4.6 shows the glass structure of a typical FZ-based glass doped with trivalent rare-earth ions ( $\text{Eu}^{3+}$ -doped ZBLAN) taken from Ref. [61]. The structure is comparable to that of the present FCZ base glass in which the  $\text{BaCl}_2$  nanocrystals are embedded as the Raman investigations of the FZ and FCZ glasses in Chapter 6 show. A more detailed structural investigation is outside the scope of this work.

#### 4. Crystallization processes in rare-earth doped glasses

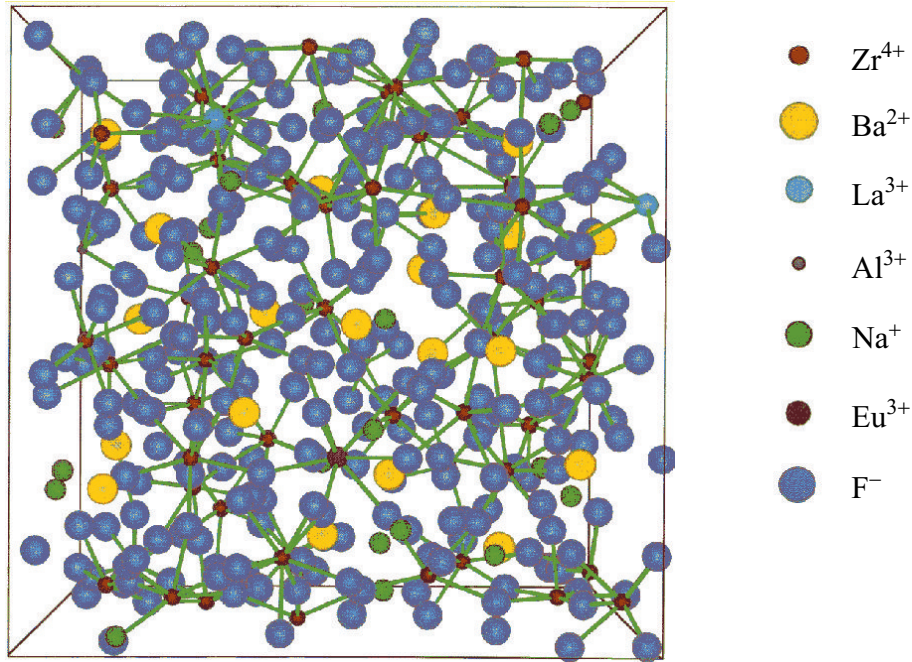


Figure 4.6.: Atomic positions in an Eu<sup>3+</sup>-doped ZBLAN glass [61].

### 4.3. Influence of the rare-earth ions on the crystallization

BaCl<sub>2</sub> crystallization was also found for rare-earth free FCZ glasses and in FCZ glasses doped with other rare-earths such as Eu and Er [53, 64]. However, the crystallization behavior depends on the rare-earth ion and rare-earth doping level used. In particular, the BaCl<sub>2</sub> crystallization and the phase transition are found at other annealing temperatures, which overlap in some cases with the partial glass crystallization [53, 64]. In Ref. [65], in which the crystallization behavior of comparable FCZ glasses is investigated, it is found that rare-earth doping decreases the apparent activation energy  $E_a$  and increases the Ruby constant  $H_r$  of the BaCl<sub>2</sub> crystallization compared to undoped FCZ glasses. In that study, an activation energy of 260 kJ/mol was found for rare-earth free FCZ glasses, which is slightly above the activation energy of the 1 mol% Nd<sup>3+</sup>-doped FCZ glass determined in Section 4.2 to be about 250 kJ/mol. A significantly lower activation energy of approximately 210 kJ/mol was found for a 5 mol% Nd<sup>3+</sup>-doped FCZ glass [58]. For the rare-earths investigated, Nd, Eu, Gd, Tb, and Er, Paßlick's study shows that the activation energy increases with the rare-earth' atomic number with the exception of europium. Usually, rare-earths occur as trivalent ions since they are most stable in this configuration as they can easily lose three valence electrons. The investigation of the MPR dynamics of Nd<sup>3+</sup> in the FCZ glass ceramics, is a step in obtaining a deeper understanding whether trivalent rare-earth ions are incorporated into the BaCl<sub>2</sub>

### 4.3. Influence of the rare-earth ions on the crystallization

nanocrystals. However, due to their electronic configuration Eu, Sm, and Yb can occur as trivalent as well as divalent ions [66]. Thus, the oxidation state is important here, and is investigated by Mössbauer spectroscopy in the last chapter for europium doped glass ceramics. It was already shown for  $\text{Eu}^{2+}$  that it can be incorporated into the  $\text{BaCl}_2$  nanocrystals leading to enhanced  $\text{Eu}^{2+}$  PL and interesting scintillation and storage phosphor properties.



## 5. Investigations on luminescence properties and relaxation dynamics

The influence of the  $\text{BaCl}_2$  nanocrystals on the rare-earth PL and MPR properties is investigated for  $\text{Nd}^{3+}$ -doped samples. In contrast to Nd, Eu is not suitable for the investigation of MPR processes due to its tendency to become divalent, changing its energy structure. As demonstrated in Figure 5.1 the nanocrystal formation causes increased  $\text{Nd}^{3+}$  PL intensities.

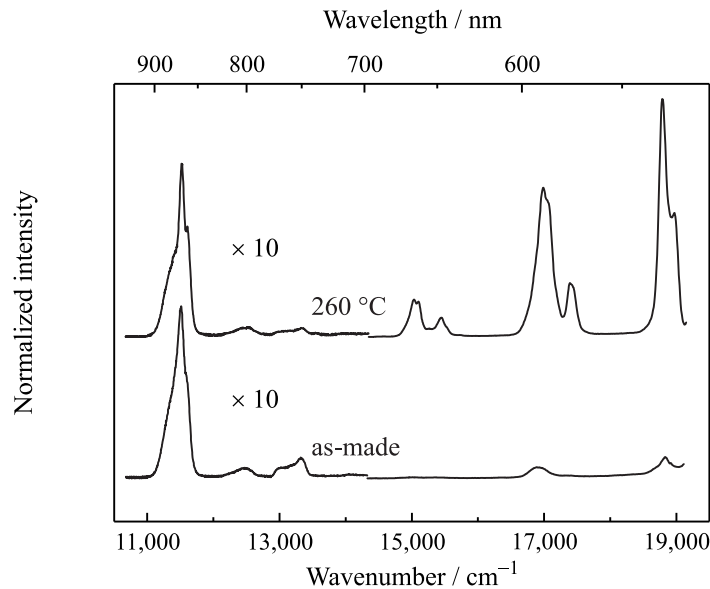


Figure 5.1.: PL spectra of 1 mol%  $\text{Nd}^{3+}$ -doped as-made FCZ and FCZ annealed at 260 °C with an excitation wavelength of 515 nm (for details see Section 5.2). The spectra are vertically displaced for clarity.

It will turn out in this chapter that the enhanced emissions exhibit significantly longer decay times implying improved MPR properties. The MPR rates of various  $\text{Nd}^{3+}$  levels are obtained from time-resolved PL measurements. Different analyzing methods are used for a comprehensive investigation of the MPR properties. Using appropriate experimental conditions such as weak pulsed excitation and low rare-earth doping concentration, interfering processes that can also influence the time dependence become negligible. Since such a glass ceramic is a combined system of the base glass and the embedded nanocrystals, special attention must be paid to isolate the effects caused by the nanocrystals from those of the base glass. Thus, always an as-made glass is investigated as a nanocrystal-free reference sample. Some parts and figures of this chapter have already been published in Refs. [67, 68].

## 5.1. Spectroscopic properties of Nd<sup>3+</sup>

In order to determine the spectral positions of the Nd<sup>3+</sup> absorption lines that are important for the following PL measurements, the transmission spectra of the 1 mol% Nd<sup>3+</sup>-doped FCZ samples series are measured (Figure 5.2). Table 5.1 lists the deduced Nd<sup>3+</sup> energy level positions, together with the assignments to the corresponding optical transitions for the 260 °C FCZ glass ceramic. The level assignment is taken from Ref. [69].

The transmittance decreases with increasing annealing temperature; this is related to the increasing BaCl<sub>2</sub> nanocrystal size. At about 400 nm, the UV absorption edge sets in. It results from electronic transitions within the glass network; the absorption sets in when the photon energy exceeds the band gap of the glass network. Due to the increasing glass absorption, the Nd<sup>3+</sup> energy levels above the <sup>2</sup>K<sub>15/2</sub> level are not suitable for an investigation of the PL properties and the MPR dynamics. Thus, only transitions between lower energy levels are analyzed.

Figure 5.3 shows the energy level scheme that results from the observed absorption transitions and from the energy levels and assignments given in Refs. [69] and [70]. The corresponding transitions are indicated for illustration. Nd<sup>3+</sup> has a typical discrete energy level scheme of a trivalent rare-earth ion with many transitions in the VIS and NIR range. This makes it suitable for the investigation of the MPR properties determined by the FZ-based glass and glass-ceramics hosts.

Figures 5.4 and 5.5 give an overview on the VIS and NIR respectively PL spectra of the 1 mol% Nd<sup>3+</sup>-doped FCZ sample series. The Nd<sup>3+</sup> PL is excited at 515 nm. All spectra are normalized to the 868 nm emission originating from the metastable <sup>4</sup>F<sub>3/2</sub> level, for which MPR processes are negligible due to its large energy separation to the next lower level. The corresponding emission intensity is expected to be approximately unaffected by host modifications (see below); this is verified by absolute quantum efficiency measurements in the next section. The optical transitions corresponding to the observed emissions are indicated in the energy level scheme in Figure 5.6. In the case of spectrally overlapping states <sup>2S+1</sup>L<sub>J</sub>, which have an energy separation in the order of  $k_B T$ , the level group is considered as a combined level  $j$ . In the following sections, all overlapping states are subsumed via commas and brackets in the notation, for example (<sup>4</sup>G<sub>5/2</sub>, <sup>2</sup>G<sub>7/2</sub>).

For several levels in the VIS, enhanced relative emissions intensities are found for the samples with hexagonal BaCl<sub>2</sub> nanocrystals. As can be seen in Figure 5.5, all emissions observed in the NIR originate from the metastable <sup>4</sup>F<sub>3/2</sub> level or from neighboring levels that are coupled to <sup>4</sup>F<sub>3/2</sub> via MPA processes (see Section 5.3). The intensities of these NIR emissions do not change relative to the 868 nm emission intensity.

### 5.1. Spectroscopic properties of Nd<sup>3+</sup>

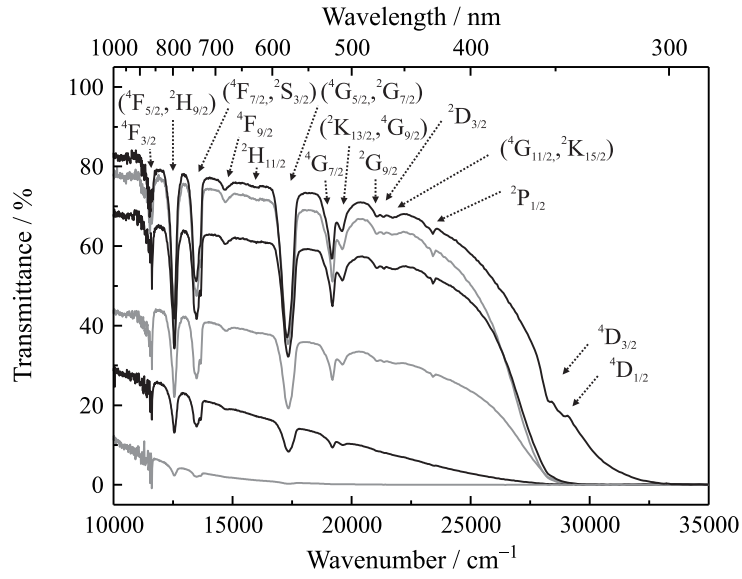


Figure 5.2.: Transmittance spectra of the 1 mol% Nd<sup>3+</sup>-doped FCZ glasses and glass ceramics. From top to bottom: as-made FCZ; FCZ annealed at 240, 250, 260, 270, and 280 °C. The final levels of the corresponding optical transitions in Nd<sup>3+</sup> are indicated; all transitions start at the <sup>4</sup>I<sub>9/2</sub> ground level. The sample thicknesses were 1.6±0.1 mm.

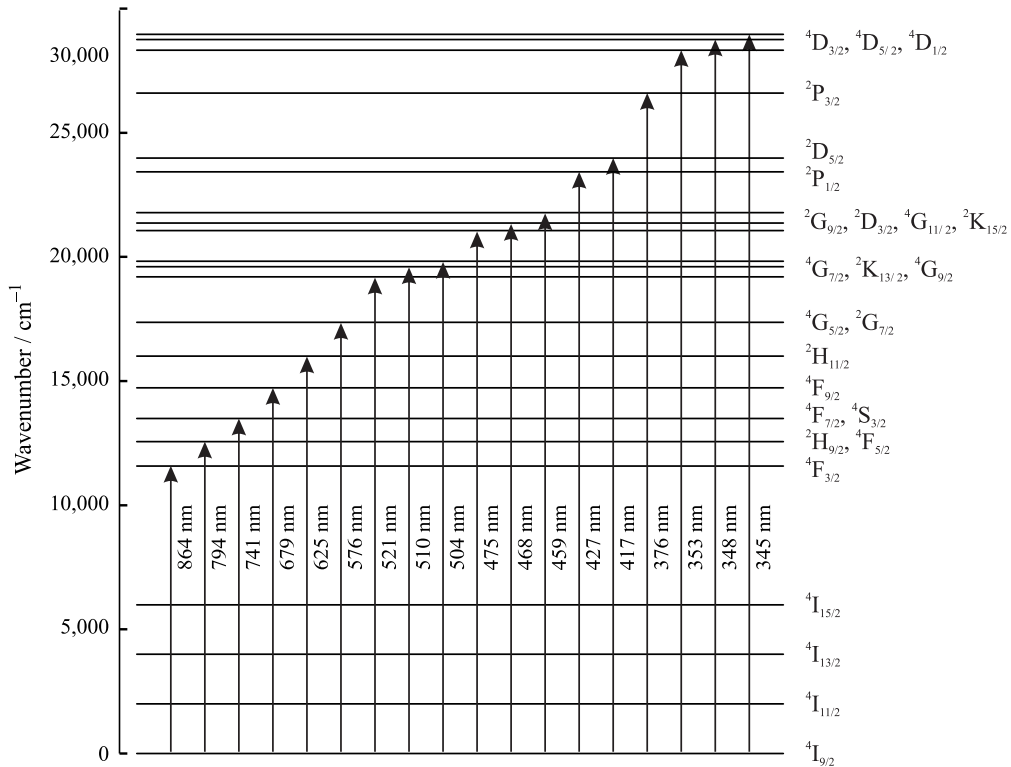


Figure 5.3.: Energy level scheme of Nd<sup>3+</sup> in the 1 mol% Nd<sup>3+</sup>-doped FCZ glass annealed at 260 °C based on the measured peak positions of the absorption bands. The absorption peak wavelengths and the corresponding optical transitions are indicated. The level assignment is taken from [69]; for the <sup>4</sup>I<sub>J</sub> levels see [70].

5. Investigations on luminescence properties and relaxation dynamics

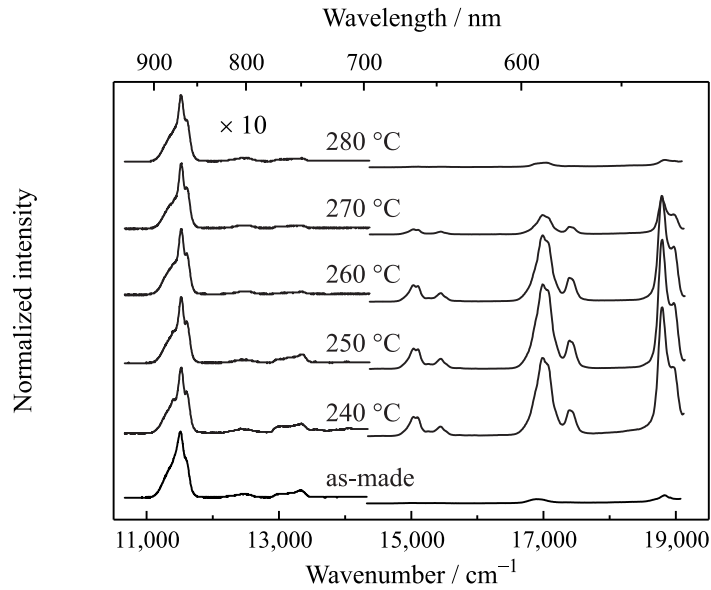


Figure 5.4.: PL spectra of the 1 mol%  $\text{Nd}^{3+}$ -doped FCZ glasses and glass ceramics. From bottom to top: as-made FCZ; FCZ annealed at 240, 250, 260, 270, and 280 °C.  $\text{Nd}^{3+}$  was excited at 515 nm in resonance with the  $^4\text{I}_{9/2}$  to ( $^4\text{G}_{7/2}$ ,  $^2\text{K}_{13/2}$ ,  $^4\text{G}_{9/2}$ ) transition. The spectra are normalized to the  $^4\text{F}_{3/2} \rightarrow ^4\text{I}_{9/2}$  emission at about 870 nm and vertically displaced for clarity.

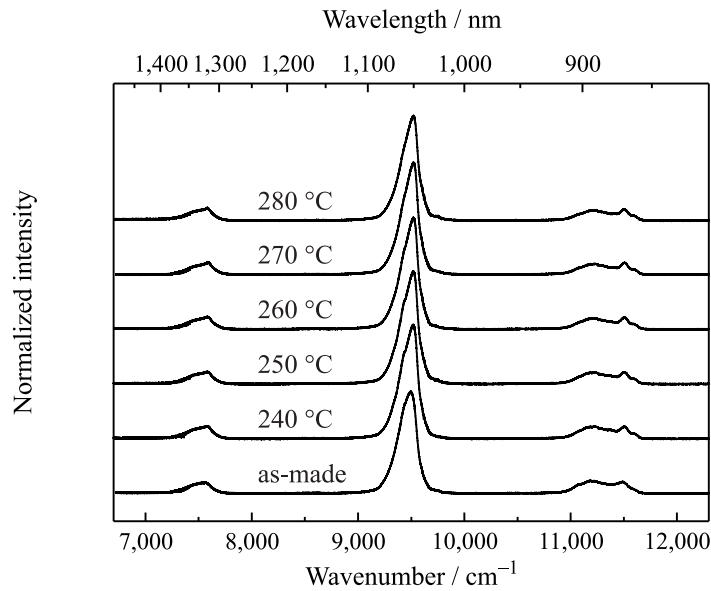


Figure 5.5.: PL spectra of the 1 mol%  $\text{Nd}^{3+}$ -doped FCZ glasses and glass ceramics in the NIR range. From bottom to top: as-made FCZ; FCZ annealed at 240, 250, 260, 270, and 280 °C.  $\text{Nd}^{3+}$  was excited at 515 nm in resonance with the  $^4\text{I}_{9/2}$  to ( $^4\text{G}_{7/2}$ ,  $^2\text{K}_{13/2}$ ,  $^4\text{G}_{9/2}$ ) transition. The spectra are normalized to the  $^4\text{F}_{3/2} \rightarrow ^4\text{I}_{9/2}$  emission at about 870 nm and vertically displaced for clarity.

### 5.1. Spectroscopic properties of Nd<sup>3+</sup>

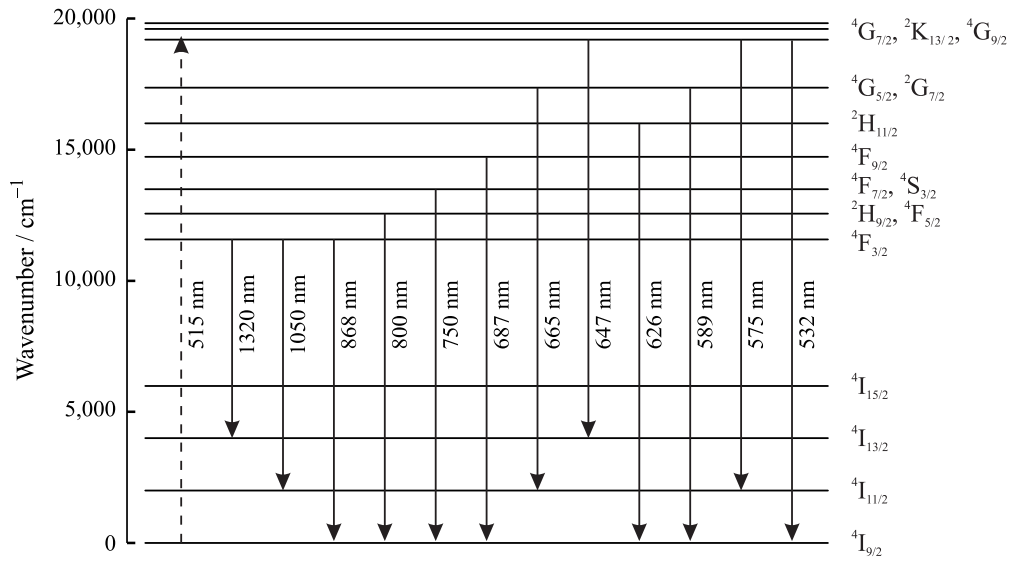


Figure 5.6.: Emissions bands (peak wavelengths indicated) corresponding to optical transitions of Nd<sup>3+</sup> in the 1 mol% Nd<sup>3+</sup>-doped FCZ glass annealed at 260 °C observed between 520 and 1500 nm. Nd<sup>3+</sup> was excited at 515 nm in resonance with the <sup>4</sup>I<sub>9/2</sub> to (<sup>4</sup>G<sub>7/2</sub>, <sup>2</sup>K<sub>13/2</sub>, <sup>4</sup>G<sub>9/2</sub>) transition. The assignment of the optical transitions is taken from [69].

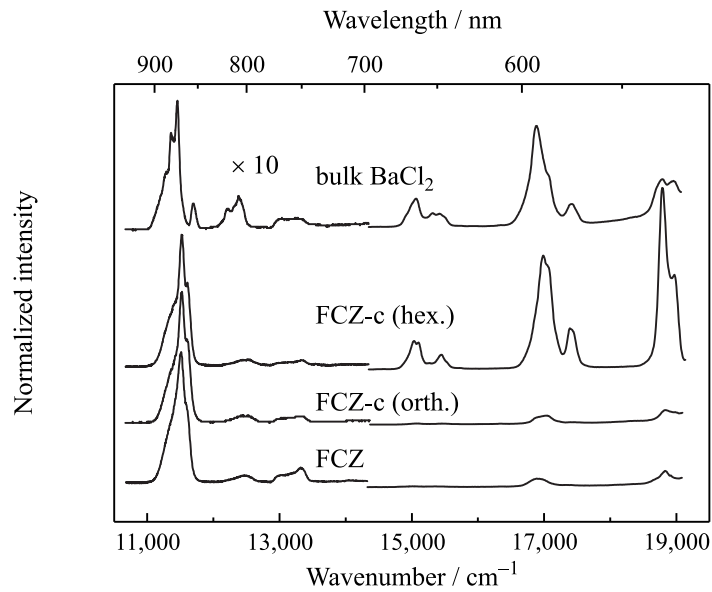


Figure 5.7.: PL spectra of the 1 mol% Nd<sup>3+</sup>-doped FCZ glasses and glass ceramics and of 100 ppm Nd<sup>3+</sup>-doped bulk BaCl<sub>2</sub>. From bottom to top: as-made FCZ; FCZ annealed at 260 °C (FCZ glass ceramic with hexagonal BaCl<sub>2</sub> nanocrystals) and 280 °C (FCZ glass ceramic with orthorhombic BaCl<sub>2</sub> nanocrystals); and bulk BaCl<sub>2</sub>. Nd<sup>3+</sup> was excited at 515 nm in resonance with the <sup>4</sup>I<sub>9/2</sub> to (<sup>4</sup>G<sub>7/2</sub>, <sup>2</sup>K<sub>13/2</sub>, <sup>4</sup>G<sub>9/2</sub>) transition. The spectra are normalized to the <sup>4</sup>F<sub>3/2</sub> → <sup>4</sup>I<sub>9/2</sub> emission at about 870 nm and vertically displaced for clarity.

## 5. Investigations on luminescence properties and relaxation dynamics

Table 5.1.: Observed peak positions of the  $\text{Nd}^{3+}$  absorption bands of the 1 mol%  $\text{Nd}^{3+}$ -doped FCZ glass annealed at 260 °C. The final levels of the corresponding optical transitions in  $\text{Nd}^{3+}$  are given; all transitions start at the  $^4\text{I}_{9/2}$  ground level. The assignment of the optical transitions is taken from Ref. [69].

level	wavenumber ( $\text{cm}^{-1}$ )	wavelength (nm)
$^4\text{F}_{3/2}$	11,574	864.0
$^2\text{H}_{9/2}, ^4\text{F}_{5/2}$	12,557	796.4
$^4\text{F}_{7/2}, ^4\text{S}_{3/2}$	13,490	741.3
$^4\text{F}_{9/2}$	14,728	679.0
$^2\text{H}_{11/2}$	16,000	625.0
$^4\text{G}_{5/2}, ^2\text{G}_{7/2}$	17,361	576.0
$^4\text{G}_{7/2}$	19,194	521.0
$^2\text{K}_{13/2}$	19,608	510.0
$^4\text{G}_{9/2}$	19,826	504.4
$^2\text{G}_{9/2}$	21,062	474.8
$^2\text{D}_{3/2}$	21,363	468.1
$^4\text{G}_{11/2}, ^2\text{K}_{15/2}$	21,787	459.0
$^2\text{P}_{1/2}$	23,425	426.9
$^2\text{D}_{5/2}$	23,981	417.0
$^2\text{P}_{3/2}$	26,603	375.9
$^4\text{D}_{3/2}$	28,329	353.0
$^4\text{D}_{5/2}$	28,752	347.8
$^4\text{D}_{1/2}$	28,969	345.2

Figure 5.7 compares the VIS PL spectra of  $\text{Nd}^{3+}$  in the as-made glass, in the 260 °C glass ceramic with hexagonal  $\text{BaCl}_2$  nanocrystals, in the 280 °C glass ceramic with orthorhombic  $\text{BaCl}_2$  nanocrystals, and in an orthorhombic bulk  $\text{BaCl}_2$  (doped with 100 ppm  $\text{Nd}^{3+}$ ) crystal. Whereas the VIS emissions are quenched in the as-made sample, these emissions are very intense in orthorhombic bulk  $\text{BaCl}_2$  as expected for such a low phonon energy crystal [71]. However, the PL intensities in the spectrum of the 280 °C glass ceramic are similar to those of the as-made glass indicating that the formation of orthorhombic  $\text{BaCl}_2$  nanocrystals does not cause a PL enhancement. The formation of hexagonal nanocrystals on the contrary, leads to a strong enhancement effect (see 260 °C glass ceramic). A direct comparison to  $\text{Nd}^{3+}$  in the corresponding bulk crystal is not possible since the hexagonal crystalline phase of  $\text{BaCl}_2$  is metastable and cannot be grown as bulk crystals. The PL enhancement caused by the nanocrystals is investigated in the following.

## 5.2. Luminescence enhancement

In order to get a quantitative estimate of the PL enhancement, absolute quantum yield measurements are performed on the Nd-doped sample series. The presented PL spectra are not corrected for the spectral dependencies (wavelength dependence of the grating efficiencies, of the imaging losses and of the photomultiplier sensitivity etc.) of the optical components in the used PL setup. Additionally, different scattering and transmission properties of the host materials can lead to different detected PL intensities independently from the radiative quantum efficiencies. To enable a comparison of luminescence enhancements of the different samples, all spectra are normalized to the  ${}^4F_{3/2} \rightarrow {}^4I_{9/2}$  emission at 868 nm. The efficiency of this emission is expected to be nearly unaffected by the host modifications, because of similar radiative rates and of negligible nonradiative losses caused by the large energy gap below  ${}^4F_{3/2}$  (see Section 8.4). This assumption can be verified by the absolute quantum yield measurements.

Spectral overlap of the emission bands and the spectral resolution of the used quantum yield measurement system (see Section 3.3.5) do not allow for isolated measurements of the single  $\text{Nd}^{3+}$  transitions. In particular, it is not possible to measure the emissions after direct level excitation (in resonance with the emitting level), because a certain minimum distance between excitation and emission wavelength is required to obtain a sufficient signal-to-noise-ratio. Under these conditions, the following two quantum efficiency measurements are found to be a good choice. In both cases, the PL is excited at  $\lambda_{\text{ex}} = 526$  nm, because the maximum of the efficient  ${}^4I_{9/2} \rightarrow ({}^4G_{7/2}, {}^2K_{13/2}, {}^4G_{9/2})$  excitation is found at that wavelength (corresponding excitation spectrum not shown). The absolute quantum efficiency  $\text{QE}(\lambda_{\text{ex}}, \lambda_{\text{em}})$  is estimated for two different detected spectral ranges, i.e. for  $\lambda_{\text{em},1} = 620\text{--}700$  nm and  $\lambda_{\text{em},2} = 840\text{--}940$  nm.  $\lambda_{\text{em},1}$  covers the  $({}^4G_{7/2}, {}^2K_{13/2}, {}^4G_{9/2}) \rightarrow {}^4I_{13/2}$  and the  $({}^4G_{5/2}, {}^2G_{7/2}) \rightarrow {}^4I_{11/2}$  emission centered at 647 and 665 nm, respectively.  $\lambda_{\text{em},2}$  contains the  ${}^4F_{3/2} \rightarrow {}^4I_{9/2}$  emission centered at 868 nm.

The efficiencies of both spectral ranges are listed for the different 1 mol%  $\text{Nd}^{3+}$ -doped samples in Table 5.2. The absolute quantum efficiencies QE have the order of  $10^{-1}$  % and  $10^1$  % for  $\lambda_{\text{em},1}$  and  $\lambda_{\text{em},2}$ , respectively. The values for  $\lambda_{\text{em},1}$  are close to the sensitivity limit of the measurement system. The corresponding quantum efficiency of the standard 1 mol%  $\text{Nd}^{3+}$ -doped FZ glass is below the sensitivity limit and is thus not determinable. The relative enhancements of the heat-treated FCZ samples in comparison to the as-made FCZ sample are plotted in Figure 5.8. For  $\lambda_{\text{em},1}$ , the enhancement factor is larger than 6 in one sample. For  $\lambda_{\text{em},2}$  on the contrary, the factor does not exceed 1.3. This result confirms that the 868 nm emission is barely influenced by the host and legitimates the normalization of the PL spectra to this emission. The quantum efficiency enhancement found for  $\lambda_{\text{em},1}$  decreases with the

## 5. Investigations on luminescence properties and relaxation dynamics

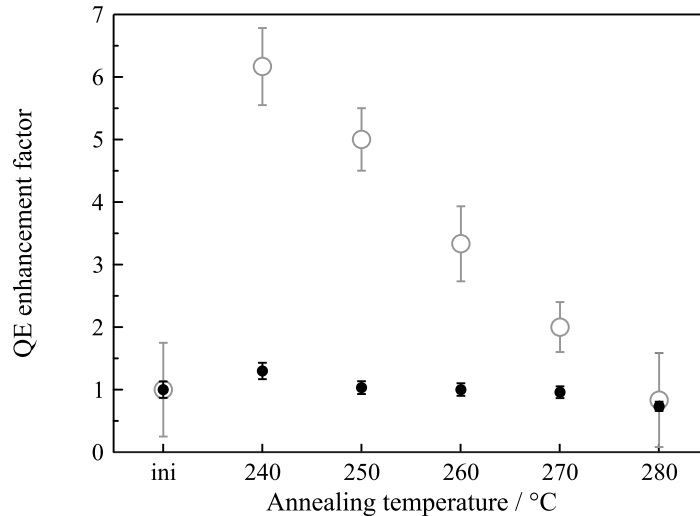


Figure 5.8.: Enhancement of the absolute quantum efficiency QE for 1 mol% Nd<sup>3+</sup>-doped FCZ annealed at different temperatures relative to 1 mol% Nd<sup>3+</sup>-doped as-made FCZ (ini). The absolute quantum efficiency was determined with an absolute quantum yield measurement system for a Nd<sup>3+</sup> excitation at  $\lambda_{\text{ex}} = 526$  nm and for two different detected spectral ranges  $\lambda_{\text{em},1} = 620 - 700$  nm (open circles) and  $\lambda_{\text{em},2} = 840 - 940$  nm (full circles).

Table 5.2.: Absolute quantum efficiency QE determined with an absolute quantum yield measurement system for 1 mol% Nd<sup>3+</sup>-doped as-made FCZ (ini) and FCZ annealed at different temperatures. The absolute quantum efficiency was measured for a Nd<sup>3+</sup> excitation at  $\lambda_{\text{ex}} = 526$  nm and for two different detected spectral ranges  $\lambda_{\text{em},1} = 620 - 700$  nm and  $\lambda_{\text{em},2} = 840 - 940$  nm.

annealing temperature (°C)	ini	240	250	260	270	280
QE( $\lambda_{\text{ex}}, \lambda_{\text{em},1}$ ) (%)	0.06	0.37	0.30	0.20	0.12	0.05
QE( $\lambda_{\text{ex}}, \lambda_{\text{em},2}$ ) (%)	9.7	12.6	10.0	9.7	9.3	7.1

annealing temperature, which is directly related to the nanocrystal size; this dependence is discussed in Section 8.2. The sample with the orthorhombic BaCl<sub>2</sub> nanocrystals does not show any efficiency enhancement; only samples with hexagonal BaCl<sub>2</sub> nanocrystals show an enhancement. This indicates that only the hexagonal nanocrystals, and not the orthorhombic ones are somehow associated with the Nd<sup>3+</sup> ions. This is also discussed in Section 8.2.

Table 5.3 compares the luminescence lifetime of the strongly enhanced ( ${}^4\text{G}_{5/2}, {}^2\text{G}_{7/2}$ )  $\rightarrow$   ${}^4\text{I}_{9/2}$  emission for all samples with hexagonal BaCl<sub>2</sub> nanocrystals. The time constant does not change significantly. This indicates that the difference in the PL enhancement of these samples is related to the different average nanocrystal sizes but not to different relaxation rates (see Section 8.2). Since the hexagonal nanocrystals lead to the largest PL enhancement, their influence is further investigated. For this purpose, the 260 °C sample is studied

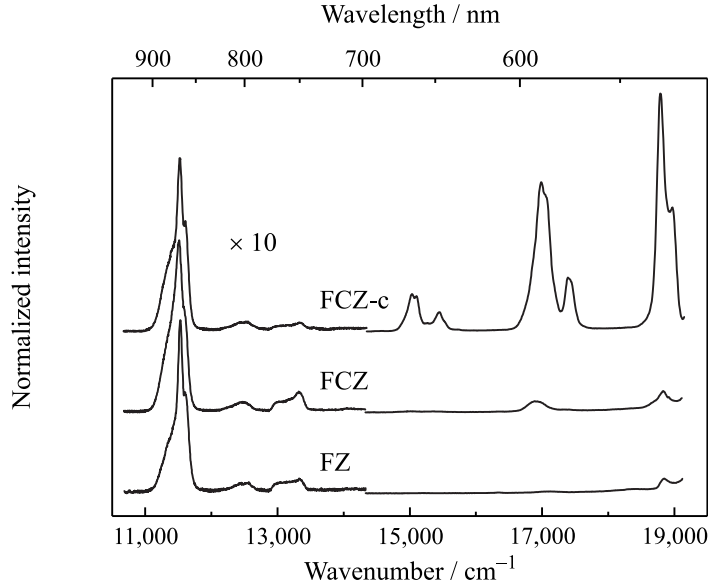


Figure 5.9.: PL spectra of the 1 mol%  $\text{Nd}^{3+}$ -doped FZ-based glasses and glass ceramics. From bottom to top: as-made FZ, as-made FCZ, and FCZ annealed at 260 °C (FCZ-c).  $\text{Nd}^{3+}$  was excited at 515 nm in resonance with the  ${}^4\text{I}_{9/2}$  to ( ${}^4\text{G}_{7/2}$ ,  ${}^2\text{K}_{13/2}$ ,  ${}^4\text{G}_{9/2}$ ) transition. The spectra are normalized to the  ${}^4\text{F}_{3/2} \rightarrow {}^4\text{I}_{9/2}$  emission at about 870 nm and vertically displaced for clarity.

Table 5.3.: Experimental PL decay time constant  $\tau_{\text{exp}}$  of the ( ${}^4\text{G}_{5/2}$ ,  ${}^2\text{G}_{7/2}$ )  $\rightarrow$   ${}^4\text{I}_{9/2}$  transition at 589 nm of  $\text{Nd}^{3+}$  in FCZ glass ceramics following direct pulsed excitation. The error for  $\tau_{\text{exp}}$  is between 10 % and 20 %. All samples are doped with 1 mol%  $\text{Nd}^{3+}$ ; they were annealed at different temperatures. All samples contain hexagonal  $\text{BaCl}_2$  nanocrystals; the average nanocrystal size increases with the annealing temperature.

annealing temperature (°C)	240	250	260
time constant ( $\mu\text{s}$ )	10.5	11.4	11.8

as a representative glass ceramic with hexagonal nanocrystals. In the following paragraphs, the glass ceramic (abbreviated as FCZ-c) refers to the sample heat-treated at 260 °C. Besides this FCZ glass ceramic, the as-made FCZ glass and the FZ glass with the standard ZBLAN composition are investigated as reference samples.

In Figure 5.9, the PL spectra of  $\text{Nd}^{3+}$  in the FZ and FCZ glasses as well as in the FCZ glass ceramic are shown. All spectra are recorded for excitation at 515 nm. The observed  $\text{Nd}^{3+}$  emissions and their corresponding transitions [69] are listed in Table 5.4. The PL emissions at about 532, 575, 589, 647, and 665 nm, which originate from the ( ${}^4\text{G}_{5/2}$ ,  ${}^2\text{G}_{7/2}$ ) and ( ${}^4\text{G}_{7/2}$ ,  ${}^2\text{K}_{13/2}$ ,  ${}^4\text{G}_{9/2}$ ) excited levels, become slightly pronounced by the addition of chlorine to the FZ glass, but get strongly enhanced by the formation of the  $\text{BaCl}_2$  nanocrystals within the FCZ glass. The energy gaps below the levels ( ${}^4\text{G}_{5/2}$ ,  ${}^2\text{G}_{7/2}$ )

## 5. Investigations on luminescence properties and relaxation dynamics

Table 5.4.: Peak positions of the  $\text{Nd}^{3+}$  emission bands of the 1 mol%  $\text{Nd}^{3+}$ -doped FCZ glass annealed at 260 °C observed between 520 and 950 nm under excitation at 515 nm. The assignment of the optical transitions is taken from Ref. [69].

transition	wavenumber ( $\text{cm}^{-1}$ )	wavelength (nm)
${}^4\text{F}_{3/2} \rightarrow {}^4\text{I}_{9/2}$	11,520	868
$({}^2\text{H}_{9/2}, {}^4\text{F}_{5/2}) \rightarrow {}^4\text{I}_{9/2}$	12,500	800
$({}^4\text{F}_{7/2}, {}^4\text{S}_{3/2}) \rightarrow {}^4\text{I}_{9/2}$	13,330	750
${}^4\text{F}_{9/2} \rightarrow {}^4\text{I}_{9/2}$	14,560	687
$({}^4\text{G}_{5/2}, {}^2\text{G}_{7/2}) \rightarrow {}^4\text{I}_{11/2}$	15,040	665
$({}^4\text{G}_{7/2}, {}^2\text{K}_{13/2}, {}^4\text{G}_{9/2}) \rightarrow {}^4\text{I}_{13/2}$	15,460	647
${}^2\text{H}_{11/2} \rightarrow {}^4\text{I}_{9/2}$	15,970	626
$({}^4\text{G}_{5/2}, {}^2\text{G}_{7/2}) \rightarrow {}^4\text{I}_{9/2}$	16,980	589
$({}^4\text{G}_{7/2}, {}^2\text{K}_{13/2}, {}^4\text{G}_{9/2}) \rightarrow {}^4\text{I}_{11/2}$	17,390	575
$({}^4\text{G}_{7/2}, {}^2\text{K}_{13/2}, {}^4\text{G}_{9/2}) \rightarrow {}^4\text{I}_{9/2}$	18,800	532

and  $({}^4\text{G}_{7/2}, {}^2\text{K}_{13/2}, {}^4\text{G}_{9/2})$  are relatively small, namely about  $1,360 \text{ cm}^{-1}$  and  $1,830 \text{ cm}^{-1}$ , respectively, so that emissions from these levels are usually quenched by MPR. In halide glasses, the MPR rates for such small energy separations are typically between  $10^6$  and  $10^7 \text{ s}^{-1}$  [39]. However, the radiative decay rates for  $4f$ -transitions in trivalent rare-earth ions, are typically between  $10^3$  and  $10^5 \text{ s}^{-1}$  and do not depend significantly on the host material [27, 28]. Thus, in halide glasses, the nonradiative decay is about two orders of magnitude faster than the radiative decay resulting in PL quenching as observed for the as-made FCZ and FZ glasses. The reduced PL quenching in the FCZ glass ceramic indicates reduced MPR rates that are investigated in the following sections.

### 5.3. Luminescence decay times

To analyze the strong PL enhancement in the heat-treated glass and the MPR processes involved, the time dependence of (the populations of) the  $\text{Nd}^{3+}$  levels is investigated. The decay time constants  $\tau_{\text{exp}}$  are determined from PL decays following direct pulsed excitation. The fitting results are collected in Table 5.5; the uncertainty of  $\tau_{\text{exp}}$  is between 10 % and 40 %. For all measurements, the average decay time constant is given. Most decays display mono-exponential time dependencies. Partially observed slight deviations from mono-exponential decay behavior are not further analyzed and are negligible for the analysis of the MPR rates.

To determine the MPR rates for the various  $\text{Nd}^{3+}$  levels, the observed PL decays are analyzed. According to Equation 2.1, the luminescence lifetime  $\tau_{\text{exp}}$  of an excited level  $j$  is given by the radiative and the nonradiative decay rates from level  $j$ . Besides MPR, nonradiative decays may include ion-ion

### 5.3. Luminescence decay times

Table 5.5.: Room temperature optical transition parameters of different  $\text{Nd}^{3+}$  levels in 1 mol%  $\text{Nd}^{3+}$ -doped FZ glass, FCZ glass, and FCZ glass annealed at 260 °C (FCZ-c): energy gaps to the next lower levels  $\Delta E$ , experimental decay time constants  $\tau_{\text{exp}}$ , total (Boltzmann weighted for level groups) radiative decay rates  $\sum A$  [72], and MPR rates  $W_{\text{MPR}}$  (for details see text).

level	sample	$\Delta E$ ( $\text{cm}^{-1}$ )	$\tau_{\text{exp}}$ ( $\mu\text{s}$ )	$\sum A$ $\text{s}^{-1}$	$W_{\text{MPR}}$ $\text{s}^{-1}$	comment
${}^4\text{F}_{3/2}$	FZ	5,547	450	2,165	$<10^3$	$W_{\text{MPR}} \ll \sum A$
	FCZ	5,544	370	2,591	$<10^3$	$W_{\text{MPR}} \ll \sum A$
	FCZ-c	5,584	360	2,849	$<10^3$	$W_{\text{MPR}} \ll \sum A$
$({}^2\text{H}_{9/2}, {}^4\text{F}_{5/2})$	FZ	1,029	460*	1,650	*	
	FCZ	1,010	370*	1,912	*	
	FCZ-c	982	360*	2,079	$3.2 \cdot 10^{5**}$	decay time, Fig. 5.13
$({}^4\text{F}_{7/2}, {}^4\text{S}_{3/2})$	FZ	928	440*	3,012	*	
	FCZ	935	360*	3,289	*	
	FCZ-c	933	390*	3,390	*	
${}^4\text{F}_{9/2}$	FZ	1,275	-	2,105	-	
	FCZ	1,216	-	2,242	-	
	FCZ-c	1,238	50*	2,283	*	
${}^2\text{H}_{11/2}$	FZ	1,221	-	212	-	
	FCZ	1,292	-	255	-	
	FCZ-c	1,272	-	251	-	
$({}^4\text{G}_{5/2}, {}^2\text{G}_{7/2})$	FZ	1,347	0.2	7,194	$5.0 \cdot 10^6$	decay time, Fig. 5.10
	FCZ	1,359	2	8,696	$4.9 \cdot 10^5$	decay time, Fig. 5.10
	FCZ-c	1,361	12	8,197	$7.5 \cdot 10^4$ $7.8 \cdot 10^4$	decay time, Fig. 5.10 temp. dep., Fig. 5.18
$({}^4\text{G}_{7/2}, {}^2\text{K}_{13/2}, {}^4\text{G}_{9/2})$	FZ	1,842	0.9	1,923	$1.1 \cdot 10^6$	decay time, Fig. 5.11
	FCZ	1,829	17	2,242	$5.7 \cdot 10^4$	decay time, Fig. 5.11
	FCZ-c	1,833	85	2,119	$9.7 \cdot 10^3$ $2.2 \cdot 10^4$	decay time, Fig. 5.11 rise time, Fig. 5.15
$({}^2\text{G}_{9/2}, {}^2\text{D}_{3/2}, {}^4\text{G}_{11/2}, {}^2\text{K}_{15/2})$	FZ	1,236	-	1,767	-	
	FCZ	1,236	-	2,037	-	
	FCZ-c	1,236	-	2,008	$1.8 \cdot 10^5$	rise time, Fig. 5.14

\* The marked levels show distorted decay times, because of their coupling to the metastable  ${}^4\text{F}_{3/2}$  level. Their MPR rates cannot be determined from room temperature decay times.

\*\* The MPR rate of the  $({}^2\text{H}_{9/2}, {}^4\text{F}_{5/2})$  level was determined from the 10 K decay time measurement ( $W_{\text{MPR}}(10 \text{ K}) = 5.4 \cdot 10^4 \text{ s}^{-1}$ ). The  $W_{\text{MPR}}$  given in the table is the corrected room temperature value.

## 5. Investigations on luminescence properties and relaxation dynamics

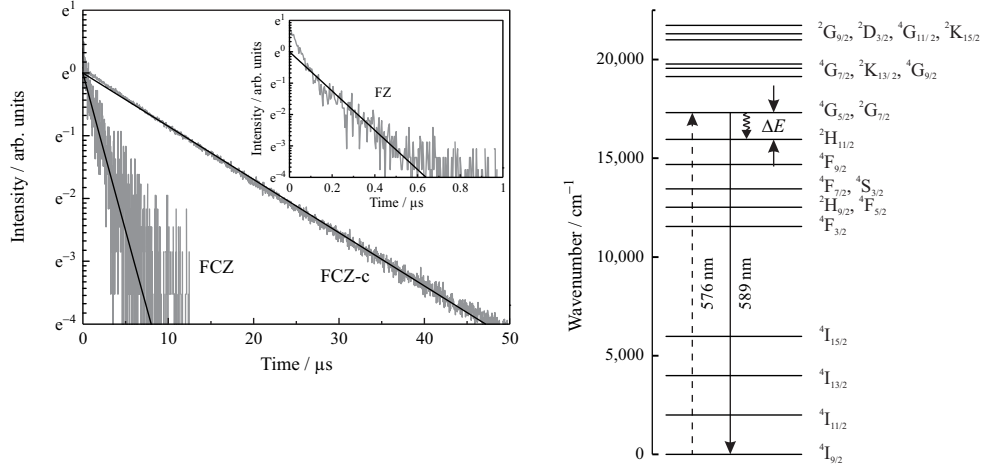


Figure 5.10.: PL decay of the ( ${}^4G_{5/2}$ ,  ${}^2G_{7/2}$ )  $\rightarrow$   ${}^4I_{9/2}$  transition at 589 nm of  $Nd^{3+}$  in as-made FZ, as-made FCZ, and in the FCZ glass annealed at 260 °C (FCZ-c) following direct pulsed excitation. All samples are doped with 1 mol%  $Nd^{3+}$ . The wavy arrow in the energy level scheme indicates the MPR analyzed.

interactions. In the present case, however, ion-ion interactions are negligible due to the relatively low  $Nd^{3+}$  doping level of 1 mol% [39]. Lifetime measurements on a glass with a  $Nd^{3+}$  doping level of 0.1 mol% provided the same time constants (see below) confirming that ion-ion interactions can be neglected. The MPR rate of a particular level  $j$  is determined by the MPR decay to the next lower level. Neglecting ion-ion interactions, the MPR rate of level  $j$  can be estimated from the observed level lifetime  $\tau_{exp}$  via (see Equation 2.1)

$$W_{MPR} = \tau_{exp}^{-1} - \sum A. \quad (5.1)$$

$\sum A$  is the level's total radiative decay rate, which can be calculated from absorption spectra using Judd-Ofelt theory [36, 37]. The total radiative decay rates of the analyzed  $Nd^{3+}$  levels are listed in Table 5.5; the calculations were done elsewhere [72]. Their uncertainty is 10 to 20 %. In case of overlapping states  ${}^{2S+1}L_J$ , which have an energy separation in the order of  $k_B T$ ,  $\sum A$  is the Boltzmann weighted common radiative decay rate of the level group, which is considered as a combined level  $j$ . The MPR rates obtained from Equation 5.1 are given in Table 5.5 together with the energy gaps  $\Delta E$ . The latter were determined from the peak positions of absorption lines (see Section 5.1).

Figure 5.10 and 5.11 show the luminescence decay of the ( ${}^4G_{5/2}$ ,  ${}^2G_{7/2}$ )  $\rightarrow$   ${}^4I_{9/2}$  and of the ( ${}^4G_{7/2}$ ,  ${}^2K_{13/2}$ ,  ${}^4G_{9/2}$ )  $\rightarrow$   ${}^4I_{9/2}$  emission at 589 nm and 532 nm, respectively. In order to illustrate that ion-ion interactions are negligible for the investigated 1.0 mol%  $Nd^{3+}$ -doped samples, a comparison between the luminescence lifetime of the ( ${}^4G_{5/2}$ ,  ${}^2G_{7/2}$ )  $\rightarrow$   ${}^4I_{9/2}$  transition in the 1.0 mol%  $Nd^{3+}$ -doped glass ceramic and the the 0.1 mol%  $Nd^{3+}$ -doped glass ceramic is presented in Figure 5.12. Figure 5.13 shows the luminescence decay of the

### 5.3. Luminescence decay times

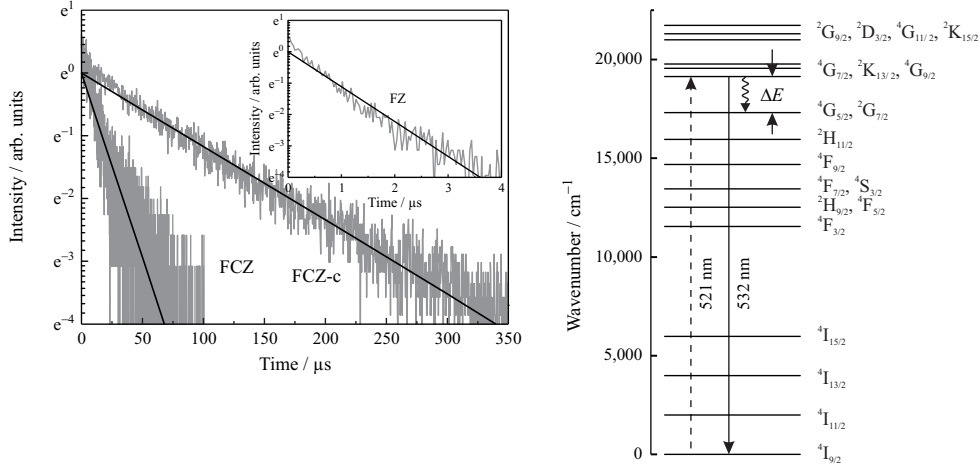


Figure 5.11.: PL decay of the ( ${}^4G_{7/2}$ ,  ${}^2K_{13/2}$ ,  ${}^4G_{9/2}$ )  $\rightarrow$   ${}^4I_{9/2}$  transition at 532 nm of  $Nd^{3+}$  in as-made FZ, as-made FCZ, and in the FCZ glass at 260 °C (FCZ-c) following direct pulsed excitation. All samples are doped with 1 mol%  $Nd^{3+}$ . The wavy arrow in the energy level scheme indicates the MPR analyzed.

( ${}^2H_{9/2}$ ,  ${}^4F_{5/2}$ )  $\rightarrow$   ${}^4I_{9/2}$  transition at 800 nm for the FCZ glass ceramic. Since the ( ${}^2H_{9/2}$ ,  ${}^4F_{5/2}$ ) level is coupled to the  ${}^4F_{3/2}$  level at room temperature, the luminescence decay measurement was repeated at low temperature. The solid lines represent the corresponding mono-exponential fit to the experimental data. The excitation routes are indicated in the corresponding energy level schemes.

The luminescence decay times of the ( ${}^4G_{5/2}$ ,  ${}^2G_{7/2}$ ) and the ( ${}^4G_{7/2}$ ,  ${}^2K_{13/2}$ ,  ${}^4G_{9/2}$ ) levels change significantly with the sample (Figure 5.10 and 5.11). The deduced MPR rates for these levels in the FZ glass sample correspond well to literature values for the given energy gaps in FZ-based glasses [39, 73, 74].

For the FCZ glass, lower MPR rates than in the FZ glass are calculated. In contrast to the MPR rates, the radiative decay rates do not change significantly with the sample (see Table 5.5). This is a general phenomenon of rare-earths and the same order of magnitude is found in other glasses and in crystals [27]. The lowest MPR rates for the ( ${}^4G_{5/2}$ ,  ${}^2G_{7/2}$ ) and ( ${}^4G_{7/2}$ ,  ${}^2K_{13/2}$ ,  ${}^4G_{9/2}$ ) levels belong to the FCZ glass ceramic explaining the significant luminescence enhancement in this sample.

The estimated decay time constant  $\tau_{exp}$  of the  ${}^4F_{3/2}$  level varies only slightly with the sample composition. The  ${}^4F_{3/2}$  level has an energy gap of about  $5,600\text{ cm}^{-1}$ . For such large energy gaps the MPR rate is negligibly small ( $W_{MPR} \ll A$ ). We found that the  ${}^4F_{3/2}$  level lifetime does not depend on temperature (measured between 10 and 300 K), which is evident when MPR is negligible. Thus, the observed decay time constant of the  ${}^4F_{3/2}$  level directly gives its radiative decay rate and the MPR rate listed is an upper limit. The observed decay time constants of the  ${}^4F_{3/2}$  level correspond well to the calculated radiative decay rates (see Table 5.5). The latter is slightly higher in the

## 5. Investigations on luminescence properties and relaxation dynamics

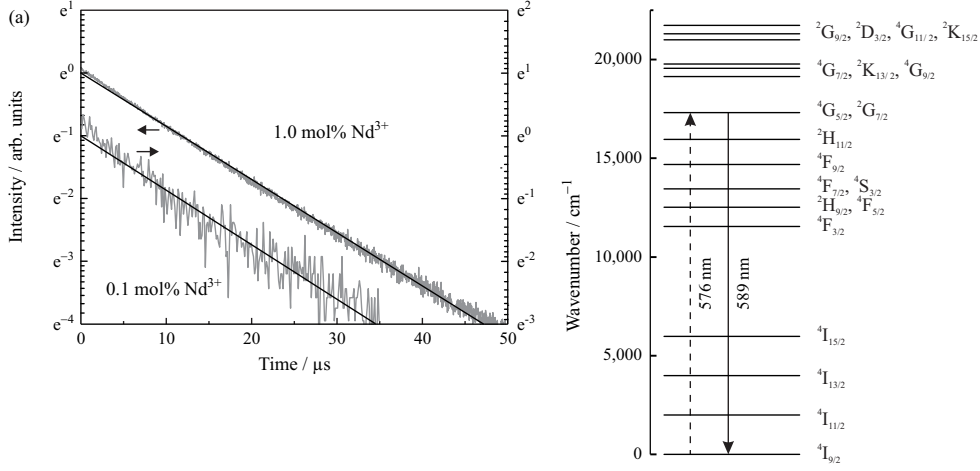


Figure 5.12.: Comparison of the PL decay of the ( ${}^4G_{5/2}$ ,  ${}^2G_{7/2}$ )  $\rightarrow$   ${}^4I_{9/2}$  transition at 589 nm of  $\text{Nd}^{3+}$  in FCZ glasses annealed at 260 °C with doping concentrations of 1.0 mol%  $\text{Nd}^{3+}$  (scale for the corresponding measurement on the left) and of 0.1 mol%  $\text{Nd}^{3+}$  (scale for the corresponding measurement on the right) following direct pulsed excitation.

FCZ than in the FZ glass and also barely influenced by the  $\text{BaCl}_2$  nanocrystals.

Due to its restriction to radiative decay,  ${}^4F_{3/2}$  is a long living state which becomes highly populated even at low pumping rates (storage level) in comparison to the other levels. The next two levels above  ${}^4F_{3/2}$ , i.e. ( ${}^2H_{9/2}$ ,  ${}^4F_{5/2}$ ) and ( ${}^4F_{7/2}$ ,  ${}^4S_{3/2}$ ), are strongly coupled to it via multiphonon processes in both directions. Although the probability of the MPA is typically  $10^2$  times (Boltzmann factor for the present energy gaps) lower than that of the inverse MPR process [75], MPA is not negligible in this case, because of the high population of  ${}^4F_{3/2}$ . The coupling of these levels causes them to show the same luminescence decay times like  ${}^4F_{3/2}$ . Also  ${}^4F_{9/2}$  might be populated via MPA. Thus, these levels show distorted decay times and their MPR rates cannot be reliably calculated from the simple relation in Equation 5.1.

However, MPA can be suppressed when going to low temperatures where no excited phonons exist. To determine the MPR rate for a small energy gap, the lifetime of the ( ${}^2H_{9/2}$ ,  ${}^4F_{5/2}$ ) level (gap of  $1,000 \text{ cm}^{-1}$ ) is measured at low temperature. Due to the suppressed MPA a shorter decay time constant ( $18 \mu\text{s}$  for the glass ceramic) is observed. This decay is directly given by the low temperature MPR and radiative decay rates. Thus, Equation 5.1 leads to the low temperature MPR rate. Subsequently, the corresponding room temperature MPR rate (Table 5.5) is calculated from the well-known temperature dependence of the MPR rate (see Section 5.5). In the FZ and FCZ glasses ( ${}^2H_{9/2}$ ,  ${}^4F_{5/2}$ ) does not show any PL at low temperature. This is evident as the corresponding, spontaneous MPR rates of fluoride glasses are high enough to cause luminescence quenching. This is the case in all samples for the  ${}^2H_{11/2}$  level and, together with its low radiative rates, render a lifetime analysis impossible.

## 5.4. Luminescence rise times

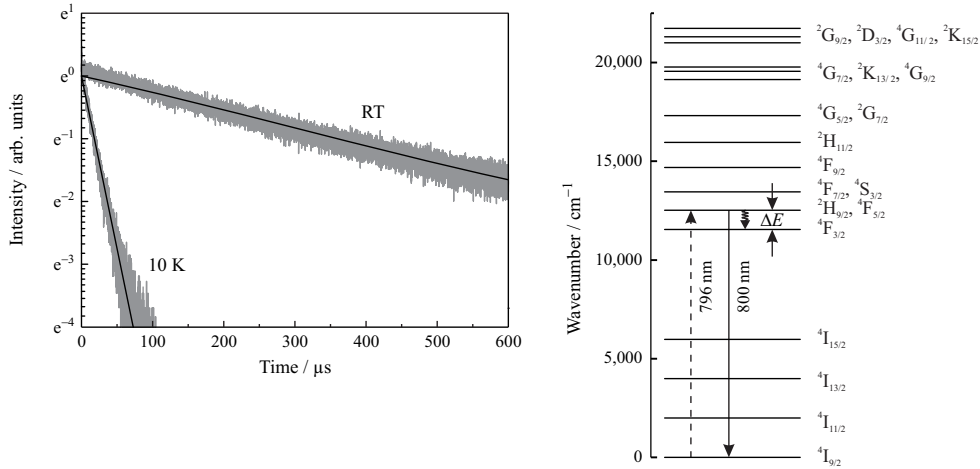


Figure 5.13.: PL decay of the (<sup>2</sup>H<sub>9/2</sub>, <sup>4</sup>F<sub>5/2</sub>) → <sup>4</sup>I<sub>9/2</sub> transition at 800 nm of Nd<sup>3+</sup> in the 1 mol% Nd<sup>3+</sup>-doped FCZ glass annealed at 260 °C following direct pulsed excitation. The measurements were done at room temperature and at 10 K. The wavy arrow in the energy level scheme indicates the MPR analyzed.

## 5.4. Luminescence rise times

Another possibility to estimate MPR rates is the analysis of PL rise times following excitation into higher levels. Figure 5.14 and Figure 5.15 show the time-dependent intensities of different Nd<sup>3+</sup> emissions following indirect pulsed excitation. The excitation routes are indicated in the corresponding energy level schemes. As visible from Figure 5.14, the FCZ glass ceramic shows a long buildup of the luminescence intensity in comparison to the corresponding as-made FCZ sample. In the glass ceramic, the intensity of the (<sup>4</sup>G<sub>7/2</sub>, <sup>2</sup>K<sub>13/2</sub>, <sup>4</sup>G<sub>9/2</sub>) → <sup>4</sup>I<sub>9/2</sub> emission increases relatively slowly after the excitation pulse, because the emitting level is populated from the next higher (<sup>2</sup>G<sub>9/2</sub>, <sup>2</sup>D<sub>3/2</sub>, <sup>4</sup>G<sub>11/2</sub>, <sup>2</sup>K<sub>15/2</sub>) level with a low MPR rate. In the as-made glass, the intensity increases nearly instantaneously with the excitation pulse due to the sample's higher MPR rate.

The excitation scheme for the <sup>4</sup>F<sub>9/2</sub> → <sup>4</sup>I<sub>9/2</sub> emission presented in Figure 5.15 also leads to a clearly visible buildup in the glass ceramic. Since emissions from the <sup>4</sup>F<sub>9/2</sub> level are strongly quenched in FZ-based glasses, the corresponding time dependence can not be measured for the as-made FCZ glass. Such arrangements can be considered as a three level system, where the ions get excited into the higher level 2 initially from where they decay nonradiatively into level 1; level 1 finally decays under radiative emission to the ground level 0.

5. Investigations on luminescence properties and relaxation dynamics

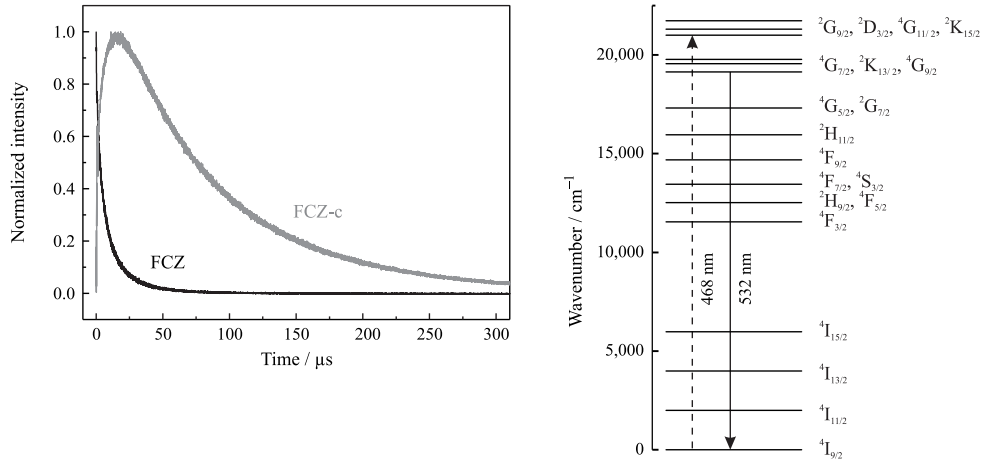


Figure 5.14.: Comparison of the time dependence (linear scale) of the PL intensity of the  $(^4\text{G}_{7/2}, ^2\text{K}_{13/2}, ^4\text{G}_{9/2}) \rightarrow ^4\text{I}_{9/2}$  transition at 532 nm following pulsed excitation into the  $(^2\text{G}_{9/2}, ^2\text{K}_{15/2}, ^2\text{D}_{3/2}, ^4\text{G}_{11/2})$  level of  $\text{Nd}^{3+}$  in the FCZ glass annealed at 260 °C (FCZ-c) and in as-made FCZ. Both samples are doped with 1 mol%  $\text{Nd}^{3+}$ .

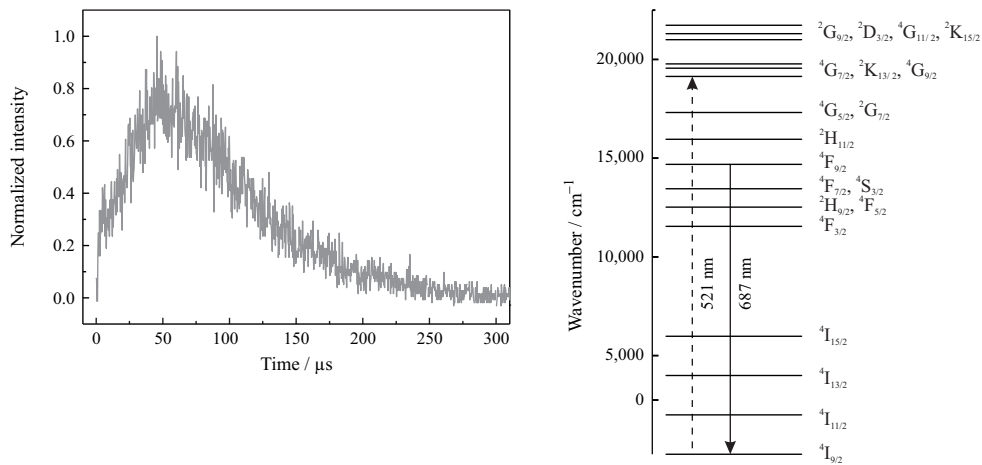


Figure 5.15.: Time dependence (linear scale) of the PL intensity of the  $^4\text{F}_{9/2} \rightarrow ^4\text{I}_{9/2}$  transition at 687 nm following pulsed excitation into the  $(^4\text{G}_{7/2}, ^2\text{K}_{13/2}, ^4\text{G}_{9/2})$  level of  $\text{Nd}^{3+}$  in the FCZ glass annealed at 260 °C (the corresponding emission is quenched in as-made FCZ). The sample is doped with 1 mol%  $\text{Nd}^{3+}$ .

## 5.4. Luminescence rise times

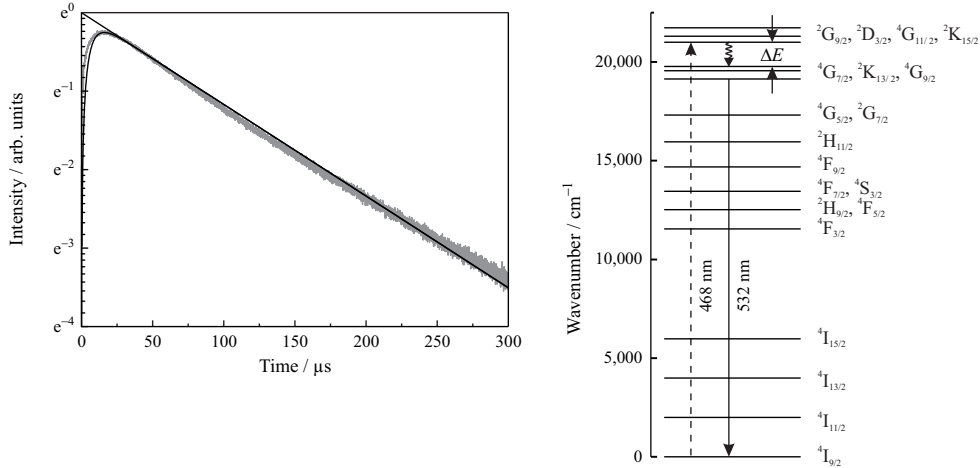


Figure 5.16.: Time dependence of the PL intensity of the  $(^4G_{7/2}, ^2K_{13/2}, ^4G_{9/2}) \rightarrow ^4I_{9/2}$  transition at 532 nm following pulsed excitation into the  $(^2G_{9/2}, ^2K_{15/2}, ^2D_{3/2}, ^4G_{11/2})$  level of  $\text{Nd}^{3+}$  in the FCZ glass annealed at 260 °C. The sample is doped with 1 mol%  $\text{Nd}^{3+}$ . The solid curve describes the time dependence via Equations 5.2 and 5.3. The wavy arrow in the energy level scheme indicates the MPR analyzed.

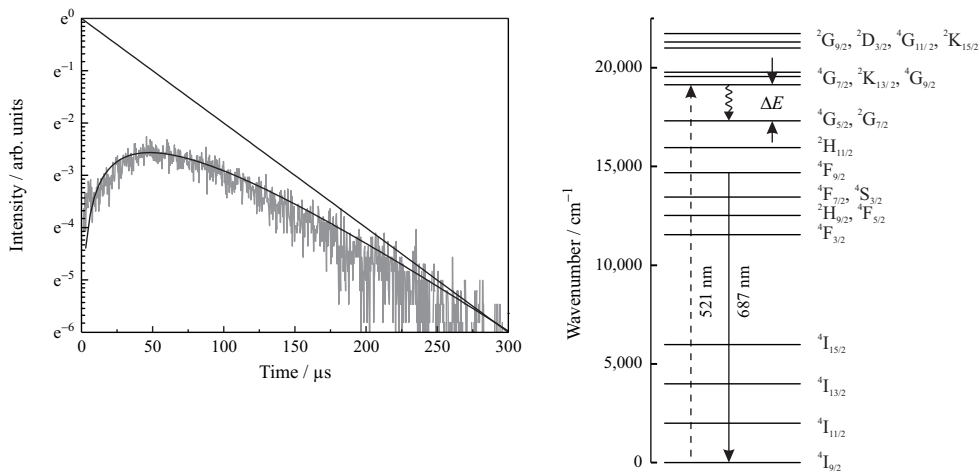


Figure 5.17.: Time dependence of the PL intensity of the  $^4F_{9/2} \rightarrow ^4I_{9/2}$  transition at 687 nm following pulsed excitation into the  $(^4G_{7/2}, ^2K_{13/2}, ^4G_{9/2})$  level of  $\text{Nd}^{3+}$  in the FCZ glass annealed at 260 °C. The sample is doped with 1 mol%  $\text{Nd}^{3+}$ . The solid curve describes the time dependence via Equations 5.2 and 5.3. The wavy arrow in the energy level scheme indicates the MPR analyzed.

## 5. Investigations on luminescence properties and relaxation dynamics

The solution of the corresponding rate equation system for level 1 gives the time dependence of the intensity  $I$ , i.e.

$$I(t) \propto \frac{W_2}{W_1 - W_2} \cdot (\exp(-W_2 \cdot t) - \exp(-W_1 \cdot t)), \quad (5.2)$$

where  $W_1$  is the total decay rate of level 1 and  $W_2$  is the nonradiative decay rate from level 2 to level 1. This function has a maximum at  $t_{\max}$ , which is given by

$$t_{\max} = \frac{\ln(W_2/W_1)}{W_2 - W_1}. \quad (5.3)$$

Both,  $t_{\max}$  and  $W_1$ , can be easily extracted from the measurement;  $W_1$  corresponds to the mono-exponential decay following the buildup, i.e.  $W_1 = \tau_{\text{exp}}^{-1}$ . Since level 2 can be assumed to decay only by MPR into level 1,  $W_2$  corresponds to the MPR rate  $W_{\text{MPR}}$ . The MPR rates estimated from the buildup analysis via Equation 5.3 are given in Table 5.5. The MPR rate of ( ${}^2\text{G}_{9/2}$ ,  ${}^2\text{D}_{3/2}$ ,  ${}^4\text{G}_{11/2}$ ,  ${}^2\text{K}_{15/2}$ ) is determined from the time dependence shown in Figure 5.14 (excitation of ( ${}^2\text{G}_{9/2}$ ,  ${}^2\text{D}_{3/2}$ ,  ${}^4\text{G}_{11/2}$ ,  ${}^2\text{K}_{15/2}$ ) and PL detection from ( ${}^4\text{G}_{7/2}$ ,  ${}^2\text{K}_{13/2}$ ,  ${}^4\text{G}_{9/2}$ )) with a  $t_{\max}$  of 16  $\mu\text{s}$ . The calculated time-dependent intensity, which results from the estimated rates using Equation 5.2, is shown in Figure 5.16 together with the corresponding measurement.

For excitation into the ( ${}^4\text{G}_{7/2}$ ,  ${}^2\text{K}_{13/2}$ ,  ${}^4\text{G}_{9/2}$ ) level and detection from level  ${}^4\text{F}_{9/2}$  (Figure 5.15), several energy gaps are bridged during the buildup. Thus, the detection level is populated via a multiphonon cascade (see corresponding excitation route). The buildup time is dominated by the MPR rate of the largest energy gap in the cascade whereas the influence of the MPR rates of the other energy gaps in the cascade can be neglected. The limiting gap is directly below ( ${}^4\text{G}_{7/2}$ ,  ${}^2\text{K}_{13/2}$ ,  ${}^4\text{G}_{9/2}$ ) and is about  $1,830 \text{ cm}^{-1}$ ;  $t_{\max}$  is 48  $\mu\text{s}$ . The evaluated MPR rate of ( ${}^4\text{G}_{7/2}$ ,  ${}^2\text{K}_{13/2}$ ,  ${}^4\text{G}_{9/2}$ ) is consistent with the rate estimated before from decay time analysis (see Table 5.5). In Figure 5.17 the measured time dependence is compared to the corresponding theoretical curve given by Equation 5.2.

### 5.5. Temperature dependence of the decay rates

To investigate the dependence of the transition rates on the phonon occupation number, the luminescence decay time constant of ( ${}^4\text{G}_{5/2}$ ,  ${}^2\text{G}_{7/2}$ ) is measured at different temperatures (see Figure 5.18). According to Equations 2.7 and 2.10 in Section 2.2.1, the temperature dependence of the MPR rate can be modeled by the Bose-Einstein-statistics via

$$W_{\text{MPR}}(T) = W_{\text{MPR},0} \cdot \left( \frac{\exp(\hbar\omega/k_B T)}{\exp(\hbar\omega/k_B T) - 1} \right)^{\frac{\Delta E}{\hbar\omega}}. \quad (5.4)$$

### 5.5. Temperature dependence of the decay rates

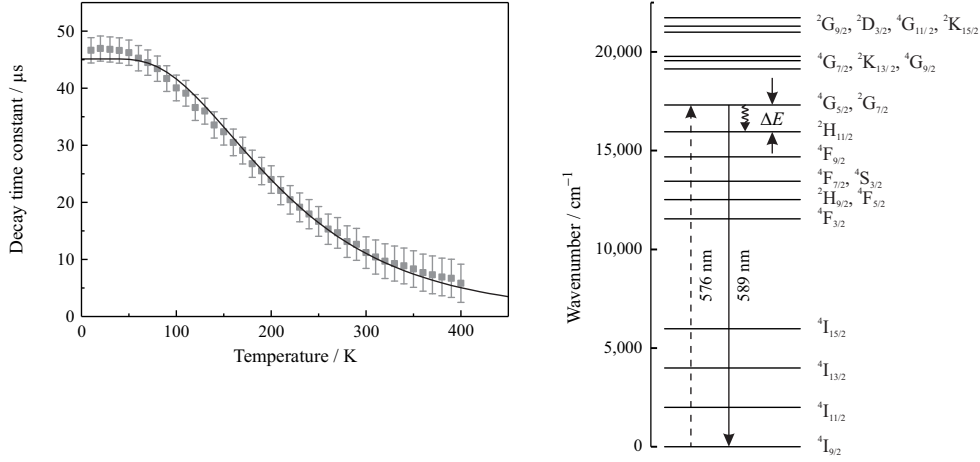


Figure 5.18.: Temperature dependence of the PL decay time constant of the ( ${}^4G_{5/2}$ ,  ${}^2G_{7/2}$ )  $\rightarrow$   ${}^4I_{9/2}$  transition at 589 nm of  $\text{Nd}^{3+}$  in the FCZ glass annealed at 260 °C following direct pulsed excitation. The sample is doped with 1 mol%  $\text{Nd}^{3+}$ . The solid curve shows the fit according to Equations 5.1 and 5.4. The wavy arrow in the energy level scheme indicates the MPR analyzed.

This equation enables the determination of (for a given energy gap  $\Delta E$ ) the energy  $\hbar\omega$  of the phonons involved in the MPR process. The temperature dependence of the measured lifetime was fitted with  $\tau_{\text{exp}}^{-1} = W_{\text{MPR}}(T) + \sum A$  (in accordance to Equation 5.1) by substituting  $W_{\text{MPR}}(T)$  with Equation 5.4. In contrast to the MPR rate  $W_{\text{MPR}}$ , the radiative decay rate does not depend on temperature. A least squares fitting procedure using the given values  $\Delta E = 1,361 \text{ cm}^{-1}$  and  $W_{\text{rad}} = 8,197 \text{ s}^{-1}$  yielded a spontaneous MPR rate of  $W_{\text{MPR},0} = 1.4 \cdot 10^4 \text{ s}^{-1}$  and a phonon energy of  $\hbar\omega = 260 \text{ cm}^{-1}$  (with an uncertainty of about 20 % for  $\hbar\omega$ ). The corresponding room temperature MPR rate is approximately  $8 \cdot 10^4 \text{ s}^{-1}$  which agrees well with the MPR rate obtained before for this level (see Table 5.5).



## 6. Experimental and theoretical investigations on vibrational spectra

The knowledge of the phonon spectra of the rare-earth host material is necessary for an interpretation of the determined MPR properties. Hence, the glasses and glass ceramics are studied here by Raman spectroscopy. Furthermore, the Raman investigations allow for conclusions concerning the structural properties. Besides different base glasses, the  $\text{BaCl}_2$  nanocrystals incorporated in the glasses are studied. There is also fundamental interest in the phonon spectra of the different occurring structural phases of  $\text{BaCl}_2$ . Besides Raman measurements, *ab initio* calculations of DFT are performed in order to investigate the phonon spectra of crystalline  $\text{BaCl}_2$  in hexagonal and orthorhombic symmetry. The calculations allow for a prediction of all phonon modes and for an assignment of the measured Raman modes to their symmetry types. Some parts of this chapter have already been published in Refs. [76, 53].

### 6.1. Raman spectra of the glasses and glass ceramics

Figure 6.1 gives an overview of the Raman spectra of the 1 mol%  $\text{Nd}^{3+}$ -doped FCZ sample series and of the 1 mol%  $\text{Nd}^{3+}$ -doped FZ glass. The as-made FCZ and FZ glasses show typical phonon spectra of FZ-based glasses consisting of several glass-related broad phonon bands between about  $200\text{ cm}^{-1}$  and  $580\text{ cm}^{-1}$ , which are analyzed at the end of this chapter. The spectra are normalized to the Raman band at approximately  $580\text{ cm}^{-1}$ .

Raman spectroscopy on the heat-treated FCZ glasses reveal that after annealing of the as-made sample, additional phonon modes appear below  $250\text{ cm}^{-1}$ . They can be related to the  $\text{BaCl}_2$  nanocrystal formation and are analyzed in the following sections.

All Raman spectra show a small background, which increases continuously with decreasing Raman shift. This background is zero above  $700\text{ cm}^{-1}$ . A weak emission tail of the  $(^2\text{G}_{9/2}, ^2\text{D}_{3/2}, ^4\text{G}_{11/2}, ^2\text{K}_{15/2}) \rightarrow ^4\text{I}_{9/2}$   $\text{Nd}^{3+}$  transition (centered at 482 nm), which is excited by the intense laser via upconversion processes [58], contributes to this background. In addition, the background is caused by Rayleigh scattering of the laser. This background is small due to the laser rejection in the Raman setup (see Section 3.1.1). Thus, the spectra can be analyzed without any background subtraction.

## 6. Experimental and theoretical investigations on vibrational spectra

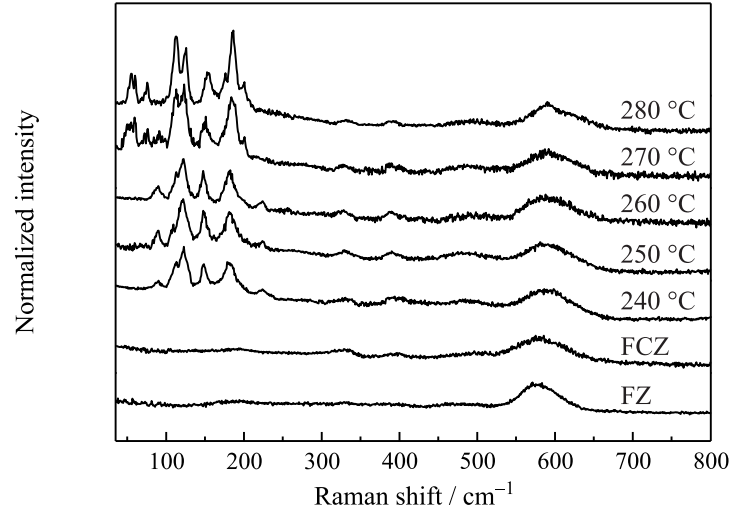


Figure 6.1.: Raman spectra of the 1 mol%  $\text{Nd}^{3+}$ -doped FZ-based glasses and glass ceramics. From bottom to top: as-made FZ; as-made FCZ; and FCZ annealed at 240, 250, 260, 270, and 280 °C. The spectra are normalized to the Raman band at approximately  $580 \text{ cm}^{-1}$  and vertically displaced for clarity.

### 6.2. Comparison of $\text{BaCl}_2$ nanocrystals and bulk $\text{BaCl}_2$

A comparison of the Raman spectra of bulk  $\text{BaCl}_2$  and of the above-mentioned  $\text{BaCl}_2$ -related phonon modes in Nd-doped FCZ glass is given in Figure 6.2. The annealing temperature used for the presented FCZ glass ceramic is 280 °C. Bulk  $\text{BaCl}_2$  has an orthorhombic  $Pnma$  crystal structure, which is the thermodynamically stable crystalline phase of  $\text{BaCl}_2$  [24]. In the given spectral range, the Raman spectrum of annealed FCZ glass is in good agreement with the bulk  $\text{BaCl}_2$  spectrum, showing that orthorhombic phase  $\text{BaCl}_2$  crystallites are formed upon annealing at 280 °C. The other FCZ glass ceramics, annealed at lower temperatures, show different  $\text{BaCl}_2$ -related phonon bands (see Figure 6.1), because another crystalline phase of  $\text{BaCl}_2$  or a mixture of different crystalline phases is formed depending on the annealing conditions. The different structural phases of the nanocrystals are analyzed in the following two sections.

The spectrum of the orthorhombic  $\text{BaCl}_2$  nanocrystals in the 280 °C sample (Figure 6.2, top) shows several Raman bands between about 50 and  $200 \text{ cm}^{-1}$ . The spectral positions of bulk  $\text{BaCl}_2$  (Figure 6.2, bottom) coincide well. The phonon energies and the mode assignments are given in Section 6.4. Because the nanocrystals are randomly orientated in the glasses, their Raman spectra are well averaged over all crystal orientations. This is not the case for the measurement of the polycrystalline bulk crystal in which only a few orientations are superimposed. Thus, only the spectral positions of the phonon modes, but not the intensities, should be compared. The signal-to-noise ratio of the Raman

## 6.2. Comparison of $\text{BaCl}_2$ nanocrystals and bulk $\text{BaCl}_2$

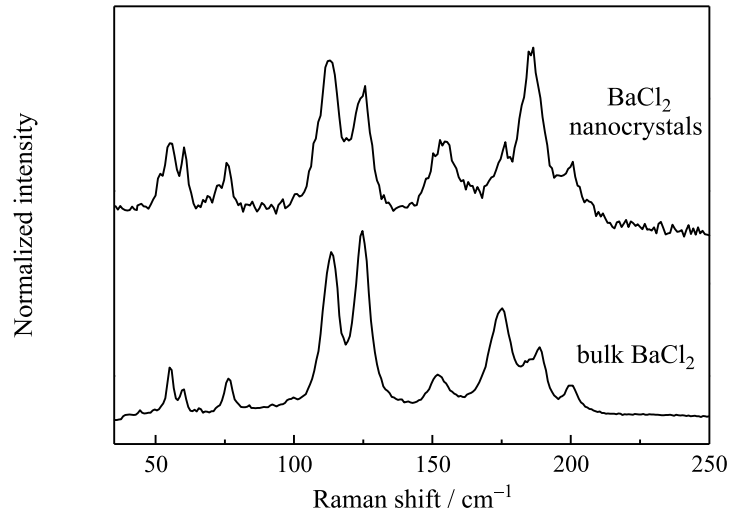


Figure 6.2.: Raman spectrum of orthorhombic  $\text{BaCl}_2$  nanocrystals in the 1 mol%  $\text{Nd}^{3+}$ -doped FCZ glass annealed at 280 °C (top) in comparison to Raman spectrum of bulk  $\text{BaCl}_2$  (bottom). The spectra are vertically displaced for clarity.

spectra of the nanocrystals is significantly lower than that found for the corresponding bulk  $\text{BaCl}_2$  spectrum. The reason for the lower signal-to-noise ratio in the glass ceramics is basically the lower  $\text{BaCl}_2$  content which is determined in Section 4.2 to be about 20 %. Compared to those of the bulk crystal, the lines are broadened in the Raman spectrum of the nanocrystals in the glass. This line broadening may originate from disorder and poor crystalline quality in the nanocrystals (see discussion in Section 8.1). Due to the random nanocrystal orientation the measured Raman spectra are a superposition of the spectra for all crystal directions. The phonon frequencies of bulk  $\text{BaCl}_2$  were analyzed previously by Sadoc and Guillo [42] using polarized Raman spectroscopy performed in different scattering geometries to obtain all six independent components of the polarizability tensor for orthorhombic symmetry. Their results are in good agreement with the experimental results obtained here for orthorhombic  $\text{BaCl}_2$ .

### 6.3. Calculated phonon spectra

For a deeper understanding of the phononic properties of the nanocrystals in the glasses, the Raman spectra of BaCl<sub>2</sub> in hexagonal and orthorhombic symmetry were calculated. First principles calculations were performed within the LDA to DFT as described in Section 3.1.2 and in the references given there. At the zone center, one expects 3 acoustical and 33 optical phonon modes in orthorhombic symmetry and 3 acoustical and 24 optical phonon modes in hexagonal symmetry. Factor group analysis predicts 18 ( $6A_g+3B_{1g}+6B_{2g}+3B_{3g}$ ) and 10 ( $2A'_1+6E'+2E''$ ) Raman-active modes for the orthorhombic  $Pnma$  and the hexagonal  $P\bar{6}2m$  structure, respectively. The calculated phonon energies of the Raman-active modes and the assignments to their symmetry adapted mode types are listed in Table 6.1 in the next section. The calculated Raman spectra of hexagonal and orthorhombic BaCl<sub>2</sub>, which are a superposition of the predicted Raman-active modes, are presented in Figure 6.3 and 6.4, respectively. For comparison the measured Raman spectra of the corresponding nanocrystals in the Nd-doped FCZ glasses annealed at 260 °C and 280 °C are shown in Figure 6.3 and 6.4, respectively. Orthorhombic BaCl<sub>2</sub> nanocrystals are formed in the 280 °C sample; the 260 °C sample represents a glass that contains hexagonal BaCl<sub>2</sub> nanocrystals (see XRD analysis in Section 4.2).

The contribution of each single Raman-active phonon mode to the resulting spectrum depends significantly on the orientation of the crystal with respect to the propagation direction and the polarization vectors of the incident and scattered light. For the present case of unpolarized Raman measurements of randomly orientated crystallites performed in reflection geometry, all Raman-active phonon modes contribute to the resulting spectrum, and their intensities are calculated in analogy to a powder spectrum (see Section 3.1.2). There is good agreement between the theoretical and experimental spectra; the deviation for the main bands with respect to the line positions is less than 5 % for both phases of BaCl<sub>2</sub>. In Ref. [48], we additionally found a good agreement between calculated and measured Raman spectra for BaBr<sub>2</sub>. The calculations were also compared to polarized Raman spectra on single BaCl<sub>2</sub> and BaBr<sub>2</sub> crystals performed in different scattering geometries. Such measurements allow for a detection and an identification of the single vibrational modes [42, 77]. The comparisons demonstrate that the approach used is appropriate to predict vibrational frequencies and relative intensities of the phonon modes in the corresponding crystals. Furthermore, the calculation method allows for an assignment of the vibrational modes to their symmetry types (see next section). For a variety of crystals, e.g., in a powder spectrum or nanocrystals in a matrix, no identification of the vibrational modes in the Raman spectrum is possible by experimental means.

In Ref. [48], it is shown that by theoretical mode prediction the measured modes can be assigned to their symmetry types, even for broader Raman peaks as they occur for nanocrystals.

### 6.3. Calculated phonon spectra

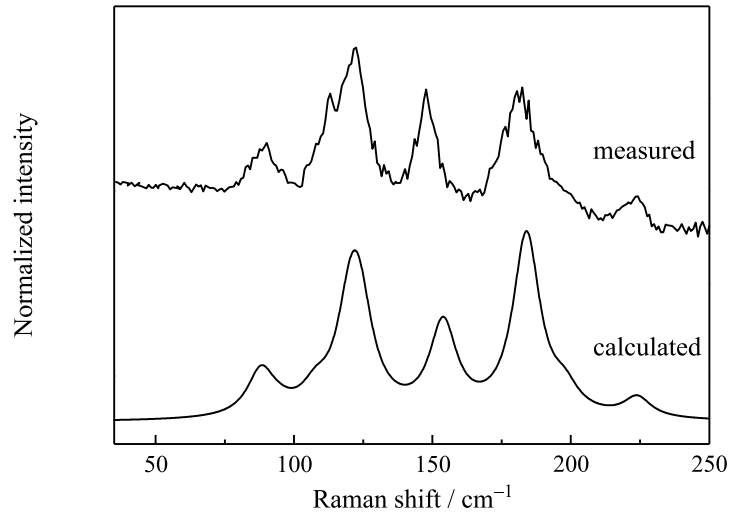


Figure 6.3.: Raman spectrum of hexagonal  $\text{BaCl}_2$  nanocrystals in the 1 mol%  $\text{Nd}^{3+}$ -doped FCZ glass annealed at 260 °C (top) in comparison to calculated Raman spectrum of hexagonal  $\text{BaCl}_2$  obtained from DFT (bottom). The spectra are vertically displaced for clarity.

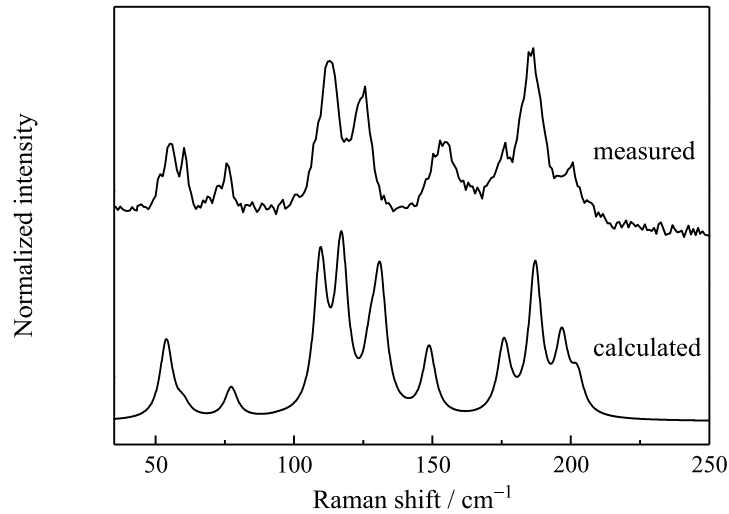


Figure 6.4.: Raman spectrum of orthorhombic  $\text{BaCl}_2$  nanocrystals in the 1 mol%  $\text{Nd}^{3+}$ -doped FCZ glass annealed at 280 °C (top) in comparison to calculated Raman spectrum of orthorhombic  $\text{BaCl}_2$  obtained from DFT (bottom). The spectra are vertically displaced for clarity.

Not all the single Raman modes are resolved in the Raman spectra due to the finite linewidth and spectral overlap of the modes. As mentioned in Section 3.1.2, it is necessary to define a spectral linewidth and line shape for the Raman modes in order to calculate spectra from the Raman scattering intensities. Lorentzian line shapes are assumed for the Raman bands. Using a linewidth

## 6. Experimental and theoretical investigations on vibrational spectra

of  $5.5 \text{ cm}^{-1}$  (FWHM used in Figure 6.4) for orthorhombic  $\text{BaCl}_2$  provides the best qualitative agreement with the measured spectrum of the orthorhombic  $\text{BaCl}_2$  nanocrystals. The hexagonal  $\text{BaCl}_2$  nanocrystals exhibit larger Raman linewidths; the best agreement with the measurement is achieved with a linewidth of  $12.0 \text{ cm}^{-1}$  (FWHM used in Figure 6.3). The larger linewidths of the Raman bands of the hexagonal nanocrystals is discussed in Section 8.1.

### 6.4. Mode assignment and structural phase transitions

Table 6.1 lists the calculated energies of the Raman-active phonon modes together with the assignments to their symmetry adapted mode types for  $\text{BaCl}_2$  in hexagonal and orthorhombic symmetry. For comparison the assigned measured peak energies of the Raman bands in the corresponding nanocrystals are also given in Table 6.1. The assignment of the measured Raman bands to the predicted phonon modes is done on the basis of their spectral positions and their relative intensities. A clear assignment is possible if the measured spectra are compared to theoretical spectra, which are calculated for a small spectral linewidth. The spectra obtained for a small FWHM of  $2 \text{ cm}^{-1}$  are shown in Ref. [48]; they were calculated for the present scattering geometry in analogy to the spectra in Section 6.3. The Raman spectra are superpositions of all the Raman-active phonon modes, but only some modes contribute significantly to the resulting spectra due to their strong relative intensities. The spectrum of orthorhombic  $\text{BaCl}_2$  nanocrystals in the  $280 \text{ }^\circ\text{C}$  sample consists of six Raman bands at approximately  $55, 76, 113, 125, 152,$  and  $186 \text{ cm}^{-1}$  and three shoulders at  $60, 175,$  and  $200 \text{ cm}^{-1}$ . The spectrum of hexagonal  $\text{BaCl}_2$  in the  $260 \text{ }^\circ\text{C}$  sample shows five Raman bands positioned at  $90, 123, 148, 182,$  and  $224 \text{ cm}^{-1}$  and a shoulder at  $113 \text{ cm}^{-1}$ . The main bands of orthorhombic crystallites are basically caused by the highest energy  $\text{B}_{3g}$  mode and the six  $\text{A}_g$  modes, whereas the lowest energy  $\text{B}_{2g}$  mode is superimposed on its neighboring  $\text{A}_g$  mode. Also one  $\text{B}_{1g}$  and another  $\text{B}_{2g}$  mode contribute significantly to the spectra causing the shoulders at about  $60 \text{ cm}^{-1}$  and the band at about  $152 \text{ cm}^{-1}$ , respectively. The Raman features of hexagonal  $\text{BaCl}_2$  nanocrystals originate from three  $\text{E}'$  modes, both  $\text{A}'_1$  modes and both  $\text{E}''$  modes, whereas the lowest energy  $\text{A}'_1$  mode and lower  $\text{E}''$  mode are superimposed on each other.

Figure 6.5 shows the  $\text{BaCl}_2$ -related Raman spectra of the FCZ ceramics in comparison to the calculated phonon energies for  $\text{BaCl}_2$  in hexagonal and orthorhombic symmetry. The  $\text{BaCl}_2$  Raman modes, which appear after annealing of the as-made glass, differ for the different annealing steps. The stick diagrams in Figure 6.5, which show the calculated spectral positions, facilitate a phase identification of the  $\text{BaCl}_2$  nanocrystals in the differently heat-treated FCZ glasses. In addition, the stick diagrams illustrate well how the single Raman-active phonon modes contribute to the experimental spectra. The  $240 \text{ }^\circ\text{C}$  sam-

#### 6.4. Mode assignment and structural phase transitions

Table 6.1.: Theoretically predicted energetic positions (values in  $\text{cm}^{-1}$ ) of the Raman-active zone center phonon modes and assignment to their symmetry adapted mode types in hexagonal ( $P\bar{6}2m$  structure) and orthorhombic ( $Pnma$  structure)  $\text{BaCl}_2$ . The peak positions of measured Raman bands of the hexagonal and orthorhombic  $\text{BaCl}_2$  nanocrystals in FCZ glass annealed at 260 °C and 280 °C are given for comparison, respectively.

$P\bar{6}2m$			$Pnma$		
predicted	observed	mode	predicted	observed	mode
88	90	$E'$	54	55	$A_g$
95	-	$E'$	54		$B_{3g}$
108	113	$E'$	60	60	$B_{1g}$
120	123	$E''$	77	76	$A_g$
124	123	$A'_1$	95	-	$B_{2g}$
132	-	$E'$	110	113	$A_g$
154	148	$E''$	117	-	$B_{1g}$
184	182	$E'$	117	113	$B_{2g}$
198	-	$E'$	127	-	$B_{2g}$
224	224	$A'_1$	127	-	$B_{3g}$
			131	125	$A_g$
			149	152	$B_{2g}$
			170	-	$B_{2g}$
			176	175	$A_g$
			187	-	$B_{1g}$
			187	186	$B_{3g}$
			197	200	$A_g$
			202	-	$B_{2g}$

ple and the 250 °C sample exhibit the same  $\text{BaCl}_2$ -related Raman bands like the 260 °C sample. In analogy to the 260 °C sample, their Raman bands can be assigned to hexagonal  $\text{BaCl}_2$ . After the 270 °C annealing step, a mixture of two different phonon spectra is found: Besides the phonon modes already observed for orthorhombic  $\text{BaCl}_2$  in the 280 °C sample, the sample shows additional phonon modes, which are also found in the spectrum of the hexagonal  $\text{BaCl}_2$  in the glasses annealed between 240 °C and 260 °C. In the 270 °C sample, the phonon bands of orthorhombic  $\text{BaCl}_2$  are not completely developed, for example the shoulder at about  $175 \text{ cm}^{-1}$  ( $A_g$  mode in orthorhombic  $\text{BaCl}_2$ ) is difficult to observe. Some phonon modes of hexagonal  $\text{BaCl}_2$  have not completely disappeared. In particular, the hexagonal  $\text{BaCl}_2$   $E'$  and  $E''$  modes at about  $90 \text{ cm}^{-1}$  and  $150 \text{ cm}^{-1}$ , respectively, are still observable after annealing at 270 °C. These results confirm the findings from the XRD analysis, in which the same phases are identified: Hexagonal  $\text{BaCl}_2$  is found in the 240 - 260 °C

## 6. Experimental and theoretical investigations on vibrational spectra

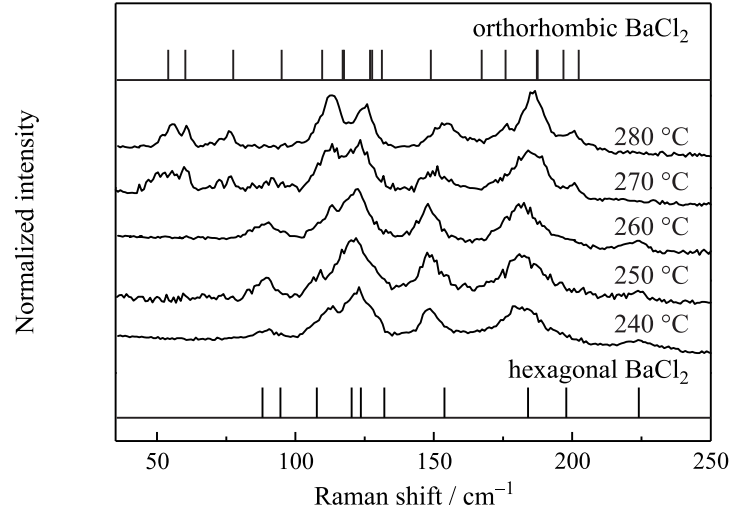


Figure 6.5.: Raman spectra of BaCl<sub>2</sub> nanocrystals in the 1 mol% Nd<sup>3+</sup>-doped FCZ glasses. From bottom to top: FCZ annealed at 240, 250, 260, 270, and 280 °C. The stick diagrams show the calculated spectral positions of the Raman-active phonon modes of hexagonal and of orthorhombic BaCl<sub>2</sub>. The spectra are vertically displaced for clarity.

samples, orthorhombic BaCl<sub>2</sub> is found in the 280 °C sample, and a mixture of both phases is found in the 270 °C sample.

### 6.5. Consideration of all optical phonon modes

The applied calculation method is also capable of predicting IR-active phonon modes. For a comprehensive consideration of the phonon spectra, Raman-active and IR-active phonon modes should be investigated. Only then is it possible to determine the highest energy phonon modes of the corresponding crystalline phases of BaCl<sub>2</sub> being important for the MPR properties of the material.

The calculated spectral positions of all optical phonon modes can be found in Figure 6.6 and Figure 6.7 for hexagonal and orthorhombic BaCl<sub>2</sub>, respectively. The Raman spectra of the corresponding crystalline phases are shown for comparison. Measurements of the IR spectra are challenging since the measurement apparatus must be capable of far IR spectral range, and a special sample preparation is required to enable appropriate light passing in this spectral range. The experimental efforts necessary to obtain the IR spectra of the hygroscopic BaCl<sub>2</sub> are beyond the scope of this work. Here, the issue is considered from the theoretical side. The DFT calculations, which have proven to be in agreement with the measurements (see Section 6.3), allow for a sufficiently precise estimation of the phonon cut-off frequencies, which are of particular interest for this work.

As stated above, orthorhombic BaCl<sub>2</sub> has 36 phonon modes ( $p = 12$  atoms and  $3p$  degrees of freedom per unit cell), i.e. 33 optical and 3 acoustical phonon

### 6.5. Consideration of all optical phonon modes

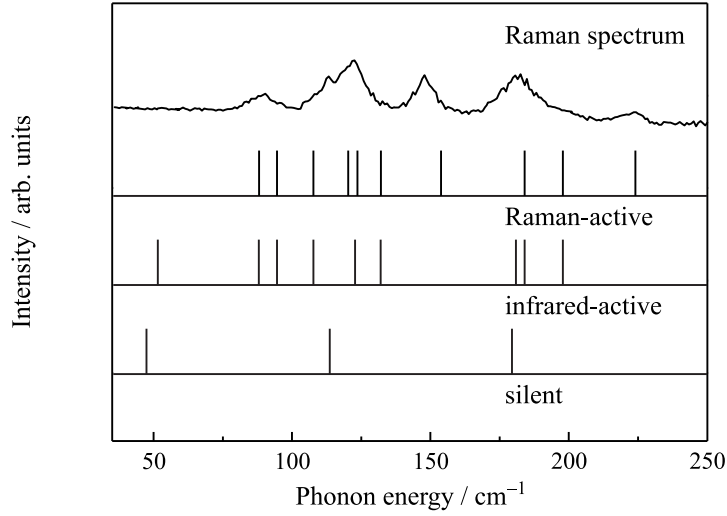


Figure 6.6.: Calculated spectral positions of the Raman-active (top), IR-active (middle) and silent (bottom) phonon modes of hexagonal  $\text{BaCl}_2$  obtained from DFT. For comparison the measured Raman spectrum of hexagonal  $\text{BaCl}_2$  nanocrystals in the 1 mol%  $\text{Nd}^{3+}$ -doped FCZ glass annealed at 260 °C is shown.

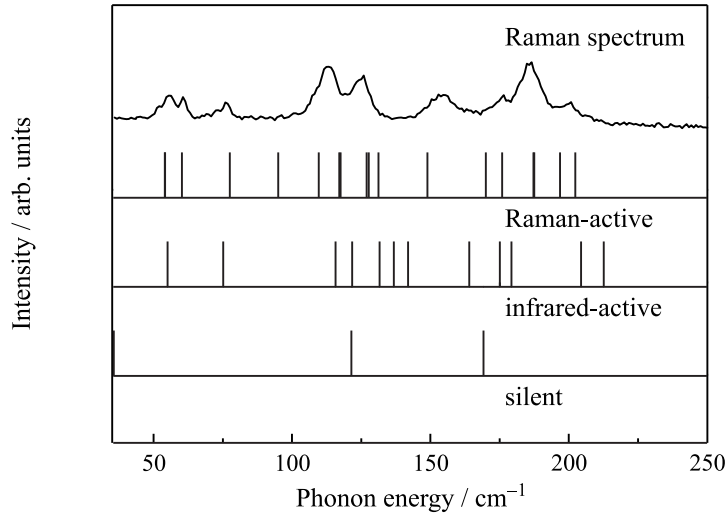


Figure 6.7.: Calculated spectral positions of the Raman-active (top), IR-active (middle) and silent (bottom) phonon modes of orthorhombic crystalline  $\text{BaCl}_2$  obtained from DFT. For comparison the measured Raman spectrum of orthorhombic  $\text{BaCl}_2$  nanocrystals in the 1 mol%  $\text{Nd}^{3+}$ -doped FCZ glass annealed at 280 °C is shown.

modes. The 33 optical phonon modes consists of 18 ( $6A_g+3B_{1g}+6B_{2g}+3B_{3g}$ ) Raman-active, 12 ( $5B_{1u}+2B_{2u}+5B_{3u}$ ) IR-active, and 3 ( $3A_u$ ) silent phonon modes [48]. Silent phonon modes are neither Raman-active nor IR-active. Hexagonal  $\text{BaCl}_2$  provides 27 phonon modes ( $p = 9$  atoms and  $3p$  degrees of freedom per unit cell), i.e. 24 optical and 3 acoustical phonon modes. Factor

## 6. Experimental and theoretical investigations on vibrational spectra

Table 6.2.: Theoretically predicted spectral positions of the IR-active and silent zone center phonon modes and assignment to their symmetry adapted mode types in hexagonal ( $P\bar{6}2m$  structure) and orthorhombic ( $Pnma$  structure)  $\text{BaCl}_2$ .

$P\bar{6}2m$			$Pnma$		
$\hbar\omega$ ( $\text{cm}^{-1}$ )	mode	activity	$\hbar\omega$ ( $\text{cm}^{-1}$ )	mode	activity
47	$A_1''$	silent	36	$A_u$	silent
52	$A_2''$	IR	55	$B_{1u}$	IR
88	$E'$	IR	75	$B_{3u}$	IR
95	$E'$	IR	116	$B_{1u}$	IR
108	$E'$	IR	121	$A_u$	silent
114	$A_1''$	silent	122	$B_{2u}$	IR
123	$A_2''$	IR	132	$B_{3u}$	IR
132	$E'$	IR	137	$B_{3u}$	IR
179	$A_2'$	silent	142	$B_{1u}$	IR
181	$A_2''$	IR	164	$B_{3u}$	IR
184	$E'$	IR	169	$A_u$	silent
198	$E'$	IR	175	$B_{2u}$	IR
			179	$B_{1u}$	IR
			204	$B_{1u}$	IR
			213	$B_{3u}$	IR

group analysis predicts 10 ( $2A_1'+6E'+2E''$ ) Raman-active, 9 ( $3A_2''+6E'$ ) IR-active, and 3 ( $2A_2'+1A_1''$ ) silent phonon modes [48]. The  $E'$  modes are both Raman- and IR-active. In orthorhombic  $\text{BaCl}_2$ , to the contrary, the mutual exclusion principle, which forbids that vibrational modes are both Raman- and IR-active, is valid, because the orthorhombic  $Pnma$  structure has an inversion center of symmetry. The  $E'$  and  $E''$  modes are twofold degenerated; the total number of optical phonon modes in hexagonal  $\text{BaCl}_2$  is thus 24 ( $2A_1'+2\cdot 6E'+2\cdot 2E''+3A_2''+2A_2'+1A_1''$ ). For completeness, the calculated energies of the IR and silent phonon modes and the assignments to their symmetry adapted types are listed in Table 6.2. As shown in Figures 6.6 and 6.7, the highest energy phonon mode is Raman-active in hexagonal  $\text{BaCl}_2$  and IR-active in orthorhombic  $\text{BaCl}_2$ .

## 6.6. Analysis of the glass-related Raman bands

Figure 6.8 compares the glass-related phonon bands of the as-made FZ glass, of the as-made FCZ glass, and of a FCZ glass ceramic heat-treated at 260 °C. The 260 °C glass ceramic is representative of all annealed samples; the other glass ceramics display similar glass-related Raman modes. The measured peak positions of glass-related phonon bands and their assignments to vibrations in FZ-based glasses are given in Table 6.3. Five Raman bands are observed; they peak at about 580, 490, 390, 330, and 200  $\text{cm}^{-1}$ . The Raman band at about 200  $\text{cm}^{-1}$  is not observable in the glass ceramic, because it is superimposed by the  $\text{BaCl}_2$ -related phonon modes below 250  $\text{cm}^{-1}$ .

The strong band at approximately 580  $\text{cm}^{-1}$ , which is found in the Raman spectra of all samples, can be assigned to symmetric stretching vibrations of nonbridging Zr-F bonds in FZ-based glasses [17]. Almeida's and Mackenzie's [78] study of the structure of binary FZ-based glasses, in which IR and Raman spectra are investigated, shows that this vibration is caused by the highest energy phonons in these glasses. In Ref. [78], a glass structure which basically consists of zig-zag chains of  $\text{ZrF}_6$  octahedra, cross-linked by other metal-fluoride bonds is proposed. The  $\text{ZrF}_6$  octahedra have four nonbridging fluorine atoms and two bridging fluorine atoms. The vibrational mode originates from symmetric stretching of these four nonbridging Zr-F bonds in a square planar structure. In other studies, slightly higher coordination numbers of seven to eight are proposed [18]; however, there is a general agreement on the basic structure described in Ref. [78]. The phonon band at about 480  $\text{cm}^{-1}$  is related to symmetric stretching vibrations of the two bridging fluorine atoms in the  $\text{ZrF}_6$  octahedra [78]. The next two Raman bands are assigned to vibrations in isolated  $\text{ZrF}_6^{-2}$  octahedra [78], they are located at about 390  $\text{cm}^{-1}$  and 330  $\text{cm}^{-1}$ . The first one belongs to antisymmetric Zr-F stretching modes. The latter one is caused by F-Zr-F bending modes in the free  $\text{ZrF}_6^{-2}$  octahedra. The last observed Raman band at about 200  $\text{cm}^{-1}$  originates from Zr-F-Zr bending in the zig-zag chains of  $\text{ZrF}_6$  octahedra [79].

The Raman spectra and the peak positions of the phonon bands of as-made FZ and FCZ do not show a significant difference, which indicates a similar behavior as described by Almeida and Mackenzie in Ref. [80]. They compared  $\text{ZrF}_4\text{BaF}_2$  and  $\text{ZrF}_4\text{BaCl}_2$  model glasses and observed similar Raman spectra for the FZ and FCZ glasses. This indicates that the chlorine does not influence the basic structure consisting of zig-zag chains of six-coordinated octahedra. Since the highest energy vibration does not differ between FZ and FCZ glass, they suggested that the square planar structure of the four bridging fluorine atoms around the Zr atoms is unaffected, and the Cl atoms basically occupy the bridging positions in the chain of the six-coordinated octahedra [80].

The Raman spectrum of the FCZ glass ceramic differs significantly from those of the as-made FZ and FCZ glasses. Apart from the additional phonon modes

## 6. Experimental and theoretical investigations on vibrational spectra

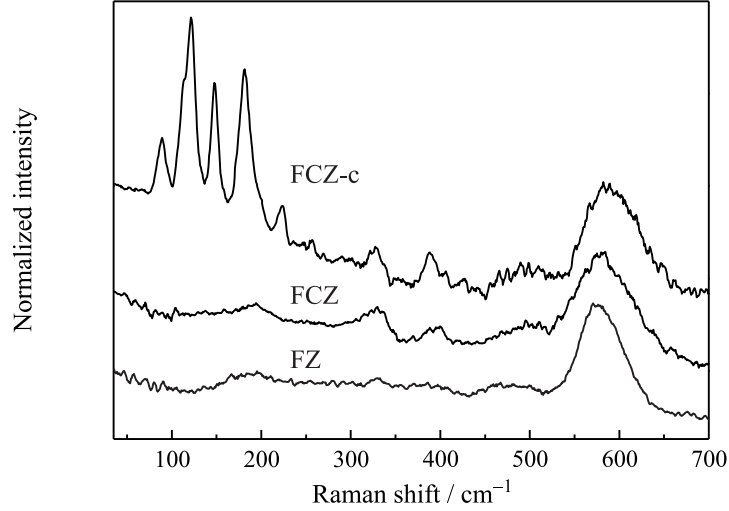


Figure 6.8.: Raman spectra of the 1 mol%  $\text{Nd}^{3+}$ -doped FZ-based glasses and glass ceramics in the frequency range of the glass-related Raman bands. From bottom to top: as-made FZ, as-made FCZ, and FCZ annealed at 260 °C (FCZ-c). The spectra are normalized to the Raman band at approximately 580  $\text{cm}^{-1}$  and vertically displaced for clarity.

Table 6.3.: Observed peak energies (values in  $\text{cm}^{-1}$ ) of the glass-related Raman bands in as-made FZ, in as-made FCZ, and in FCZ annealed at 260 °C (FCZ-c) and vibrational mode assignment for FZ-based glass.

FZ	FCZ	FCZ-c	assignment	Ref.
$576 \pm 3$	$580 \pm 3$	$589 \pm 4$	symm. stretching of nonbridging Zr-F bonds	[17]
$479 \pm 7$	$493 \pm 8$	$493 \pm 8$	symm. stretching of bridging Zr-F bonds	[78]
$390 \pm 5$	$395 \pm 4$	$390 \pm 4$	antisymm. Zr-F stretching in free $\text{ZrF}_6^{-2}$	[78]
$331 \pm 3$	$331 \pm 3$	$329 \pm 3$	F-Zr-F in free $\text{ZrF}_6^{-2}$	[78]
$195 \pm 8$	$195 \pm 6$	-	in-chain bending of Zr-F-Zr bridges	[79]

which are related to the  $\text{BaCl}_2$  nanocrystals, the highest energy vibration in the base glass is significantly shifted by more than 10  $\text{cm}^{-1}$  (see Table 6.3). This shift towards higher energies indicates a decreasing halide-to-zirconium ratio in the base glass. Aasland *et al.* [17] found that the energy of this symmetric stretching vibration basically depends on the fluorine-to-zirconium ratio in the glass composition, which is related to structural changes involving a changing Zr coordination number. The batch composition of the FZ glass has a fluorine-to-zirconium ratio of 5.6; the FCZ glass has the same halide-to-zirconium ratio but some fluorine is substituted by chlorine. For such ratios, maximum phonon energies of about 570  $\text{cm}^{-1}$  are reported [17]. The observed maximum phonon energy of the as-made FZ and FCZ glasses is slightly higher (576  $\text{cm}^{-1}$  and 580  $\text{cm}^{-1}$ , respectively) which indicates little evaporation loss during the melt-

## 6.7. Influence of rare-earth ions on the phonon spectra

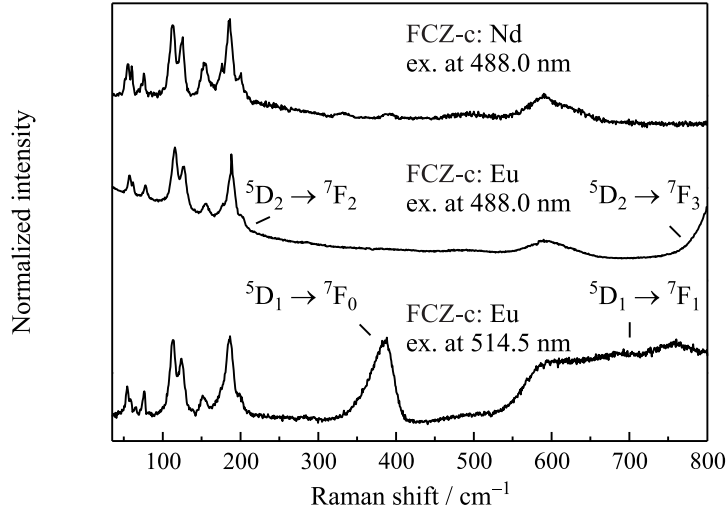


Figure 6.9.: Comparison of Raman spectra of Nd-doped and Eu-doped FCZ glass ceramics with orthorhombic  $\text{BaCl}_2$  nanocrystals: 1 mol%  $\text{Nd}^{3+}$ -doped FCZ annealed at 280 °C (FCZ-c: Nd) (top) and the 5 mol%  $\text{Eu}^{2+}$ -doped FCZ annealed at 290 °C (FCZ-c: Eu) (middle and bottom). The used excitation wavelengths are 488.0 nm (top and middle) and 514.5 nm (bottom). The corresponding optical transitions of the superimposing  $\text{Eu}^{3+}$  emissions are indicated. The spectra are vertically displaced for clarity.

ing process. The energy shift to  $590 \text{ cm}^{-1}$  in the FCZ glass ceramic can be attributed to a loss of halides in the glass matrix due to the formation of the  $\text{BaCl}_2$  nanocrystals induced by the annealing process. For maximum phonon energies of  $590 \text{ cm}^{-1}$  correspond to halide-to-zirconium ratios of 4.8 [17].

## 6.7. Influence of rare-earth ions on the phonon spectra

All Raman spectra presented in the previous sections are measurements of neodymium-doped FCZ glasses and glass ceramics since the main focus of this work is on these samples. Raman spectra of europium-doped samples with a similar FCZ base glass composition are presented in Ref. [53]. The comparison of the differently doped glass ceramics in Figure 6.9 does not show a significant difference of the Raman bands (for details see Pfau *et al.* [53]). Furthermore, measurements on rare-earth-free FCZ glass ceramics provide similar Raman spectra. This indicates that the phonon spectra are not influenced by the rare-earth doping. It can be concluded that the structure of the base glass and of the  $\text{BaCl}_2$  nanocrystals is not significantly changed by the rare-earth ions. This is, of course, related to the low rare-earth concentration in the samples (rare-earth doping level of a few mol%).

It should be noted that the specific PL emissions of the rare-earth ions can be

## 6. *Experimental and theoretical investigations on vibrational spectra*

superimposed on the Raman spectra. For example, upon excitation at 488.0 nm  $\text{Eu}^{3+}$ -emissions centered at 510 nm ( ${}^5\text{D}_2$ - ${}^7\text{F}_3$  transition, the corresponding Raman shift is about  $880\text{ cm}^{-1}$ ) and 488 nm ( ${}^5\text{D}_2$ - ${}^7\text{F}_2$  transition) are observed in the Raman spectra of the Eu-doped samples. The tail of the latter is superimposed on the  $\text{BaCl}_2$ -related phonon modes. Thus, an excitation wavelength of 488.0 nm is not suitable for studying  $\text{BaCl}_2$  phonon spectra in case of Eu-doping. When Raman scattering is excited at 514.5 nm, the Raman spectra are superimposed by  $\text{Eu}^{3+}$ -emissions centered at 525 nm ( ${}^5\text{D}_1$ - ${}^7\text{F}_0$  transition, the corresponding Raman shift is about  $390\text{ cm}^{-1}$ ) and 535 nm ( ${}^5\text{D}_1$ - ${}^7\text{F}_1$  transition, the corresponding Raman shift is about  $750\text{ cm}^{-1}$ ) making investigations on several glass-related phonon bands impossible. Figure 6.9 shows Raman spectra of the Eu-doped FCZ ceramic for both excitation wavelengths. The observed optical transitions of  $\text{Eu}^{3+}$  are indicated. These superimposing bands are not related to the phonons or Raman scattering; they are solely related to the rare-earth PL in the VIS spectral range, which is excited by the Raman laser. Thus, the excitation wavelength must be chosen for the present rare-earth ion in such a way that superimposing on the investigated phonon bands is avoided.

## 7. Investigation of the oxidation state of rare-earth ions: a Mössbauer study

Another important issue for the development of rare-earth doped glass ceramics is the oxidation state of the rare-earth ions. Whereas, most rare-earth ions occur in a trivalent valence state in solid hosts, europium shows both the trivalent and the divalent ionization state. For the usage of Eu-doped FZ-based glass ceramics as storage phosphors or scintillators, the  $\text{Eu}^{2+}/\text{Eu}^{3+}$  ratio is important, which can be determined by Mössbauer spectroscopy in principle. It is investigated under which conditions the  $\text{Eu}^{2+}$ -to- $\text{Eu}^{3+}$  ratio can be estimated by this method. Using low temperature Mössbauer spectroscopy, routes for maximizing the divalent europium content are investigated by varying chemical compositions and preparation parameters. This chapter has already been published in Ref. [81].

### 7.1. Optimization of Eu-doped glasses and glass ceramics

In the framework of the Mössbauer study a glass of the composition  $51\text{ZrF}_4-17\text{BaCl}_2-20\text{NaF}-3.5\text{LaF}_3-3\text{AlF}_3-0.5\text{InF}_3-5\text{EuF}_2$ , is compared to a glass of the composition  $51\text{ZrF}_4-17\text{BaCl}_2-20\text{NaF}-3.5\text{LaF}_3-3\text{AlF}_3-0.5\text{InF}_3-5\text{EuCl}_2$ , i.e. in the latter one  $\text{EuCl}_2$  is used instead of  $\text{EuF}_2$  (values given in mol%). The  $\text{EuF}_2$ -doped FCZ glass is henceforth abbreviated with FCZ – 5 mol%  $\text{EuF}_2$ , while the acronym for the  $\text{EuCl}_2$ -doped sample is FCZ – 5 mol%  $\text{EuCl}_2$ . The preparation procedure is comparable to that described in Section 4.1. More details can be found in Ref. [81]. Subsequently, the glasses are annealed for 5 minutes at  $300\text{ }^\circ\text{C}$  to initiate the growth of  $\text{BaCl}_2$  therein. Each sample is powdered and uniformly distributed on the sample holder area ( $60\text{ mg/cm}^2$ ) in an inert argon atmosphere, before being quickly put into the cryostat to avoid oxidation.

In Figure 7.1 the 260 K and 6 K Mössbauer spectra of an as-made  $\text{EuCl}_2$ -doped FCZ glass are compared. The corresponding fitting parameters of the  $\text{Eu}^{2+}$  Mössbauer line are given in Table 7.1. The  $\text{Eu}^{2+}$  and  $\text{Eu}^{3+}$  Mössbauer lines have shifts (isomer plus second order Doppler) of about  $-14\text{ mm/s}$  and  $0\text{ mm/s}$ , respectively. According to theory, the absolute value of the second order Doppler shift increases as the temperature is lowered. The expected effect of the temperature on the shift is about  $-10^{-4}\text{ mm/(s}\cdot\text{K)}$  [82], and is within the

7. Investigation of the oxidation state of rare-earth ions: a Mössbauer study

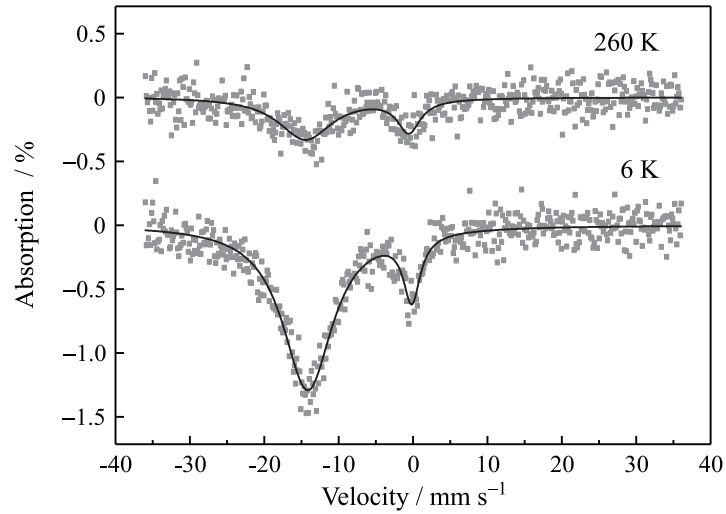


Figure 7.1.: Mössbauer spectra of an as-made 5 mol%  $\text{EuCl}_2$ -doped FCZ glass measured at 260 K (top) and 6 K (bottom).

Table 7.1.: Fitting parameters of the  $\text{Eu}^{2+}$  Mössbauer spectra in different FCZ glasses, measured at 6 K, the values at 260 K are given in brackets.

sample composition	treatment	area fraction (%)	line shift (mm/s)	line width (mm/s)
FCZ – 5 mol% $\text{EuF}_2$	as-made	$69.6 \pm 4.6$	$-14.3 \pm 0.2$	$8.9 \pm 0.5$
FCZ – 5 mol% $\text{EuCl}_2$	as-made	$88.0 \pm 1.8$ ( $75.4 \pm 8.5$ )	$-14.0 \pm 0.1$ ( $-14.3 \pm 0.3$ )	$8.3 \pm 0.2$ ( $8.9 \pm 0.9$ )
FCZ – 5 mol% $\text{EuCl}_2$	annealed at 300 °C in air	$84.2 \pm 3.6$	$-14.0 \pm 0.1$	$7.0 \pm 0.3$
FCZ – 5 mol% $\text{EuCl}_2$	annealed at 300 °C in Ar	$89.4 \pm 3.7$ ( $77.8 \pm 9.8$ )	$-14.1 \pm 0.1$ ( $-14.1 \pm 0.2$ )	$7.3 \pm 0.3$ ( $7.5 \pm 0.5$ )

experimental error (see Table 7.1) and can thus not be observed.

The linewidth of the  $\text{Eu}^{2+}$  resonance (about 8-9 mm/s) is broad mainly because of paramagnetic relaxation and partly because of the different sites associated with the disorder in the glass. This may be compared with that of the  $\text{Eu}^{3+}$  (about 3 mm/s), which has a non-magnetic ground state. The measurements do not show a significant influence of the temperature on the linewidths.

The Mössbauer effect increases as the temperature is decreased. The enhanced absorption at low temperature is clearly visible in Figure 7.1. Besides this, low temperature Mössbauer spectroscopy has the further advantages that it prevents the sample from oxidizing. Without a cryostat the powdered samples oxidized very quickly. A partial break-through to obtain spectra from  $\text{Eu}^{2+}$  in the glasses was making polished plates as used in [83], which oxidized more

### 7.1. Optimization of Eu-doped glasses and glass ceramics

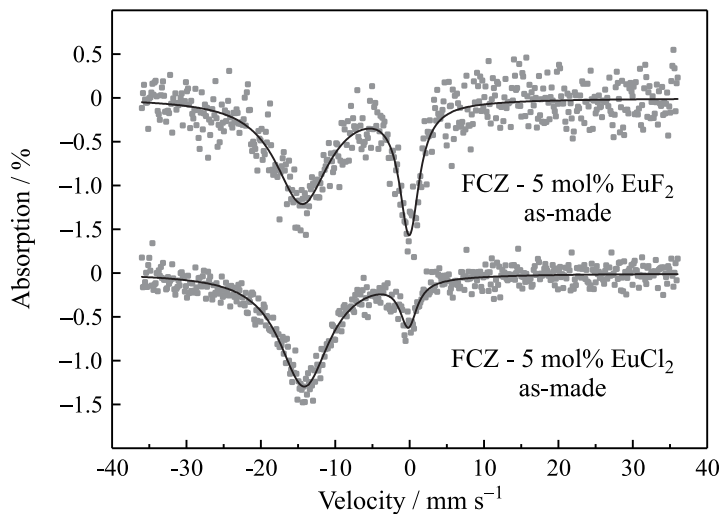


Figure 7.2.: Mössbauer spectra of as-made 5 mol%  $\text{EuF}_2$ -doped (top) and 5 mol%  $\text{EuCl}_2$ -doped (bottom) FCZ glasses, both measured at 6 K.

slowly. The measurements presented here are done on powdered samples installed in a closed-cycle cryostat in which both the low temperature and the vacuum prevented oxidation.

The main reason for going to low temperatures is to achieve a good quantitative analysis of the  $\text{Eu}^{2+}$ -to- $\text{Eu}^{3+}$  ratio. The ratio of the areas under the  $\text{Eu}^{2+}$  and  $\text{Eu}^{3+}$  absorption lines is 70 : 30 and 88 : 12 at 260 K and at 6 K, respectively. The  $\text{Eu}^{2+}$ -to- $\text{Eu}^{3+}$  ratio increases on cooling, because the Mössbauer effect increases more for  $\text{Eu}^{2+}$  than for  $\text{Eu}^{3+}$  resulting from its weaker binding strength (see below). The relative area of each line does not give directly the amount of each oxidation state present. The low temperature values of the  $f$ -factors are limited by the mean square zero-point vibrations. The ratio measured at the lowest temperature would be the closest to the true value. An analysis of the  $f$ -factors shows that the estimated relative area at 6 K is already a very good estimate for the real value (see below).

In Figure 7.2 low temperature Mössbauer spectra of the as-made FCZ – 5 mol%  $\text{EuF}_2$  and FCZ – 5 mol%  $\text{EuCl}_2$  samples are compared (for the fitting parameters see Table 7.1). The isomer shift depends on the glass composition; the fit of the  $\text{Eu}^{2+}$  Mössbauer line gives  $-14.0$  mm/s for  $\text{EuF}_2$ -doping and  $-14.3$  mm/s for  $\text{EuCl}_2$ -doping. The difference between F and Cl is barely significant, but it shows the expected tendency. Mössbauer studies of different  $\text{Eu(II)}$ -halides [82] suggest that the absolute value of the isomer shift increases as the covalency increases, i.e. in the order  $\text{F} < \text{Cl}$ . There is only a small difference between the linewidths of the FCZ – 5 mol%  $\text{EuCl}_2$  and FCZ – 5 mol%  $\text{EuF}_2$  samples.

The relative absorption strengths are strongly affected by the europium halide used for doping. An analysis of the relative areas under the absorption lines

## 7. Investigation of the oxidation state of rare-earth ions: a Mössbauer study

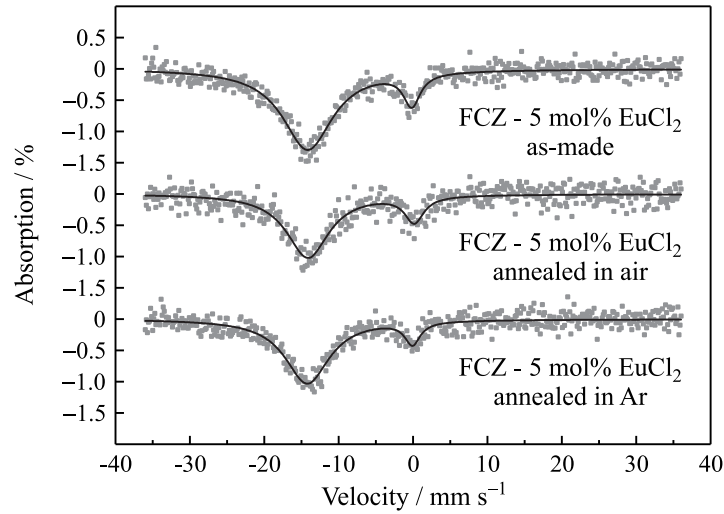


Figure 7.3.: Mössbauer spectra of as-made (top), annealed at 300 °C in air (middle), and in an argon atmosphere (bottom) 5 mol%  $\text{EuCl}_2$ -doped FCZ glasses. All spectra were measured at 6 K.

yields that using  $\text{EuCl}_2$  instead of  $\text{EuF}_2$  significantly improves the  $\text{Eu}^{2+}$ -to- $\text{Eu}^{3+}$  ratio. A replacement of  $\text{EuF}_2$  by  $\text{EuCl}_2$  increases the relative  $\text{Eu}^{2+}$  area from 70 % to 88 %.  $\text{EuCl}_2$  is preferable for keeping the  $\text{Eu}^{2+}$  fraction high having a lower free energy in an FCZ glass than  $\text{EuF}_2$ . This advantage of  $\text{EuCl}_2$  is confirmed by XANES measurements giving 88 % and 83 % relative  $\text{Eu}^{2+}$  content for  $\text{EuCl}_2$  and  $\text{EuF}_2$  doping, respectively [65]. Note, that europium doping level was only 2 mol% in those XANES measurements. The following investigations are done with the  $\text{EuCl}_2$ -doped FCZ glasses, having the highest  $\text{Eu}^{2+}$  fraction. The growth of  $\text{BaCl}_2$  nanocrystals in the glasses is achieved by annealing the glasses for 5 minutes at 300 °C. The glasses are annealed in either air or argon to determine if it is necessary to anneal in an inert atmosphere to keep the  $\text{Eu}^{2+}$  fraction high.

The Mössbauer spectra of the as-made glass, the glass annealed in air and the glass annealed in argon are compared in Figure 7.3. While the isomer shift is not influenced by the thermal treatment of the glasses (see Table 7.1), the linewidth is significantly reduced from 8.3 mm/s to about 7 mm/s after annealing, suggesting that the Eu is now in an ordered, i.e. crystalline, state. This can be explained by the formation of the  $\text{BaCl}_2$  nanocrystals in the glasses containing the europium ions. The  $\text{Eu}^{2+}$  fraction remains almost the same after both annealing in air and annealing in an argon atmosphere. In particular, annealing in an inert-argon atmosphere does not affect the  $\text{Eu}^{2+}$ -to- $\text{Eu}^{3+}$  ratio. This result is confirmed by [84], in which the  $\text{Eu}^{2+}$ -to- $\text{Eu}^{3+}$  ratio was also found to be unchanged after annealing in an inert-argon atmosphere. On the contrary, the relative  $\text{Eu}^{2+}$  content of the sample that was annealed in air decreased slightly (but barely significant) by about 5 %, which is consistent

## 7.2. Temperature dependence of the Mössbauer spectra

with a previous XANES study giving the same decrease after annealing in air [65]. Thus, it cannot be excluded that  $\text{Eu}^{2+}$  is partially oxidized on annealing the glasses in air. It should also be noted that heating can reduce  $\text{EuCl}_3$  to  $\text{EuCl}_2$  [83].

All in all, an analysis of the low temperature absorption lines allows for the following interpretations: Annealing in air or an inert atmosphere does not significantly affect the  $\text{Eu}^{2+}$  content. The results also show that the use of  $\text{EuCl}_2$  instead of  $\text{EuF}_2$  as a starting material results in about 20 % more of the europium in a divalent state. Furthermore, the Mössbauer linewidth narrowing indicates that  $\text{Eu}^{2+}$  moves to a more ordered (crystalline) environment after annealing. The temperature dependence and the exactness of the quantitative estimate of the fractions are considered in the next section.

## 7.2. Temperature dependence of the Mössbauer spectra

The temperature dependence of the Mössbauer spectra is studied for the FCZ – 5 mol%  $\text{EuCl}_2$  sample annealed in an argon atmosphere. In Figure 7.4 the Mössbauer spectra are shown for a set of different temperatures of the glass ceramic. The comparison clearly shows the continuous increase of the Mössbauer absorption strengths with decreasing sample temperature as described for the as-made glass (Figure 7.1). Besides this, the ratio of the areas under the  $\text{Eu}^{2+}$ -to- $\text{Eu}^{3+}$  absorption lines changes with temperature. Starting at an  $\text{Eu}^{2+}$ -to- $\text{Eu}^{3+}$  ratio of 78 : 22 at 275 K, it increases up to about 90 : 10 at 6 K. The errors for the line shifts and the linewidths in the table are the standard errors of the Lorentz fit parameters. The errors for the area fractions are estimated on the basis of the errors for the absorption strengths and the linewidths. For the presented low temperature Mössbauer measurements the errors for the  $\text{Eu}^{2+}$ -fractions are mostly about 4 % . For longer integration times the errors are reduced to about 1-2 % comparable to the errors achieved in XANES studies [84]. The temperature dependence can be described in terms of the Lamb-Mössbauer factor (or  $f$ -factor), which is the recoil free fraction determining the intensity of the Mössbauer effect.

The  $f$ -factor depends on the amplitude,  $x$ , of vibrations of the nuclei. For a harmonic oscillator the Lamb Mössbauer factor  $f$  can be described by

$$f = \exp\left(-\frac{E_\gamma^2}{(\hbar c)^2} \langle x^2 \rangle\right) \quad (7.1)$$

where  $E_\gamma$  is the energy of the emitted  $\gamma$ -radiation,  $\hbar$  is the reduced Planck constant, and  $c$  is the velocity of light.

In Figure 7.5, the temperature dependence of the  $f$ -factors deduced from the areas of absorption lines is shown for  $\text{Eu}^{2+}$  and  $\text{Eu}^{3+}$ . It is seen from the temperature dependence that the Mössbauer effect increases more for  $\text{Eu}^{2+}$  than

## 7. Investigation of the oxidation state of rare-earth ions: a Mössbauer study

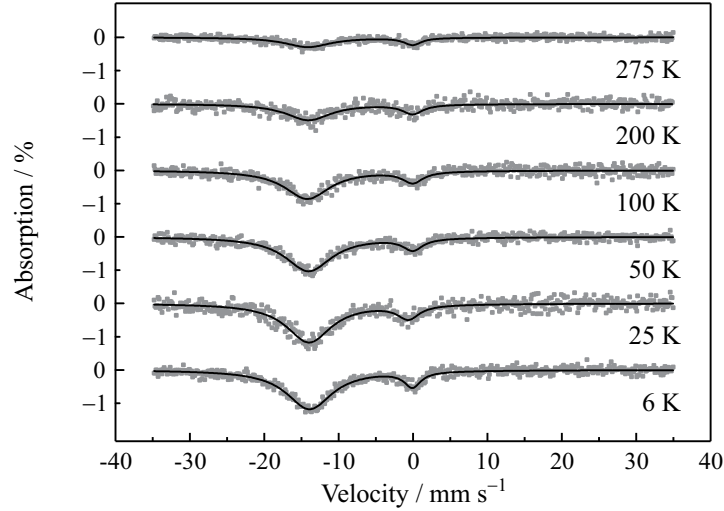


Figure 7.4.: Mössbauer spectra of a 5 mol%  $\text{EuCl}_2$ -doped FCZ glass annealed at  $300\text{ }^\circ\text{C}$  in argon atmosphere measured at different temperatures between 275 K and 6 K.

for  $\text{Eu}^{3+}$  due to the lower binding strength of  $\text{Eu}^{2+}$ . According to Equation 7.1 the  $f$ -factor decreases exponentially with the mean square amplitude of the vibrations.  $\text{Eu}^{2+}$  is less strongly bound so starting from absolute zero the amplitude of the thermal vibrations increases more rapidly than for the more strongly bound  $\text{Eu}^{3+}$ .

Describing the vibrations within the Debye model (as a first approximation) yields [85]

$$f = \exp\left(-\frac{3E_R}{2k_B\theta_D}\left[1 + 4\left(\frac{T}{\theta_D}\right)^2 \int_0^{\theta_D/T} \frac{x}{e^x - 1} dx\right]\right) \quad (7.2)$$

with  $E_R$  the recoil energy,  $k_B$  the Boltzmann constant,  $T$  the temperature, and  $\theta_D$  the Debye temperature. Least square fits are applied to the temperature dependence of the  $f$ -factors using Equation 7.2 and the recoil energy of  $^{151}\text{Eu}$ , which is  $E_R = 0.0017\text{ eV}$ . The fits, shown in Figure 7.5, yielded Debye temperatures of  $\theta_D = 147\text{ K}$  and  $186\text{ K}$  for  $\text{Eu}^{2+}$  and  $\text{Eu}^{3+}$ , respectively. The estimated Debye temperatures for the  $\text{Eu}^{2+}$  and  $\text{Eu}^{3+}$  in the glass ceramic are typical for those found for europium compounds [86, 87]. However, it should be pointed out that this estimation of the Debye temperatures is just a rough approximation. The errors for the  $f$ -factors, especially for  $\text{Eu}^{3+}$  are large. Besides experimental uncertainties, some simplifying assumptions in the Debye model, for example that an isotropic monatomic crystal lattice is present, are not satisfied.

At high temperatures ( $T \gg \theta_D$ ) Equation 7.2 can be written as

$$\ln f = \frac{-6E_RT}{k_B\theta_D^2} \quad (7.3)$$

## 7.2. Temperature dependence of the Mössbauer spectra

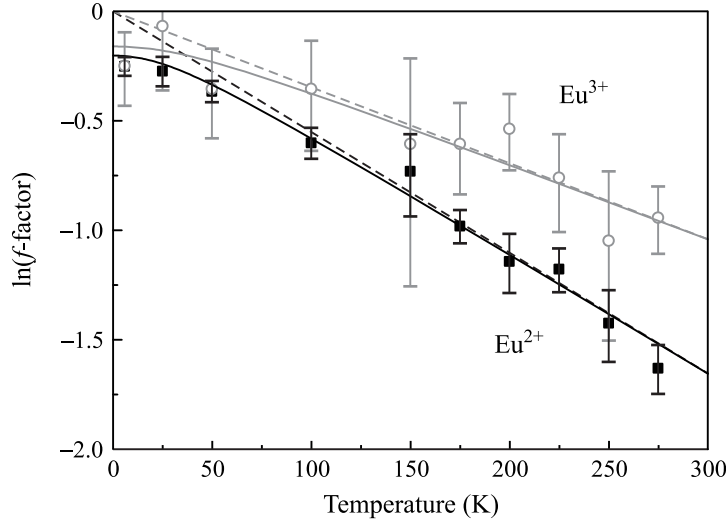


Figure 7.5.: Natural logarithm of the  $f$ -factors of  $\text{Eu}^{3+}$  (open circles) and  $\text{Eu}^{2+}$  (full squares) in a 5 mol%  $\text{EuCl}_2$ -doped FCZ glass annealed at 300 °C in an argon atmosphere versus the sample temperature. The solid lines are fits with the Debye temperatures  $\theta_D = 147$  K and 186 K for  $\text{Eu}^{2+}$  and  $\text{Eu}^{3+}$ , respectively. The dashed lines show the exponential temperature dependencies valid at high temperatures.

i.e.,  $\ln f$  decreases linearly with increasing temperature, which is seen from the high temperature data in Figure 7.5. According to Equation 7.2 the linear slope goes through  $f = 1$  at  $T = 0$  K. This enabled the  $f$  values to be deduced from the measured areas. Due to zero-point energy the amplitude of vibrations remains finite (i.e.  $f < 1$ ). The slope decreases at low temperatures.

At room temperature, the  $f$ -factors are low, about 0.4 for  $\text{Eu}^{3+}$  and only about 0.2 for  $\text{Eu}^{2+}$ . Thus, at room temperature the absorption areas are small and comparable in size for both,  $\text{Eu}^{3+}$  and  $\text{Eu}^{2+}$ , although the concentration of  $\text{Eu}^{2+}$  is much higher in the samples. By contrast, at low temperatures the  $f$ -factors are high and comparable. The  $f$ -factors extrapolated to  $T = 0$  K are 0.818 and 0.853 for  $\text{Eu}^{2+}$  and  $\text{Eu}^{3+}$ , respectively. The  $\text{Eu}^{2+}$ -to- $\text{Eu}^{3+}$  ratio of 89.4 : 10.6 extracted directly from the 6 K spectra changes only slightly upon correction with the corresponding  $f$ -factors (0.816 for  $\text{Eu}^{2+}$  and 0.852 for  $\text{Eu}^{3+}$ ); after correction a  $\text{Eu}^{2+}$ -to- $\text{Eu}^{3+}$  ratio of 89.8 : 10.2 is obtained. In case of the room temperature spectra, however, the  $\text{Eu}^{2+}$ -to- $\text{Eu}^{3+}$  ratio before  $f$ -factor correction (0.219 for  $\text{Eu}^{2+}$  and 0.382 for  $\text{Eu}^{3+}$ ) is 77.8 : 22.2 where it becomes 85.9 : 14.1 after correction.

The results show that deducing the  $\text{Eu}^{2+}$ -to- $\text{Eu}^{3+}$  ratio directly from the ratio of the areas under the low temperature absorption lines is already a good estimate, i.e. the  $f$ -factor correction is negligibly small, unlike at room temperature. This means that for an exact quantitative analysis, low temperature measurements or corrections with the corresponding  $f$ -factors are necessary.



## 8. Discussion

In the previous chapters, the measurements of the glasses and glass ceramics are analyzed in terms of assignments of the observed data and deductions of related physical quantities. In this chapter, the results are interpreted and placed into a wider context. Besides structural and phononic properties of the glasses and glass ceramics, the PL and MPR properties of the embedded rare-earth ions are considered. In particular, the PL efficiency enhancement is analyzed and explained in terms of modified MPR relaxation characteristics, which can be related to the phonon energies found for the formed  $\text{BaCl}_2$  nanocrystals. Some parts and figures of this chapter have already been published in Refs. [53, 68].

### 8.1. Nanocrystal formation and vibrational spectra

The XRD analysis in Chapter 4 shows that it was possible to induce the formation of  $\text{BaCl}_2$  nanocrystals in 1 mol%  $\text{Nd}^{3+}$ -doped FCZ glasses upon thermal processing. The average nanocrystal size increases with the annealing temperature. For low annealing temperatures, hexagonal  $\text{BaCl}_2$  nanocrystals are formed, whereas for higher annealing temperatures, the thermodynamically stable orthorhombic phase of  $\text{BaCl}_2$  is formed, similar to findings for  $\text{Eu}^{2+}$ -doped FCZ glasses [20, 53]. Such a phase transition is observed for the first time for  $\text{Nd}^{3+}$ -doped FCZ samples. To achieve a phase transition an annealing temperature was chosen according to the DSC data. In particular, one must be careful to not anneal in the range where the partial glass crystallization sets in, because the corresponding crystallization peak is close to the exothermic peak of the  $\text{BaCl}_2$  phase transition. In Chapter 4 it was found that with increasing annealing temperature the nanocrystal size increases by a factor of six, whereas the volume fraction of the nanocrystals remains basically constant. This indicates an Ostwald ripening process of the nanocrystals upon thermal processing [88]. During Ostwald ripening small crystallites dissolve and redeposit onto larger crystals until they reach their final size, which minimizes the total surface energy. Figure 8.1 illustrates schematically all formation stages of the nanocrystals as well as nucleation and Ostwald ripening. Although the width of the XRD reflections of the nanocrystals is too close to the instrumental resolution to allow a precise estimate of the particle size, the Scherrer analysis of the XRD pattern provides a first estimate. The structural data obtained from the XRD analysis are consistent with results from other methods of structural analysis.

## 8. Discussion

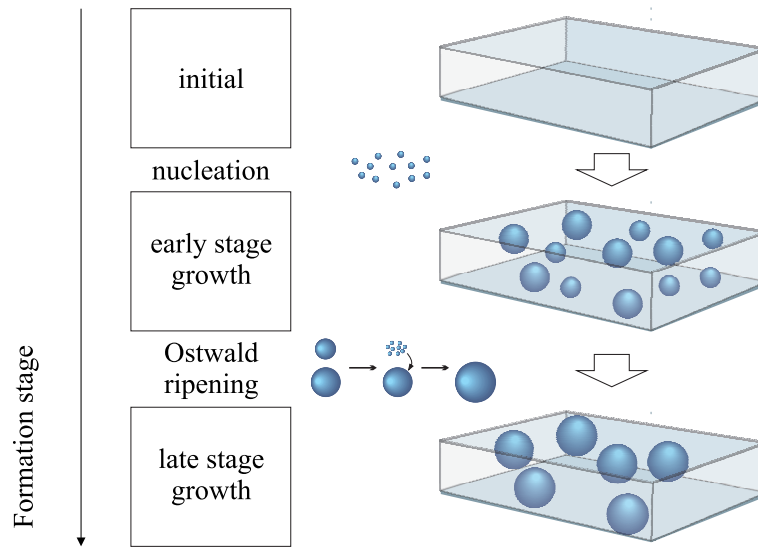


Figure 8.1.: Schematic illustration of the formation stages and Ostwald ripening of the BaCl<sub>2</sub> nanocrystals in FCZ glass upon thermal treatment.

It was possible to determine the nanocrystal size from the transmission spectra of the glass ceramics by a Rayleigh scattering model based analysis giving similar results to those of the Scherrer analysis [89]. Additionally, transmission electron microscopy (TEM) investigations on similar FCZ glass ceramics gave comparable nanocrystal sizes and volume fractions [20, 90]. These TEM measurements indicate a nanocrystal size distribution with a relative standard deviation of about 30 %.

Additional low energy phonon modes in the Raman measurements presented in Chapter 6 also reveal the formation of BaCl<sub>2</sub> nanocrystals and their structural phase transitions upon thermal treatment. As shown there, the Raman bands of the hexagonal nanocrystals exhibit larger Raman linewidths than those of the orthorhombic nanocrystals. This may be related to the smaller size of hexagonal nanocrystals (about 10 nm) in comparison to the orthorhombic nanocrystals (about 60 nm). With decreasing nanocrystal size broader linewidths are observed; Raman line broadening is an expected effect of phonon confinement in nanocrystals [91]. In some studies simple phenomenological models are used to obtain nanocrystal sizes from the Raman line shapes (see for example Ref. [92]). However, Rolo and Vasilevskiy [91] advise caution in this respect. One problem with this is the size distribution of the nanocrystals, which is usually broad. Moreover, large widths may be caused by disorder effects such as poor crystalline quality or shape irregularities, beyond the phonon confinement effect [91]. A shift in the position of the Raman peaks in comparison to the corresponding phonon energy in bulk crystal, which is another expected effect of low dimensional crystals [91, 93] is not observed. Thus, the line broadening may be related to disorder and a broader size distribution occurring at early formation stages

## 8.2. Interaction of rare-earth ions with BaCl<sub>2</sub> nanocrystals

of the nanocrystals; there is no clear indication for the occurrence of quantum confinement effects. This is evident, because phonon confinement becomes noticeable in the spectra only when the crystal size is smaller than typically 20 lattice constants [93]. In BaCl<sub>2</sub> having lattice constants of about 0.1 nm [48], this limiting size is approximately 2 nm and is thus about five times smaller than the average crystal size estimated for the hexagonal nanocrystals. The Raman data of orthorhombic BaCl<sub>2</sub> are in agreement with literature data [42]; the hexagonal phase of BaCl<sub>2</sub> was not investigated before.

In Section 6.3 it is shown that the applied first principles approach is capable of predicting phonon frequencies of BaCl<sub>2</sub> in hexagonal and orthorhombic symmetry. The calculation enables symmetry adapted mode types to be assigned to the observed BaCl<sub>2</sub>-related phonon modes. Additionally, a comparison of measured Raman spectra of the nanocrystals in the glasses and of the calculated Raman spectra confirms that the orientation of the nanocrystals is random. Section 6.3 also shows that it is possible to estimate the energies of all phonon modes of hexagonal and orthorhombic BaCl<sub>2</sub> by means of DFT calculations. Thus, their highest energy phonon modes can be determined. The highest energy phonon modes of rare-earth host materials are most important for the MPR. Table 8.1 lists the estimated maximum phonon energies of all relevant rare-earth hosts in this work. The cut-off phonon energies of the base glasses do not differ significantly except for the annealed glasses, in which the maximum energy is approximately 590 cm<sup>-1</sup>, which is about 10 cm<sup>-1</sup> higher than in the as-made glasses. The embedded nanocrystals provide much lower phonon energies than the base glasses. For hexagonal and orthorhombic BaCl<sub>2</sub> nanocrystals, the cut-off energy is about 224 cm<sup>-1</sup> and 213 cm<sup>-1</sup>, respectively.

The observed glass-related Raman bands can easily be interpreted by a comparison to Raman spectra of various compositions of FZ-based glasses given in the literature [78, 80, 17, 79]. The analysis of the glass-related Raman bands in Section 6.6 reveals that the base glass structure is not significantly affected by the chlorine nor by the thermal treatment, which induces the nanocrystal formation. The analysis indicates that some bridging fluorine atoms of the ZrF<sub>6</sub> octahedra are substituted by chlorine atoms when going from FZ to FCZ glasses. The thermal treatment induces the BaCl<sub>2</sub> nanocrystal formation and thus leads to a reduced halide-to-zirconium ratio in the base glass, which causes a shift of about 10 cm<sup>-1</sup> in the maximum phonon energy of the base glass.

## 8.2. Interaction of rare-earth ions with BaCl<sub>2</sub> nanocrystals and effect of their structural phase and size

The luminescence enhancement and the reduced nonradiative relaxation rates found in Chapter 5 can be explained by a partial incorporation of the neodymium ions into the hexagonal BaCl<sub>2</sub> nanocrystals. The strongly increased lumines-

## 8. Discussion

Table 8.1.: Determined maximum phonon energies  $\hbar\omega_{\max}$  (given in  $\text{cm}^{-1}$ ) of the different analyzed materials: hexagonal ( $P\bar{6}2m$  structure) and orthorhombic ( $Pnma$  structure)  $\text{BaCl}_2$ , as-made FZ glass matrix (FZ), as-made FCZ glass matrix (FCZ), and FCZ glass matrix annealed at 260 °C (FCZ-c).

$\text{BaCl}_2$ $P\bar{6}2m$	$\text{BaCl}_2$ $Pnma$	FZ	FCZ	FCZ-c
224	213	576	580	589

cence intensities and lifetimes (see Table 5.13) of various  $\text{Nd}^{3+}$  levels after the hexagonal nanocrystal formation are unusual for FZ-based glasses, but typical for low phonon energy crystals. As a representative example for the intensity enhancement investigated in Sections 5.1 - 5.2, Figure 8.2 shows selected emissions from the levels ( ${}^4G_{5/2}$ ,  ${}^2G_{7/2}$ ) and ( ${}^4G_{7/2}$ ,  ${}^2K_{13/2}$ ,  ${}^4G_{9/2}$ ). As stated above, only for levels with small energy gaps is a luminescence enhancement expected when the  $\text{Nd}^{3+}$  environment becomes crystalline. All levels other than the metastable  ${}^4F_{3/2}$  level have a sufficiently small energy gap; Figure 8.3 presents an example of the emission from this metastable level. Besides the deduced low MPR rates (see Table 5.13), a clear indication for a nanocrystal environment is the energy of the phonons emitted in the MPR, which is estimated from the fit of the temperature dependence in Section 5.5 to be  $258 \text{ cm}^{-1}$ . It matches quite well the maximum phonon energy of hexagonal  $\text{BaCl}_2$  nanocrystals estimated from Raman investigations to be  $224 \text{ cm}^{-1}$  (the cut-off phonon energies are summarized in Table 8.1). As mentioned above, the highest energy phonons are most important for MPR since they conserve energy in the lowest order process. This indicates that the  $\text{Nd}^{3+}$  ions are incorporated in the low phonon energy  $\text{BaCl}_2$  nanocrystals. The maximum phonon energy of the glass matrix of about  $590 \text{ cm}^{-1}$  is much higher than the energy of the involved phonons. Even  $\text{Nd}^{3+}$  ions at the nanocrystal/base glass interface may preferably interact with  $\text{BaCl}_2$  phonons, because the glass network vibrations are strongly localized [27]. As mentioned above, a direct comparison to  $\text{Nd}^{3+}$  in bulk crystals is not possible since the hexagonal crystalline phase of  $\text{BaCl}_2$  is metastable and cannot be grown as bulk crystals. However, MPR rates as low as in the FCZ glass ceramic are found in laser crystals. For example, Orlovskii *et al.* [43] report a MPR rate of approximately  $1 \cdot 10^5 \text{ s}^{-1}$  for ( ${}^4G_{5/2}$ ,  ${}^2G_{7/2}$ ) in  $\text{Nd}^{3+}$ -doped  $\text{PbCl}_2$  crystals (with  $\hbar\omega_{\max} \approx 200 \text{ cm}^{-1}$  [42]) in agreement to the corresponding MPR rate found for the glass ceramic. For the glass matrix on the contrary, a much higher MPR rate of about  $1 \cdot 10^7 \text{ s}^{-1}$  is found, which is characteristic for a level with such an energy gap in FZ-based glasses [39]. Beyond that, the host-specific parameters determined from the energy gap dependence of the MPR rates in Section 8.3 are similar to those of crystals; this supports the hypothesis.

The interaction with the  $\text{BaCl}_2$  phonons observed in this work is the first clear indication for an association of trivalent rare-earth ions with the  $\text{BaCl}_2$

## 8.2. Interaction of rare-earth ions with BaCl<sub>2</sub> nanocrystals

nanocrystals. In case of glass ceramics doped with divalent europium, it was already shown that the Eu<sup>2+</sup> ions are incorporated in the BaCl<sub>2</sub> nanocrystals, e.g. by a partial substitution of the Ba<sup>2+</sup> ions by Eu<sup>2+</sup> ions [20]. In addition, the reduced linewidths in the Eu<sup>2+</sup> Mössbauer spectra presented in Chapter 7 indicate that Eu<sup>2+</sup> moves to a crystalline environment after the nanocrystal formation. Despite of the different charges, also trivalent rare-earth ions such as Nd<sup>3+</sup> may substitute Ba<sup>2+</sup> sites of the BaCl<sub>2</sub> nanocrystals. It has been shown for many alkaline-earth halide crystals that trivalent rare-earth ions are substituted on the divalent alkaline-earth ion sites, for example as in case of Nd<sup>3+</sup> on Ca<sup>2+</sup> sites in CaF<sub>2</sub> crystals [94] or Nd<sup>3+</sup> ions on Sr<sup>2+</sup> sites in SrF<sub>2</sub> crystals [71]. As the rare-earth ions are normally on a trivalent site, charge compensation is required. Different charge compensation mechanisms have been examined in Ref. [95] by electron paramagnetic resonance (EPR) investigations. Commonly, the charge is compensated by a F<sup>-</sup> or Cl<sup>-</sup> ion in an interstitial position in a lattice cell next to the rare-earth ion; this is usually achieved by an alkali-metal halide doping. In the present case, the extra positive charge of the Nd<sup>3+</sup> ion in the BaCl<sub>2</sub> lattice is compensated by Cl<sup>-</sup> realized by the addition of the alkali-metal halide KCl to the sample composition (see Section 4.1).

In this work, the environment of the rare-earth ions is only analyzed by spectroscopic methods. However, there are other methods that can even directly visualize the atomic positions of the rare-earth ions. For this purpose, efforts are made to analyze rare-earth doped FCZ glass ceramics by atom-probe tomography (ATP).

It might be reasonably assumed that the neodymium ions are partially incorporated in the FZ-base glass; not all the Nd<sup>3+</sup> ions are located in the nanocrystals. A part of the Nd<sup>3+</sup> ions can remain at the different anion sites (see Ref. [61]) of the FZ-based glass network, which has a larger volume fraction than the nanocrystals being about 80 % (see Section 4.2). This means that a combination of the emissions from Nd<sup>3+</sup> ions in the nanocrystals and from Nd<sup>3+</sup> ions in the glass is measured. Thus, the PL emission bands in the glass ceramics are not as narrow as in a crystal. This is for example clearly visible for the <sup>4</sup>F<sub>3/2</sub> → <sup>4</sup>I<sub>9/2</sub> emission shown in Figure 8.3. In the 260 °C glass ceramic, the emission is narrower and shows a stronger splitting than in the as-made glass, but not as much as in a bulk crystal. However, the luminescence lifetimes of emissions bands from this metastable level are similar for the glass and the nanocrystals, because the MPR rates of <sup>4</sup>F<sub>3/2</sub> are negligible for both and the radiative rates depend only barely on the host. For time-resolved PL decay measurements of levels, for which the MPR has a significant influence, the contribution of the emissions from Nd<sup>3+</sup> ions in the glass is negligible, because these emissions are superimposed by the much stronger and longer living emissions from Nd<sup>3+</sup> ions in the nanocrystals (see Section 5.3). The PL properties of Nd<sup>3+</sup> in the glass are investigated separately in the as-made samples.

## 8. Discussion

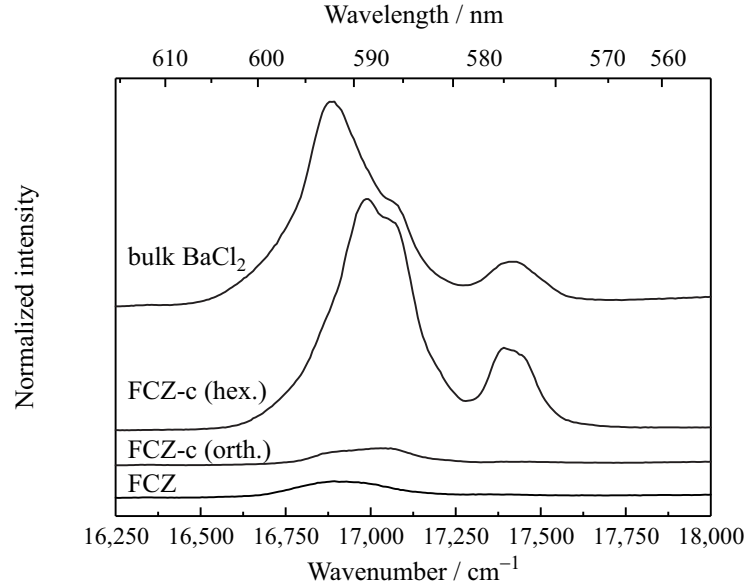


Figure 8.2.: PL spectra of the 1 mol%  $\text{Nd}^{3+}$ -doped FCZ glasses and glass ceramics and of 100 ppm  $\text{Nd}^{3+}$ -doped bulk  $\text{BaCl}_2$  in the range of the  $(^4\text{G}_{5/2}, ^2\text{G}_{7/2}) \rightarrow ^4\text{I}_{9/2}$  and  $(^4\text{G}_{7/2}, ^2\text{K}_{13/2}, ^4\text{G}_{9/2}) \rightarrow ^4\text{I}_{11/2}$  emission. From bottom to top: as-made FCZ; FCZ annealed at 260 °C (FCZ glass ceramic with hexagonal  $\text{BaCl}_2$  nanocrystals) and 280 °C (FCZ glass ceramic with orthorhombic  $\text{BaCl}_2$  nanocrystals); and bulk  $\text{BaCl}_2$ .  $\text{Nd}^{3+}$  was excited at 515 nm in resonance with the  $^4\text{I}_{9/2}$  to  $(^4\text{G}_{7/2}, ^2\text{K}_{13/2}, ^4\text{G}_{9/2})$  transition. The spectra are normalized to the  $^4\text{F}_{3/2} \rightarrow ^4\text{I}_{9/2}$  emission at about 870 nm and vertically displaced for clarity.

Additionally, it can be concluded from the PL measurements that the  $\text{Nd}^{3+}$  ions are not properly incorporated in the orthorhombic  $\text{BaCl}_2$  nanocrystals, in contrast to the case of hexagonal  $\text{BaCl}_2$  nanocrystals. This conclusion is drawn, because the formation of the orthorhombic nanocrystals does not lead to any PL enhancement, although the  $\text{Nd}^{3+}$  ions in the corresponding bulk crystal show much stronger PL emissions than the as-made glass (see for example Figure 8.2). Taking into account the fact that nanocrystals try to minimize their potential energy during the growth process, gives an explanation. There is some evidence that the rare-earth ions act as nucleation centers triggering the crystallization [65]. As stated above, at the beginning of the crystallization process, hexagonal nanocrystals that are directly associated with the  $\text{Nd}^{3+}$  ions are formed. Subsequently, the nanocrystals undergo a phase transition from the metastable hexagonal to the orthorhombic structure in order to stabilize thermodynamically. Similarly, the crystals try to stabilize by delocalizing the  $\text{Nd}^{3+}$  ions outside. In order to obtain samples with hexagonal phase  $\text{BaCl}_2$  nanocrystals the thermal treatment is stopped at lower temperatures. Thus, the  $\text{Nd}^{3+}$  ions presumably remain quasi frozen in their current states explaining the association of the hexagonal nanocrystals with the neodymium. Whereas the continuation of the growth process which is necessary to obtain samples with

## 8.2. Interaction of rare-earth ions with BaCl<sub>2</sub> nanocrystals

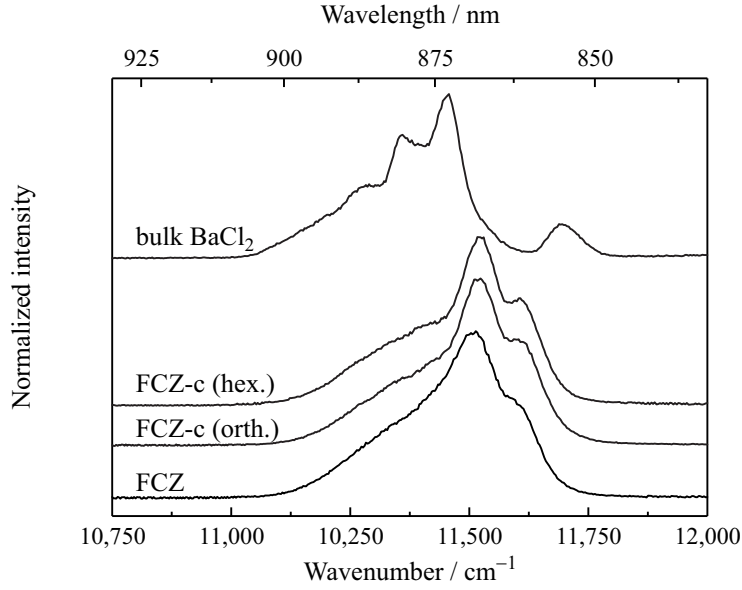


Figure 8.3.: PL spectra of the 1 mol% Nd<sup>3+</sup>-doped FCZ glasses and glass ceramics and of 100 ppm Nd<sup>3+</sup>-doped bulk BaCl<sub>2</sub> in the range of the <sup>4</sup>F<sub>3/2</sub> → <sup>4</sup>I<sub>9/2</sub> emission. From bottom to top: as-made FCZ; FCZ annealed at 260 °C (FCZ glass ceramic with hexagonal BaCl<sub>2</sub> nanocrystals) and 280 °C (FCZ glass ceramic with orthorhombic BaCl<sub>2</sub> nanocrystals); and bulk BaCl<sub>2</sub>. Nd<sup>3+</sup> was excited at 515 nm in resonance with the <sup>4</sup>I<sub>9/2</sub> to (<sup>4</sup>G<sub>7/2</sub>, <sup>2</sup>K<sub>13/2</sub>, <sup>4</sup>G<sub>9/2</sub>) transition. The spectra are normalized to the <sup>4</sup>F<sub>3/2</sub> → <sup>4</sup>I<sub>9/2</sub> emission at about 870 nm and vertically displaced for clarity.

orthorhombic nanocrystals leads to the delocalization of the Nd<sup>3+</sup> ions. Note that the phase transition of the nanocrystals can either be achieved by treating the samples at different temperatures up to about 280 °C as done in the present work or by holding the samples at about 280 °C for different time periods of between a few seconds and 20 min [53]. It should also be noted, that spatially resolved PL measurements on the Nd<sup>3+</sup>-doped bulk BaCl<sub>2</sub> crystal indicate that the Nd<sup>3+</sup> ions are not uniformly distributed in the crystal, which further confirms an inadequate incorporation of the Nd<sup>3+</sup> ions into orthorhombic BaCl<sub>2</sub>.

Another finding of this thesis is that the luminescence intensity of the glass ceramics decreases with increasing nanocrystal size. This is clearly visible from the PL measurements or rather from the absolute quantum efficiency measurements in Chapter 5. The 240 °C sample, which has the smallest average BaCl<sub>2</sub> crystallite diameter, displays the largest efficiency enhancement (see Figure 5.8). However, the transition rates are not influenced by the nanocrystal size. As presented in Table 5.3, the experimental luminescence decay time of the glass ceramics, which show a luminescence enhancement, does not depend on the crystallite size. It is known for the present samples that the radiative decay rate does not change significantly with the crystallite size [72]. Concerning the unaffected total decay time, it can be concluded that also the MPR rate does not change with the crystallite size. This is evident since the phonon modes

## 8. Discussion

of the hexagonal  $\text{BaCl}_2$  nanocrystals do not change with the crystallite size. As discussed in Section 8.1, phonon quantum confinement effects and thus size effects on the MPR rates are not expected here. The difference in the radiative decay rate when going from bulk samples to nanocrystals is basically related to effects of surrounding media on the optical properties that are determined by the effective refractive index of the nanocrystals and the embedding matrix [96]. Due to the relatively similar refractive indices of the FZ-based glass ( $n = 1.50$  nm at  $\lambda = 600$  nm) and  $\text{BaCl}_2$  ( $n = 1.65$  nm at  $\lambda = 600$  nm) [97, 98], the radiative decay rate was calculated to depend only barely on the crystallite size [72]. Rather, the decreasing luminescence intensity with the increasing nanocrystal size may be related to a smaller portion of emissions from  $\text{Nd}^{3+}$  ions in the nanocrystals. The following reasons support this hypothesis. Firstly, as discussed above, the  $\text{Nd}^{3+}$  ions are expected to move out of the nanocrystals during the growth process. In case of the 240 °C sample, this process is aborted at the lowest annealing step and thus the largest amount of  $\text{Nd}^{3+}$  ions remains in the crystallites. Secondly, the maximum luminescence intensity in the sample with the smallest nanocrystals can be related to the largest total surface area of the nanocrystals. As found in the structural analysis, the volume fraction of the nanocrystals is similar in all glass ceramics (about 20 %). Since the 240 °C glass ceramic exhibits the smallest average crystallite size, it provides the largest total surface area of the luminescent  $\text{BaCl}_2$  nanocrystals leading to efficient emissions. Note that  $\text{Nd}^{3+}$  ions that are close to the crystals surface have a larger probability to contribute to luminescence than those located near the center due to geometry considerations and to reflection and absorption/reabsorption processes.

The difference in the luminescence intensity of  $\text{Nd}^{3+}$  in glass and glass ceramic is already qualitatively explained by means of the different MPR rates; it will be analyzed in detail in the following sections. Finally, the different spectral features in the PL spectra that are clearly visible in Figures 8.2 and 8.3 are shortly commented here; a detailed analysis is not within the scope of this work. The PL emission bands of bulk  $\text{BaCl}_2$  and of the 260 °C glass ceramic, which shows an association with crystalline  $\text{BaCl}_2$ , exhibit different line splittings and different line shifts. These host-dependent shifts and splittings of the free-ion levels are determined by the crystal field of the rare-earth environment (see Section 2.1.1). Thus, the differences can be explained by the fact that different crystalline phases of  $\text{BaCl}_2$  are present in these two samples, i.e. orthorhombic and hexagonal  $\text{BaCl}_2$  for the bulk crystal and the 260 °C glass ceramic, respectively. Additionally, in the glass ceramic, the  $\text{Nd}^{3+}$  ions are not only incorporated in the crystalline environment, but also in the base glass. This mixed character also explains why the emission bands of this glass ceramic are also shifted relative to those of the as-made glass. Also the emission bands of the 280 °C glass ceramic are significantly shifted with respect to those of the

### 8.3. Comparison and energy gap dependence of the MPR rates

as-made glass. Although the  $\text{Nd}^{3+}$  ions are not incorporated in the sample's orthorhombic nanocrystals, this shift is not a contradiction, as the  $\text{Nd}^{3+}$  ions can be influenced by the nanocrystals' crystal field. Furthermore, the composition of the base glass is modified by the heat treatment (see Section 8.1). When considering the PL spectra of the samples with hexagonal  $\text{BaCl}_2$  nanocrystals, it is important to always keep in mind that the contribution from  $\text{Nd}^{3+}$  ions in the base glass (with respect to the contribution from  $\text{Nd}^{3+}$  in the nanocrystals) is significant for emissions from the  ${}^4\text{F}_{3/2}$  level, whereas it becomes negligible for emissions from the higher lying levels. This is related to the strong luminescence quenching of emissions from these closely spaced levels in the base glass.

### 8.3. Comparison and energy gap dependence of the multiphonon relaxation rates

In Figure 8.4, the MPR relaxation rates estimated in Chapter 5 for the FCZ glass ceramic (heat-treated at 260 °C), the as-made FCZ glass, and the standard FZ glass are plotted on a logarithmic scale as a function of the energy gap. The energy gap  $\Delta E$  is the energy difference between the corresponding  $\text{Nd}^{3+}$  level and its next lower level. The FCZ glass ceramic shows the lowest MPR rates following an exponential dependence on the energy gap as predicted from the theory described in Section 2.2.1. As stated there, such exponential relation was found for various glasses and crystals. Empirically, the so-called ‘‘energy gap law’’ was formulated as [32]:

$$W_{\text{MPR}} = C \cdot \exp(-\alpha \cdot \Delta E) , \quad (8.1)$$

which is in agreement with Equation 2.11.  $C$  and  $\alpha$  are constants which depend only on the host material. They allow for an estimate of the MPR rates for any rare-earth ion in the host.  $C$  is the MPR rate extrapolated to zero energy gap  $\Delta E$ , while  $\alpha$  expresses the dependence of the MPR on the electron-phonon coupling constant  $\epsilon$  and on the maximum phonon energy  $\hbar\omega_{\text{max}}$  (see Section 2.2.1) of the host material, i.e.

$$\alpha = \frac{-\ln(\epsilon)}{\hbar\omega_{\text{max}}} . \quad (8.2)$$

For the FZ glass, MPR rates for two gaps could be determined, namely  $5.0 \cdot 10^6 \text{ s}^{-1}$  and  $1.1 \cdot 10^6 \text{ s}^{-1}$  for  $1,347 \text{ cm}^{-1}$  and  $1,842 \text{ cm}^{-1}$ , respectively (two data points in Figure 8.4). Using these values,  $C = 3.0 \cdot 10^8 \text{ s}^{-1}$  and  $\alpha = 3.0 \cdot 10^{-3} \text{ cm}$  are obtained from Equation 8.1. This agrees quite well with literature values for FZ glasses [39, 73]. For the as-made FCZ glass, the MPR rates are  $4.9 \cdot 10^5 \text{ s}^{-1}$  and  $5.7 \cdot 10^4 \text{ s}^{-1}$  for an energy separation of  $1,359 \text{ cm}^{-1}$  and  $1,829 \text{ cm}^{-1}$ , respectively, which yields  $C = 2.5 \cdot 10^8 \text{ s}^{-1}$  and  $\alpha = 4.6 \cdot 10^{-3} \text{ cm}$ . In the case

## 8. Discussion

of the FCZ glass ceramic (total of 6 data points), a least squares fit yields  $C = (1.4 \pm 0.1) \cdot 10^7 \text{ s}^{-1}$  and  $\alpha = (3.8 \pm 0.4) \cdot 10^{-3} \text{ cm}$ .

The  $C$  values of the as-made FZ and FCZ glasses are very close to each other, while the  $C$  of the FCZ glass ceramic is more than one order of magnitude smaller. This is attributed to the low cut-off phonon energy of the  $\text{BaCl}_2$  nanocrystals ( $\hbar\omega_{\text{max}} = 224 \text{ cm}^{-1}$ ). Both, the FZ and the FCZ glass, have maximum phonon energies of about  $590 \text{ cm}^{-1}$ , in good agreement with the observation of approximately the same  $C$  values for the glasses without nanocrystals. The estimated  $\alpha$  value of the FCZ glass is slightly higher than that of the FZ glass. A larger  $\alpha$  value but a similar  $\hbar\omega_{\text{max}}$  for the FCZ glass, results from the lower electron-phonon coupling strength  $\epsilon$  (see Equation 8.2) in agreement with previous results [99], where it was found that the addition of chlorine decreases the electron-phonon coupling strength in FZ glasses. The FCZ glass ceramic on the contrary, has the distinctly highest electron-phonon coupling strength  $\epsilon$  which stems from the lowest  $\hbar\omega_{\text{max}}$  and the almost unaffected  $\alpha$ . According to Section 2.2.1, the electron-phonon coupling constant,  $\epsilon$ , is defined as the  $W_{\text{MPR}}^{(p)}$ -to- $W_{\text{MPR}}^{(p-1)}$ -ratio, i.e. the ratio of the  $p$ -order and the  $(p - 1)$ -order MPR rates. In host materials with low  $\hbar\omega_{\text{max}}$ , the number  $p$  of phonons involved in a MPR process is relatively large. Thus,  $W_{\text{MPR}}^{(p)}$  is comparable to  $W_{\text{MPR}}^{(p-1)}$  resulting in a large  $\epsilon$  which is close to unity.

Figure 8.5 shows the “energy gap laws” of various common glasses [27, 39, 41] in comparison to the result obtained for the FCZ glass ceramic. The comparison shows that the glass ceramic exhibits extremely low MPR rates, which are several orders of magnitude lower than in the conventional glasses. Only above approximately  $2500 \text{ cm}^{-1}$  does the difference between the FCZ glass ceramic and FZ glass fall below one order of magnitude; but usually for such large energy gaps the influence of the MPR rate on the luminescence efficiency becomes negligible anyway. These excellent MPR properties are caused by the interaction of the rare-earth ions with phonons of the  $\text{BaCl}_2$  nanocrystals, as the temperature-dependent analysis of the relaxation processes shows (see discussion in Section 8.2). As stated in Section 2.2, the MPR rate decreases significantly with decreasing cut-off phonon energy of the environment.

This “energy gap law” emphasizes the glass ceramic’s potential as a low phonon energy rare-earth host for PL applications. The resulting positive effects on the luminescence efficiencies are discussed in the next section. Empirically, it was found for crystals and glasses that once the host specific constants  $C$  and  $\alpha$  are known from the corresponding “energy gap law”, they give the MPR rates of any rare-earth ion in the material with an accuracy of about a factor of two [32]. Thus, it is expected that also other rare-earth ions than  $\text{Nd}^{3+}$  should provide such low MPR rates when embedded in the FCZ glass ceramic.

Apparently, this is the first time that an “energy gap law” has been observed for a glass ceramic. It also shows a general potential of glass ceramics for lu-

### 8.3. Comparison and energy gap dependence of the MPR rates

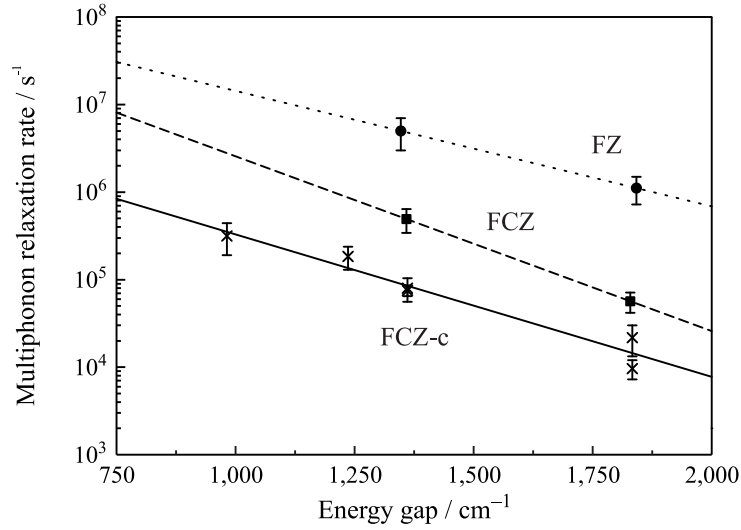


Figure 8.4.: Room temperature MPR rates of  $\text{Nd}^{3+}$  in the FZ-based glasses and glass ceramics as a function of the energy gap to the next lower level: as-made FZ glass (circles), as-made FCZ glass (squares), and FCZ glass annealed at 260 °C (FCZ-c) (crosses). All samples are doped with 1 mol%  $\text{Nd}^{3+}$ . The lines represent the corresponding energy gap law given by Equation 8.1. The error bars indicate the maximum estimated error which is between 20 % and 40 %.

minescence applications, which cannot be achieved with conventional glasses. Also for other kinds of glasses, e.g. for silicon oxide glasses, it can be supposed that such a nanocrystallization can distinctly reduce their MPR losses. Studies that demonstrate improved rare-earth emission intensities by nanocrystal formation in other glass ceramic systems already exist. Especially for various kinds of transparent oxyfluoride glass ceramics, which consist of an oxide base glass and fluoride crystallites, enhanced upconversion intensities and PL lifetimes were reported [100, 101, 102]. Also for oxychloride systems, such as phosphate oxide glass ceramics containing  $\text{CaCl}_2$  nanocrystals, first comparable reports exist [103]. In all these studies the authors proposed that the observed enhancements result from an incorporation of the rare-earth ions in the low phonon energy halide crystallites. However, they did not further investigate the MPR properties.

The advantage of such glass-ceramic systems is that they combine the luminescence properties of a halide crystal with the mechanical properties of a glass. The low MPR losses enable efficient PL emissions. It has been shown that also scattering losses in glass ceramics with crystallites of nanometer size are as low as in optical glasses or in single crystals making them applicable for fiber amplifiers [10]. Compared to single crystals, the fabrication of glasses and glass ceramics is less challenging and the achievable size is not limited. In addition, they can be drawn into fibers enabling further applications.

Glass ceramics could be applied to luminescence and lasing devices using emissions from rare-earth levels which are usually quenched in glasses. For

## 8. Discussion

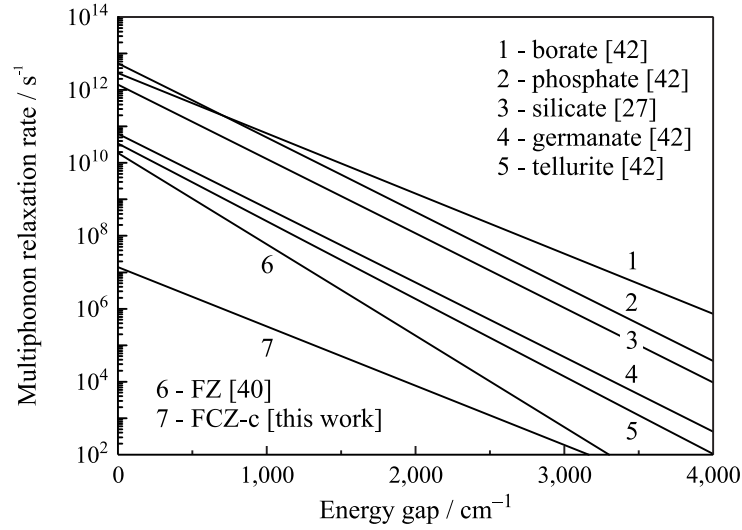


Figure 8.5.: Energy gap dependencies of the MPR rates of rare-earth ions in various glasses in comparison to the energy gap law of the 1 mol% Nd<sup>3+</sup>-doped FCZ glass ceramic (FCZ-c) (FCZ glass annealed at 260 °C), which was analyzed in this work [41, 27, 39].

example, FCZ glass ceramics could be interesting for Dy<sup>3+</sup> fiber amplifiers operating at 1.3  $\mu\text{m}$ . The system requires a low phonon energy host for high efficiency, because the corresponding emitting level (<sup>6</sup>H<sub>9/2</sub>, <sup>6</sup>F<sub>11/2</sub>) has a small energy separation of only 2,000 cm<sup>-1</sup> to its subjacent level [104]. The most attracting application of oxyfluoride glass ceramics is a Pr<sup>3+</sup>-doped fiber amplifier providing efficient luminescence at 1.3  $\mu\text{m}$  [105].

It might be argued that other glasses, such as other halide glasses or chalcogenide glasses, with maximum phonon energies of about 300 cm<sup>-1</sup> [41] are alternative candidates. However, they do not attract interest for most applications due to their low mechanical and chemical stabilities and their low resistance to atmospheric moisture compared to FZ-based glasses.

It should be emphasized at this point that the “energy gap law” refers only to the Nd<sup>3+</sup> ions which are incorporated into the BaCl<sub>2</sub> nanocrystals, as the above analysis indicates. Presumably, for such glass-ceramic systems, it is unavoidable that a part of the rare-earth ions remain in the base glass and contributes to the PL spectrum. However, due to the higher phonon energy of the base glass, this contribution may be small or even negligible as described for the present system.

### 8.4. Quantum efficiencies

A quantity highlighting the importance of low phonon energy rare-earth host materials is the radiative quantum efficiency. According to Equation 2.2, the

radiative quantum efficiency is defined by

$$\eta = \frac{\sum A}{\sum A + W_{\text{MPR}}} \quad (8.3)$$

when MPR processes dominate the nonradiative decay [106].  $\eta$  can be calculated for the respective level if its MPR rate  $W_{\text{MPR}}$  and its total radiative decay rate  $\sum A$  are known.

For a deeper analysis of the influence of the MPR rates on the PL properties, Table 8.2 compares radiative quantum efficiencies  $\eta$  of the FCZ glass ceramic, the as-made FCZ glass, and the standard FZ glass. The radiative quantum efficiencies of the different  $\text{Nd}^{3+}$  levels are estimated from the decay rates  $\sum A$  and  $W_{\text{MPR}}$  by using Equation 8.3. The MPR rates are obtained from the corresponding energy gap laws described above (Equation 8.1, Figure 8.4). Only the  $\text{Nd}^{3+}$  levels, which are not influenced by  ${}^4\text{F}_{3/2}$  via MPA, are considered. A comparison of the radiative quantum efficiencies shows that the  $\text{BaCl}_2$  nanocrystals have a positive effect on the  $\text{Nd}^{3+}$  luminescence properties. The radiative quantum efficiency is enhanced for the levels with small energy gaps whereas it is not influenced for the  ${}^4\text{F}_{3/2}$  level having a large energy separation.

For ( ${}^4\text{G}_{7/2}$ ,  ${}^2\text{K}_{13/2}$ ,  ${}^4\text{G}_{9/2}$ ), the calculated radiative quantum efficiency  $\eta$  is only about 0.2 % in the FZ glass which explains the strong luminescence quenching found for emissions from this level (see Figure 5.9). It is increased to about 4 % in the FCZ glass where the luminescence is slightly enhanced. An increase to about 13 % could be induced by the presence of  $\text{BaCl}_2$  nanocrystals. This is reflected by the strong luminescence enhancement observed for the FCZ glass ceramic. For ( ${}^4\text{G}_{5/2}$ ,  ${}^2\text{G}_{7/2}$ ), a similar behavior is observed: Radiative quantum efficiencies of about 0.1 %, 2 %, and 9 % in the FZ glass, in the FCZ glass, and in the FCZ glass ceramic are obtained, respectively. Also for  ${}^2\text{H}_{11/2}$  an efficiency enhancement is calculated. The radiative quantum efficiencies of the samples differ by about one order of magnitude, but  ${}^2\text{H}_{11/2}$  has very low radiative transition probabilities (see Table 5.5) leading to weak emissions from this level. For all levels with small energy gaps ( $< 2,000 \text{ cm}^{-1}$ ), the MPR transition probabilities are high in comparison to the radiative decay probabilities. The efficiency enhancements for these levels are caused by the modified MPR rates which change significantly with the host material.

For the  ${}^4\text{F}_{3/2}$  level on the contrary, the radiative transition rates dominate the decay. The MPR rates are negligibly small ( $W_{\text{MPR}} \ll A$ ) for all the samples due to the large energy gap. Thus, the radiative quantum efficiency of the  ${}^4\text{F}_{3/2}$   $\text{Nd}^{3+}$  level is approximately 100 % in all three host materials.

In summary, one can state that reduced MPR rates describe the luminescence enhancement found in Chapter 5 well. The PL spectra in Figure 5.9 show that exactly for these emissions from levels with small energy separations a corresponding luminescence enhancement is found. In this context, it is worth looking at the absolute quantum efficiency measurements, although they did

## 8. Discussion

Table 8.2.: Radiative quantum efficiencies  $\eta$  for various  $\text{Nd}^{3+}$  levels in the as-made FZ glass, in the as-made FCZ glass, and in the FCZ glass annealed at 260 °C (FCZ-c). The efficiencies were calculated via Equation 8.3 from the radiative decay rates  $\sum A$  (see Table 5.5) and from the MPR rates  $W_{\text{MPR}}$ , which were derived from the energy gap laws determined in this work (see Figure 8.4).

level	sample	$\eta$ (%)
${}^4\text{F}_{3/2}$	FZ	99
	FCZ	100
	FCZ-c	100
${}^2\text{H}_{11/2}$	FZ	0.003
	FCZ	0.04
	FCZ-c	0.2
$({}^4\text{G}_{5/2}, {}^2\text{G}_{7/2})$	FZ	0.1
	FCZ	2
	FCZ-c	9
$({}^4\text{G}_{7/2}, {}^2\text{K}_{13/2}, {}^4\text{G}_{9/2})$	FZ	0.2
	FCZ	4
	FCZ-c	13

not allow for isolated measurements of the single  $\text{Nd}^{3+}$  transitions and for an estimation of corresponding QE values of the FZ glass due to the sensitivity limit of the measurement system. Of course, the absolute values of the radiative quantum efficiency  $\eta$  and of the absolute quantum efficiency QE can not be compared, because they are different physical quantities by definition (see Equations 2.2 and 2.3). Besides the radiative quantum efficiencies of the rare-earth levels, other factors, such as the glass absorption, determine the absolute quantum efficiency  $\text{QE}(\lambda_{\text{ex}}, \lambda_{\text{em}})$ . However, at least the enhancement factors for both kinds of quantum efficiencies can be compared. The absolute quantum efficiency measurements confirm the results obtained from the calculation of the radiative quantum efficiencies. On the one hand, the absolute quantum efficiency measurements show that the emissions from  ${}^4\text{F}_{3/2}$  do not change significantly as illustrated in Figure 5.8. This is in agreement with the unaffected radiative quantum efficiencies of  ${}^4\text{F}_{3/2}$  (see Table 8.2). On the other hand, the measurements allow for a comparison of the efficiency enhancements for rare-earth levels with small energy gaps such as  $({}^4\text{G}_{7/2}, {}^2\text{K}_{13/2}, {}^4\text{G}_{9/2})$  and  $({}^4\text{G}_{5/2}, {}^2\text{G}_{7/2})$ . For instance, the radiative quantum efficiency calculations yield for both, the  $({}^4\text{G}_{7/2}, {}^2\text{K}_{13/2}, {}^4\text{G}_{9/2})$  and the  $({}^4\text{G}_{5/2}, {}^2\text{G}_{7/2})$  level, an enhancement factor of about 3-4 (see Table 8.2) when going from the as-made FCZ glass to the FCZ glass ceramic. This is in agreement with the fact that the enhancement factor of the measured average QE of the  $({}^4\text{G}_{7/2}, {}^2\text{K}_{13/2}, {}^4\text{G}_{9/2}) \rightarrow {}^4\text{I}_{13/2}$  and  $({}^4\text{G}_{5/2}, {}^2\text{G}_{7/2}) \rightarrow {}^4\text{I}_{11/2}$  emissions originating from these two levels is 3.3 (see

Figure 5.8).

Since it is shown in Section 5.2 that a normalization of the PL spectra to the  ${}^4F_{3/2} \rightarrow {}^4F_{9/2}$  emission is justified, the PL spectra in Figure 5.9 allow for a comparison of the glass ceramic and the standard FZ glass. For emissions from levels with small energy gaps ( $< 2,000 \text{ cm}^{-1}$ ), the measured PL enhancement factors are all about  $10^2$  in agreement with the corresponding enhancements obtained from the calculated radiative quantum efficiencies (see Table 8.2).

All in all, the obtained luminescent enhancements show that the glass ceramic is an attractive host exhibiting low MPR losses. In comparison to oxide glass the PL enhancement of the glass ceramic is even larger, because FZ-based glasses, which were analyzed for comparison, provide much lower phonon energies than oxide glasses.



## 9. Conclusion and outlook

In this thesis, rare-earth doped fluorozirconate (FZ)-based glasses and glass ceramics, which are of interest for various luminescence applications, were prepared and investigated in order to understand and optimize host-dependent mechanisms of rare-earth luminescence efficiency enhancement.

It was possible to initiate the growth of  $\text{BaCl}_2$  nanocrystals in 1 mol%  $\text{Nd}^{3+}$ -doped fluorochlorozirconate (FCZ) glasses by an appropriate thermal treatment. According to differential scanning calorimetry investigations of the crystallization behavior, different temperatures between 240 and 280 °C were applied for the thermal post processing of as-made glasses. For the first time, a structural phase transition of the  $\text{BaCl}_2$  nanocrystals was achieved in  $\text{Nd}^{3+}$ -doped FCZ glasses. The structure and the phonon spectra of these differently heat-treated glasses were investigated by X-ray diffraction, Raman, and *ab initio* studies. The average crystallite size increased with increasing annealing temperature. In glasses which were processed at 240, 250, and 260 °C, hexagonal  $\text{BaCl}_2$  ( $P\bar{6}2m$  structure) crystallites with an average diameter of 10-20 nm were formed. For the highest annealing temperatures of 270 and 280 °C, the crystallite diameter increased rapidly up to 60 nm. Annealing at 280 °C led to the formation of orthorhombic  $\text{BaCl}_2$  ( $Pnma$  structure) nanocrystals; in the 270 °C sample a mixture of both of these phases of  $\text{BaCl}_2$  was found.

Density functional theory calculations enabled a prediction and an assignment of all individual vibrational modes of  $\text{BaCl}_2$  in orthorhombic and hexagonal symmetry. Besides Raman-active phonon modes, infrared-active phonon modes were theoretically investigated. In addition, good agreement between calculated and experimental Raman spectra was found. The maximum phonon energy of both structural phases of  $\text{BaCl}_2$  was estimated to be  $224\text{ cm}^{-1}$  and  $213\text{ cm}^{-1}$  for hexagonal and orthorhombic symmetry, respectively. With the exception of a broader Raman line width, the Raman spectra of the embedded nanocrystals were found to coincide well with those of bulk  $\text{BaCl}_2$  crystals. Clear indications for phonon confinement effects were not observed. Except from the additional  $\text{BaCl}_2$ -related modes, the Raman spectra of the embedding FCZ glass matrices were not significantly affected by the thermal treatment. The glass-related Raman modes observed were quite similar to those of other standard FZ-based glasses such as ZBLAN; their maximum phonon frequency was estimated to be between about  $580$  and  $590\text{ cm}^{-1}$ .

## 9. Conclusion and outlook

Photoluminescence (PL) measurements have shown that the formation of hexagonal BaCl<sub>2</sub> nanocrystals led to strongly enhanced luminescence emission intensities from Nd<sup>3+</sup> levels which are usually quenched by multiphonon relaxation (MPR) processes in FZ-based glasses. However, the glass ceramics with orthorhombic nanocrystals did not exhibit any luminescence enhancement.

For an analysis of the luminescence enhancement, time-resolved PL of individual Nd<sup>3+</sup> levels was measured using different selective pulsed excitation wavelengths and the photon counting technique. The measurements showed distinctly longer PL lifetimes of several excited Nd<sup>3+</sup> levels after the formation of hexagonal BaCl<sub>2</sub> nanocrystals. The MPR dynamics of Nd<sup>3+</sup> was investigated in a FCZ glass ceramic with hexagonal BaCl<sub>2</sub> nanocrystals, in an as-made FCZ glass, and in a standard FZ glass (chlorine-free) with the ZBLAN formulation. The MPR rates of various Nd<sup>3+</sup> levels were estimated from the difference between measured total decay rates and purely radiative decay rates calculated from Judd-Ofelt theory. MPR rates were further obtained from the analysis of luminescence rise times as well as from the analysis of the temperature dependence of luminescence decay times. The rates found for the FCZ glass ceramic were extremely low, thus explaining the observed Nd<sup>3+</sup> luminescence enhancement. The MPR rates,  $W_{\text{MPR}}$ , of the different Nd<sup>3+</sup> levels showed an exponential dependence of the energy gap  $\Delta E$  to the corresponding next lower level, i.e. they follow the so-called “energy gap law” which was phenomenologically found for rare-earth ions in various crystals and glasses. It is generally expressed by  $W_{\text{MPR}} = C \cdot \exp(-\alpha \cdot \Delta E)$ . The constants characteristic for the host were determined for the glass ceramic to be  $C = 1.4 \cdot 10^7 \text{ s}^{-1}$  and  $\alpha = 3.8 \cdot 10^{-3} \text{ cm}$ . The corresponding rates were distinctly lower than those of the FZ and FCZ glasses; the chlorine-free sample provided the highest MPR rates, which were in agreement with literature values for FZ glasses. The rates obtained for the FCZ glass ceramic are more than four orders of magnitude lower than those of conventional oxide glasses.

Temperature-dependent studies of the decay times showed that the energy of the phonons involved in the MPR process agreed well with the maximum phonon energy of hexagonal BaCl<sub>2</sub> (about 250 cm<sup>-1</sup>), which was much lower than the cut-off phonon energy of the glass matrix (about 600 cm<sup>-1</sup>). This indicated that the Nd<sup>3+</sup> ions were incorporated in the low phonon energy hexagonal BaCl<sub>2</sub> nanocrystals leading to the extremely low MPR rates.

The estimated reduced MPR rates described the observed PL enhancement well. For levels with small energy gaps (less than 2,000 cm<sup>-1</sup> to the next lower level), radiative quantum efficiencies that were up to two orders of magnitude higher than those of the standard FZ glass were calculated for the FCZ glass ceramic using the obtained MPR rates. This was in agreement with the enhancement found for the PL quantum efficiency.

Although the MPR rate does not depend on the nanocrystal size, the sample with the smallest nanocrystal size exhibited the highest (about two times higher than in the sample with the largest hexagonal nanocrystals) measured absolute PL quantum efficiency. This was related to the largest total surface area of the nanocrystals in this sample. The nanocrystal surface area increased with decreasing average nanocrystal size, since, in contrast to the nanocrystal size, the volume fraction of the BaCl<sub>2</sub> nanocrystals was found to be similar (about 20 %) in all samples. At the same time, the glass ceramic with the smallest nanocrystals provided the highest transparency quite similar to that of the nanocrystal-free FCZ glass.

Besides neodymium-doped samples, europium-doped FCZ glass ceramics, which are of interest as X-ray scintillators and storage phosphors for medical imaging, were investigated. Routes to determine and to maximize the Eu<sup>2+</sup>-to-Eu<sup>3+</sup> ratio in these glass ceramics being important for the performance of these materials were investigated. The Eu<sup>2+</sup>-to-Eu<sup>3+</sup> ratio was successfully estimated by low temperature Mössbauer spectroscopy. The investigations showed that 20 % more divalent europium can be obtained when using EuCl<sub>2</sub> instead of EuF<sub>2</sub> as a starting material. It was also found that heat treatment in air or an inert atmosphere did not significantly affect the relative Eu<sup>2+</sup> and Eu<sup>3+</sup> contents. Mössbauer linewidth narrowing was observed after the thermal treatment. This indicated that the europium ions moved to a more ordered (crystalline) environment in accordance with the formation of BaCl<sub>2</sub> nanocrystals. Temperature dependent Mössbauer investigations showed that the ratio of the areas of the Mössbauer absorption lines measured at room temperature does not directly correspond to the actual Eu<sup>2+</sup>-to-Eu<sup>3+</sup> ratio present in the sample. For an exact determination, low temperature measurements or corrections with the corresponding *f*-factors are necessary.

The present work shows that FCZ glass ceramics have a general potential for the use as low phonon energy rare-earth host materials providing efficient rare-earth luminescence. Future work should investigate routes to improve the glass quality and to realize a well controlled crystallization. Also other treatment procedures like sintering should be considered. In addition, it should be examined if or rather under which conditions rare-earths, other than Nd and Eu can be incorporated into the nanocrystals in such glass ceramics. One should try to make a trivalent rare-earth doped FCZ glass-ceramic system for luminescence and lasing devices which are not realizable with conventional fluoride or oxide glasses. For example, such a low MPR loss host material is required for Dy<sup>3+</sup> or Tb<sup>3+</sup>-doped fiber amplifiers; both operate at 1.3 μm, which is an important wavelength for telecommunication applications. A further step towards application would be to minimize scattering losses by reducing the crystallite size and by avoiding any inclusions in the glass. Additionally, the applicability of such glass-ceramic systems for photovoltaics should be evaluated. Upconvert-

## 9. Conclusion and outlook

ing glass layers, doped with appropriate rare-earth ions such as  $\text{Er}^{3+}$  or  $\text{Nd}^{3+}$ , which convert the infrared part of a solar spectrum that cannot be used for electrical power generation above the Si bandgap, may improve the efficiency of Si solar cells. Calculations using the glass ceramic's MPR rates, which can be estimated for individual rare-earth levels from the "energy gap law" obtained in this work, can answer which system requirements (kind and doping level of rare-earth ions, lighting conditions etc.) enable promising upconversion efficiencies in the relevant spectral ranges. Steps towards this goal are currently being taken (see Ref. [107]). Furthermore, attempts to transfer the principles and methods found here to other systems could be worthwhile. The formation or incorporation of low phonon energy nanocrystals may also improve the rare-earth luminescence properties of other glasses or transparent plastics such as oxide glasses or polymethyl-methacrylate providing higher practicability than FZ-based glasses.

## Bibliography

- [1] Bahr, J. and Bunsen, R. *Annal. d. Chem. u. Pharm.* **137**(1), 1–33 (1866).
- [2] Kenyon, A. J. *Prog. Quantum Electron.* **26**(4-5), 225–284 (2002).
- [3] Simpson, J. R. In *Rare-Earth-Doped Fiber Lasers and Amplifiers*, Digonnet, M. J. F., editor, 1–15 (Marcel Dekker, New York, 2001).
- [4] Wojtowicz, A. J. *Nucl. Instr. and Meth. A* **486**, 201–207 (2002).
- [5] Chen, G., Johnson, J. A., Weber, R., Schweizer, S., MacFarlane, D., Woodford, J., and De Carlo, F. *Proc. SPIE* **5745**, 1351–1358 (2005).
- [6] Trupke, T., Green, M. A., and Würfel, P. *J. Appl. Phys.* **92**(7), 4117–4122 (2002).
- [7] Ahrens, B., Löper, P., Goldschmidt, J. C., Glunz, S., Henke, B., Miclea, P. T., and Schweizer, S. *Phys. Status Solidi A* **205**(12), 2822–2830 (2008).
- [8] Henke, B., Ahrens, B., Johnson, J. A., and Miclea, P. T. Schweizer, S. *SPIE Newsroom* , 1–3 (2009).
- [9] Limpert, J., Schreiber, T., and Tünnermann, A. *Encyclopaedia of laser physics and technology* , 1–10 (2010).
- [10] Tick, P. A., Borrelli, N. F., Cornelius, L. K., and Newhouse, M. A. *J. Appl. Phys.* **78**(11), 6367–6374 (1995).
- [11] Johnson, J. A., Schweizer, S., Henke, B., Chen, G., Woodford, J., Newman, P. J., and MacFarlane, D. R. *J. Appl. Phys.* **100**, 034701 (5pp) (2006).
- [12] Johnson, J. A., Schweizer, S., and Lubinsky, A. R. *J. Am. Ceram. Soc.* **90**(3), 693–698 (2007).
- [13] Schweizer, S. *Phys. Stat. Sol. A* **187**(2), 335–393 (2001).
- [14] Williams, G. V. M., Bittar, A., Dotzler, C., Beaudin, A., Varoy, C., and Dunford, C. *Radiat. Meas.* **42**, 899–902 (2007).
- [15] Poulain, M., Poulain, M., Lucas, J., and Brun, P. *Mater. Res. Bull.* **10**(4), 243–246 (1975).

## Bibliography

- [16] Parker, J. M. *Annu. Rev. Mater. Sci.* **19**, 21–41 (1989).
- [17] Aasland, S., Einarsrud, M.-A., and Grande, T. *J. Phys. Chem.* **100**(13), 5457–5463 (1996).
- [18] Aggarwal, I. D. and Lu, G. *Fluoride Glass Fibre Optics*. Academic Press, San Diego, (1991).
- [19] Ahrens, B., Brand, S., Büchner, T., Darr, P., Schönfelder, S., Paßlick, C., and Schweizer, S. *J. Non-Cryst. Solids* **357**, 2264–2267 (2011).
- [20] Schweizer, S., Hobbs, L. W., Secu, M., Spaeth, J.-M., Edgar, A., Williams, G. V. M., and Hamlin, J. *J. Appl. Phys.* **97**, 083522 (8pp) (2005).
- [21] Johnson, J. A., Weber, R., Kolesnikov, A. I., and Schweizer, S. In *Proceedings of IMECE2008, 2008 ASME International Mechanical Engineering Congress and Exposition, October 31 - November 6, 2008, Boston, MA, USA*, 1–6, (2008).
- [22] Henke, B., Keil, P., Paßlick, C., Vogel, D., Rohwerder, M., Wiegand, M.-C., Johnson, J. A., and Schweizer, S. *Mater. Res. Soc. Symp. Proc.* **1262**, (6pp) (2010).
- [23] Paßlick, C., Müller, O., Lützenkirchen-Hecht, D., Frahm, R., Johnson, J. A., and Schweizer, S. *J. Appl. Phys.* **110**, 113527 (5pp) (2011).
- [24] Brackett, E. B., Brackett, T. E., and Sass, R. L. *J. Phys. Chem.* **67**(10), 2132–2135 (1963).
- [25] Haase, A. and Brauer, G. *Z. anorg. allg. Chemie* **441**, 181–195 (1978).
- [26] Ahrens, B., Eisenschmidt, C., Johnson, J. A., Miclea, P. T., and Schweizer, S. *Appl. Phys. Lett.* **92**, 061905 (3pp) (2008).
- [27] Layne, C. B., Lowdermilk, W. H., and Weber, M. J. *Phys. Rev. B* **16**(1), 10–21 (1977).
- [28] Shojiya, M., Takahashi, M., Kanno, R., and Kawamoto, Y. *Appl. Phys. Lett.* **72**(8), 882–884 (1998).
- [29] Riseberg, L. A. and Moos, H. W. *Phys. Rev.* **174**(2), 429–438 (1968).
- [30] Weber, M. J. *Phys. Rev. B* **8**(8), 54–64 (1973).
- [31] Reisfeld, R. *Structure and Bonding*, volume 22, chapter Radiative and Non-Radiative Transitions of Rare-Earth Ions in Glasses, 123–175. Springer, Berlin (1975).
- [32] Riseberg, L. A. and Weber, M. J. In *Progress in Optics*, Wolf, E., editor, 91–162 (North-Holland Publishing Co., Amsterdam, 1976).

- [33] Beck, H. P. *J. Solid State Chem.* **47**(3), 328–332 (1983).
- [34] Carnall, W. T., Goodman, G. L., Rajnak, K., and Rana, R. S. *J. Chem. Phys.* **90**(7), 3443–3457 (1989).
- [35] van Vleck, J. H. *J. Phys. Chem.* **41**(1), 67 (1937).
- [36] Judd, B. R. *Phys. Rev.* **127**(3), 750–761 (1962).
- [37] Ofelt, G. S. *J. Chem. Phys.* **37**, 511–520 (1962).
- [38] Reisfeld, R. and Jorgensen, C. K. In *Handbook on the physics and chemistry of rare-earths*, Gschneider, K. A. and Eyring, L., editors, volume 9, 1–90 (Elsevier Science Publishers, Amsterdam, 1987).
- [39] Shinn, M. D., Sibley, W. A., Drexhage, M. G., and Brown, R. N. *Phys. Rev. B* **27**(11), 6635–6648 (1983).
- [40] Kiel, A. In *Quantum electronics*, Grivet, P. and N., B., editors, 765–777 (Columbia U. P., New York, 1964).
- [41] Reisfeld, R. In *Radiationless Processes*, Di Bartolo, B. and Goldberg, V., editors, 489–545 (Plenum Press, New York, 1980).
- [42] Sadoc, A., Guillo, R., and Kastler, A. *C. R. Acad. Sc., Série B* **273**, 203–206 (1971).
- [43] Orlovskii, Y. V., Basiev, T. T., Pukhov, K. K., Doroshenko, M. E., Badikov, V. V., Badikov, D. V., Alimov, O. K., Polyachenkova, M. V., Dmitruk, L. N., Osiko, V. V., and Mirov, S. B. *Opt. Mater.* **29**(9), 1115–1128 (2007).
- [44] Loudon, R. *Adv. in Phys.* **13**(52), 423–482 (1964).
- [45] Long, D. A. *Raman-Spectroscopy*. McGraw-Hill, New York, (1977).
- [46] <http://www.abinit.org>; last accessed: 02/19/2014.
- [47] Gonze, X., Amadon, B., Anglade, P.-M., Beuken, J.-M., Bottin, F., Boulanger, P., Bruneval, F., Caliste, D., Caracas, R., Côté, M., Deutsch, T., Genovese, L., Ghosez, P., Giantomassi, M., Goedecker, S., Hamann, D. R., Hermet, P., Jollet, F., Jomard, G., Leroux, S., Mancini, M., Mazevet, S., Oliveira, M. J. T., Onida, G., Pouillon, Y., Rangel, T., Rignanese, G.-M., Sangalli, D., Shaltaf, R., Torrent, M., Verstraete, M. J., Zerah, G., and Zwanziger, J. W. *Computer Phys. Commun.* **180**, 2582–2615 (2009).
- [48] Bohley, C., Wagner, J.-M., Pfau, C., Miclea, P.-T., and Schweizer, S. *Phys. Rev. B* **83**, 024107 (6pp) (2011).

## Bibliography

- [49] Veithen, M., Gonze, X., and Ghosez, P. *Phys. Rev. B* **71**, 125107 (14pp) (2005).
- [50] Holzwarth, U. and Gibson, N. *Nat. Nanotechnol.* **6**(9), 534–534 (2011).
- [51] Scherrer, P. *Nachr. Ges. Wiss. Göttingen* **2**, 98–100 (1918).
- [52] Langford, J. I. and Wilson, A. J. C. *J. Appl. Cryst.* **11**, 102–113 (1978).
- [53] Pfau, C., Bohley, C., Miclea, P. T., and Schweizer, S. *J. Appl. Phys* **109**, 083545 (6pp) (2011).
- [54] Drexhage, M. G., El-Bayoumi, O. H., and Moynihan, C. T. *Proc. of SPIE* **0320**, 1–7 (1982).
- [55] Fujiura, K., Hoshino, K., Kanamori, T., Nishida, Y., Ohishi, Y., and Sudo, S. In *Technical Digest of Optical Amplifiers and Their Applications*, 104–107 (Optical Society of America, Washington DC, 1995).
- [56] Baró, M. D., Otero, A., Suriñach, S., Jha, A., Jordery, S., Poulain, M., Soufiane, A., Hewak, D. W., Taylor, E. R., and Payne, D. N. *Mater. Sci. Eng.* **A179-180**, 303–308 (1994).
- [57] Baricco, M., Battezzati, L., Braglia, M., Cocito, G., Kraus, J., and Modone, E. *J. Non-Cryst. Solids* **161**, 60–65 (1993).
- [58] Ahrens, B. *Down- and Up-Conversion in Fluorozirconate-Based Glasses and Glass Ceramics for Photovoltaic Application*. PhD thesis, University of Paderborn, (2009).
- [59] Hruby, A. *Czech. J. Phys. B* **22**, 1187–1193 (1972).
- [60] Edgar, A., Schweizer, S., Assmann, S., Spaeth, J. M., Newman, P. J., and MacFarlane, D. R. *J. Non-Cryst. Solids* **284**, 237–242 (2001).
- [61] Harrison, M. T. and Denning, R. G. *J. Lumin.* **69**, 265–285 (1996).
- [62] Gloriant, T., Gich, M., Suriñach, S., Baró, M., and Greer, A. L. *J. Metastab. Nanocryst.* **8**, 365–370 (2000).
- [63] Liu, G. and Eick, H. A. *J. Less-Common Met* **149**, 47–53 (1989).
- [64] Henke, B., Ahrens, B., Miclea, P. T., Eisenschmidt, C., Johnson, J. A., and Schweizer, S. *J. Non-Cryst. Solids* **355**, 1916–1918 (2009).
- [65] Paßlick, C., Ahrens, B., Henke, B., Johnson, J. A., and Schweizer, S. *J. Non-Cryst. Solids* **357**, 2450–2452 (2011).
- [66] Holleman, A. F. and Wiberg, N. *Lehrbuch der Anorganischen Chemie*. de Gruyter, Berlin, (2007).

- [67] Pfau, C., Skrzypczak, U., Miclea, M., Bohley, C., Miclea, P. T., and Schweizer, S. *Mater. Res. Soc. Symp. Proc.* **1404**, (6pp) (2012).
- [68] Pfau, C., Skrzypczak, U., Ahrens, B., and Schweizer, S. *J. Phys.: Condens. Matter* **26**, 025406 (10pp) (2014).
- [69] Binnemans, K., Verboven, D., Görrler-Walrand, C., Lucas, J., Duhamel-Henry, N., and Adam, J. L. *J. Non-Cryst. Solids* **204**(2), 178–187 (1996).
- [70] Samek, L., Wasylak, J., and Marczuck, K. *J. Non-Cryst. Solids* **140**, 243–248 (1992).
- [71] Orlovskii, Y. V., Basiev, T. T., Vorob'ev, I. N., Osiko, V. V., Papashvili, A. G., and Prokhorov, A. M. *Laser Phys.* **6**(3), 448–455 (1996).
- [72] Skrzypczak, U., Pfau, C., Bohley, C., Seifert, G., and Schweizer, S. *J. Phys. Chem. C* **117**(20), 10630–10635 (2013).
- [73] Lucas, J. and Adam, J. L. *Glastech. Ber.* **62**(12), 422–441 (1989).
- [74] Auzel, F. and Pelle, F. *Proc. SPIE* **3416**, 74–82 (1998).
- [75] Yardley, J. T. *Introduction to molecular Energy Transfer*. Academic Press, New York, (1980).
- [76] Pfau, C., Miclea, P. T., Bohley, C., and Schweizer, S. *IOP Conf. Ser.: Mater. Sci. Eng.* **15**, 012021 (5pp) (2010).
- [77] Monberg, E. M. and Nicol, M. *J. Chem. Phys.* **60**(12), 5054–5056 (1974).
- [78] Almeida, R. M. and Mackenzie, J. D. *J. Chem. Phys.* **74**, 5954–5961 (1981).
- [79] Qin, L., Shen, Z. X., Low, B. L., Lee, H. K., Lu, T. J., Dai, Y. S., Tang, S. H., and Kuok, M. H. *J. Raman Spectrosc.* **28**(7), 495–499 (1997).
- [80] Almeida, R. M. and Mackenzie, J. *J. Non-Cryst. Solids* **51**(2), 187–199 (1982).
- [81] Pfau, C., Paßlick, C., Gray, S. K., Johnson, C. A., A., J. J., and Schweizer, S. *J. Phys.: Condens. Matter* **25**(2013), 205402 (6pp) (2013).
- [82] Grandjean, F. and Long, G. J. In *Mössbauer Spectroscopy Applied to Inorganic Chemistry*, Long, G. J. and Grandjean, F., editors, volume 3 (Plenum Press, New York, 1989).
- [83] Weber, J. K. R., Vu, M., Paßlick, C., Schweizer, S., Brown, D. E., Johnson, C. E., and Johnson, J. A. *J. Phys.: Condens. Matter* **23**, 495402 (6pp) (2011).

## Bibliography

- [84] Henke, B., Paßlick, C., Keil, P., Johnson, J. A., and Schweizer, S. *J. Appl. Phys.* **106**, 113501 (6pp) (2009).
- [85] Frauenfelder, H. *The Mössbauer effect: a review with a collection of reprints (Frontiers in physics: a lecture note and reprint series)*. Benjamin, New York, (1963).
- [86] Coey, J. M. D., McEvoy, A., and Shafer, M. W. *J. Non-Cryst. Solids* **43**(3), 387–392 (1981).
- [87] Furuuchi, F., Wakeshima, M., and Hinatsu, Y. *J. Solid State Chem.* **177**, 3853–3858 (2004).
- [88] Dunning, J. W. and Smith, A. L. *Particle Growth in Suspension*. Academic Press, London, (1973).
- [89] Skrzypczak, U., Pfau, C., Bohley, C., Seifert, G., and Schweizer, S. *J. Non-Cryst. Solids* **363**, 205–208 (2013).
- [90] Alvarez, C. J., Liu, Y., Leonard, R. L., Johnson, J. A., and Petford-Long, A. K. *J. Am. Ceram. Soc.* **96**(11), 3617–3621 (2013).
- [91] Rolo, A. G. and Vasilevskiy, M. I. *J. Raman Spectrosc.* **38**, 618–633 (2007).
- [92] Campbell, I. H. and Fauchet, P. M. *Solid State Commun.* **58**(10), 739–741 (1986).
- [93] Arora, A. K., Rajalakshmi, M., Ravindran, T. R., and Sivasubramanian, V. *J. Raman Spectrosc.* **38**, 604–617 (2007).
- [94] McLaughlan, S. D. *Phys. Rev.* **160**(2), 287–289 (1967).
- [95] Weber, M. J. and Bierig, R. W. *Phys. Rev.* **134**(6A), 492–503 (1964).
- [96] Feofilov, S. P. *Phys. Solid State* **44**(8), 1407–1414 (2002).
- [97] Zhang, L., Gan, F., and Wang, P. *Appl. Opt.* **33**(1), 50–56 (1994).
- [98] Li, H. H. *J. Phys. Chem. Ref. Data* **9**(1), 161–289 (1980).
- [99] Soga, K., Inoue, H., and Makishima, A. *J. Lumin.* **55**(1-2), 17–24 (1993).
- [100] Wang, Y. and Ohwaki, J. *Appl. Phys. Lett.* **63**(24), 3268–3270 (1993).
- [101] Chen, D., Wang, Y., Yu, Y., and Hu, Z. *Mater. Sci.* **123**, 1–6 (2005).
- [102] Dejneka, M. J. *J. Non-Cryst. Solids* **239**(1-3), 149–155 (1998).
- [103] Oishi, H., Benino, Y., and Komatsu, T. *Phys. Chem. Glasses* **40**(4), 212–218 (1999).

- [104] Hewak, D. W., Samson, B. N., Medeiros Neto, J. A., Laming, R. I., and Paine, D. N. *Electron. Lett.* **30**(12), 968–969 (1994).
- [105] Dejneka, M. J. *MRS Bulletin* **23**(11), 57–62 (1998).
- [106] Shojiya, M., Takahashi, M., Kanno, R., Kawamoto, Y., and Kadono, K. *J. Appl. Phys.* **82**(12), 6259 (1997).
- [107] Skrzypczak, U. *Rate equation analysis of nanocrystal-enhanced upconversion in neodymium-doped glasses*. PhD thesis, Martin Luther University Halle-Wittenberg, (in progress).



## A. Publications

- (1) C. Pfau, P. T. Miclea, C. Bohley, and S. Schweizer  
*Phonon spectra of barium halide nanocrystals in fluorozirconate glasses*  
IOP Conf. Ser.: Mater. Sci. Eng. **15**, 012021 (5pp) (2010)
- (2) C. Pfau, C. Bohley, P. T. Miclea, and S. Schweizer  
*Structural phase transitions of barium halide nanocrystals in fluorozirconate glasses studied by Raman spectroscopy*  
J. Appl. Phys. **109**, 083545 (6pp) (2011)
- (3) C. Bohley, J.-M. Wagner, C. Pfau, P. T. Miclea, and S. Schweizer  
*Raman spectra of barium halides in orthorhombic and hexagonal symmetry: An ab initio study*  
Phys. Rev. B **83**, 024107 (6pp) (2011)
- (4) C. Pfau, U. Skrzypczak, M. Miclea, C. Bohley, P. T. Miclea, and S. Schweizer  
*Low phonon energy BaCl<sub>2</sub> nanocrystals in Nd<sup>3+</sup>-doped fluorozirconate glasses and their influence on the photoluminescence properties*  
Mater. Res. Soc. Symp. Proc. **1404**, (6pp) (2012)
- (5) U. Skrzypczak, C. Pfau, C. Bohley, G. Seifert, and S. Schweizer  
*Particle size monitoring of BaCl<sub>2</sub> nanocrystals in fluorozirconate glasses*  
J. Non-Cryst. Solids **363**, 205-208 (2013)
- (6) U. Skrzypczak, C. Pfau, C. Bohley, G. Seifert, and S. Schweizer  
*Judd-Ofelt calculations for Nd<sup>3+</sup>-doped fluorozirconate-based glasses and glass ceramics*  
Dataset Papers in Physics **2013**, 236421 (4pp) (2013)
- (7) C. Pfau, C. Paßlick, S. K. Gray, C. A. Johnson, J. A. Johnson, and S. Schweizer  
*Mössbauer spectroscopy of europium-doped fluorochlorozirconate glasses and glass ceramics: optimization of storage phosphors in computed radiography*  
J. Phys.: Condens. Matter **25**, 205402 (6pp) (2013)

## A. Publications

- (8) M. Dyrba, S. Krause, C. Pfau, P. T. Miclea, and S. Schweizer  
*Samarium fluorescence efficiency in high mass density borate glasses*  
Radiat. Meas. **56**, 36-39 (2013)
  
- (9) U. Skrzypczak, C. Pfau, C. Bohley, G. Seifert, and S. Schweizer  
*Influence of BaCl<sub>2</sub> Nanocrystal Size on the Optical Properties of Nd<sup>β+</sup> in Fluorozirconate Glass*  
J. Phys. Chem. C **117**, 10630-10635 (2013)
  
- (10) C. Pfau, U. Skrzypczak, B. Ahrens, and S. Schweizer  
*Multiphonon relaxation in rare-earth doped fluorozirconate-based glasses containing BaCl<sub>2</sub> nanocrystals*  
J. Phys.: Condens. Matter **26**, 025406 (10pp) (2014)
  
- (11) S. Krause, C. Pfau, M. Dyrba, P. T. Miclea, and S. Schweizer  
*On the role of the network modifier PbO in Sm<sup>3+</sup>-doped borate glasses*  
J. Lumin. **151**, 29-33 (2014)
  
- (12) U. Skrzypczak, C. Pfau, G. Seifert, and S. Schweizer  
*Comprehensive rate equation analysis of upconversion luminescence enhancement due to BaCl<sub>2</sub> nanocrystals in neodymium doped fluorozirconate-based glass ceramics*  
J. Phys. Chem. C **118**, 13087-13098 (2014)
  
- (13) U. Skrzypczak, C. Pfau, G. Seifert, and S. Schweizer  
*Rate equation analysis of nanocrystal-enhanced upconversion in neodymium-doped glass ceramics*  
Proc. SPIE, Photonics for Solar Energy Systems V, **9140**, 1-4 (2014)
  
- (14) C. Pfau, U. Skrzypczak, M. Miclea, G. Seifert, B. Ahrens, and S. Schweizer  
*Low phonon energy fluorozirconate-based glass ceramics for efficient rare-earth luminescence*  
Conference paper, Conference on Lasers and Electro-Optics CLEO, JTh2A.60, 1-3 (2014)

## Talks and posters presented at conferences

- (1) C. Pfau, P. T. Miclea, and S. Schweizer  
talk: *Raman spectroscopy on barium halide nanoparticles in fluorozirconate-based glasses*  
Condensed Matter Division of the German Physical Society DPG  
(Regensburg, Germany, March 2010).
- (2) C. Pfau, P. T. Miclea, and S. Schweizer  
talk: *Phonon spectra of barium halide nanocrystals in fluorozirconate glasses*  
11th Europhysical Conference on Defects in Insulating Materials  
EURODIM (Pécs, Hungary, July 2010).
- (3) C. Pfau, C. Bohley, M. Miclea, P. T. Miclea, and S. Schweizer  
talk: *Multi-phonon relaxation in Eu-doped fluorozirconate-based glasses and glass ceramics*  
Condensed Matter Division of the German Physical Society DPG  
(Dresden, Germany, March 2011).
- (4) C. Pfau, U. Skrzypczak, M. Miclea, P. T. Miclea, C. Bohley, and S. Schweizer  
talk: *Low phonon energy BaCl<sub>2</sub> nanocrystals in Nd<sup>3+</sup>-doped fluorozirconate glasses and their influence on the photoluminescence properties*  
Materials Research Society MRS Fall Meeting  
(Boston, USA, November/December 2011).
- (5) U. Skrzypczak, C. Pfau, C. Bohley, and S. Schweizer  
poster: *Optical properties of Nd<sup>3+</sup> in ZBLAN containing BaCl<sub>2</sub> nanocrystals of different sizes*  
8th International Conference on Luminescent Detectors and Transformers for Ionizing Radiation LUMDETR  
(Halle, Germany, September 2012).
- (6) M. Dyrba, S. Krause, C. Pfau, P. T. Miclea, and S. Schweizer  
talk: *Samarium fluorescence efficiency in high mass density borate glasses*  
8th International Conference on Luminescent Detectors and Transformers for Ionizing Radiation LUMDETR  
(Halle, Germany, September 2012).

## A. Publications

- (7) U. Skrzypczak, C. Pfau, G. Seifert, and S. Schweizer  
poster: *Rate equation analysis of nanocrystal-enhanced upconversion in neodymium-doped glass ceramics*  
International Society for Optics and Photonics SPIE Photonics Europe  
(Brussels, Belgium, April 2014).
  
- (8) C. Pfau, U. Skrzypczak, M. Miclea, G. Seifert, B. Ahrens, and S. Schweizer  
poster: *Low phonon energy fluorozirconate-based glass ceramics for efficient rare-earth luminescence*  
Conference on Lasers and Electro-Optics CLEO  
(San Jose, USA, June 2014).

## B. Danksagung

An dieser Stelle möchte ich mich bei allen herzlich bedanken, die zum Gelingen dieser Arbeit beigetragen haben. Im Laufe der Promotionszeit bin ich einigen interessanten und besonderen Menschen begegnet, denen mein herzlicher Dank für die gemeinsame Zeit gilt.

Die vorliegende Arbeit wurde am Zentrum für Innovationskompetenz ZIK SiLi-nano angefertigt. Für die Möglichkeit hierzu danke ich vor allem Prof. Dr. Stefan Schweizer, PD Dr. Gerhard Seifert und Prof. Dr. Ralf B. Wehrspohn.

Den thematischen Anstoß für diese Arbeit gab Prof. Dr. Stefan Schweizer, dem ich für die die nötigen Freiheiten, die er mir als Betreuer gegeben hat, danke. Desweiteren danke ich ihm für die stete und kompetente fachliche Unterstützung und Zusammenarbeit, die Herstellung von wichtigen wissenschaftlichen Kontakten und für seinen Beitrag zu meiner beruflichen und persönlichen Weiterentwicklung.

Außerdem danke ich PD Dr. Gerhard Seifert, der die Arbeitsgruppenleitung am ZIK nach dem Ausscheiden von Prof. Dr. Stefan Schweizer übernommen hat, für seine Fairness und seinen stets klugen Rat.

Mein besonderer Dank gilt Dr. Manuela Miclea für ihre stete Hilfsbereitschaft, die vielen aufschlussreichen Diskussionen und die Einweisung ins Laserlabor.

Herzlicher Dank gebührt meinem langjährigen Mitdoktoranden Dr. Christian Paßlick für die ausgezeichnete Büroatmosphäre, die vielen Diskussionen und seine Hilfe bei der ersten Korrektur.

Desweiteren danke ich Dr. Christian Bohley für die computergestützte Simulation der Phononenspektren mittels Dichtefunktionaltheorie.

Ich danke Dr. Vadim Talalaev, von dessen Erfahrungen im Bereich der Photolumineszenzspektroskopie ich sehr profitieren konnte.

Weiterer Dank gilt Dr. Bernd Ahrens und Dr. Paul T. Miclea dafür, dass sie mir bei der Realisierung vieler Messungen mit Rat und Tat zur Seite standen. Außerdem danke ich meinen Mitdoktoranden Marcel Dyrba, Stefan Krause und Ulrich Skrzypczak für die erfolgreiche gemeinsame Bearbeitung verschiedener Forschungsprojekte.

Ich danke auch allen nicht namentlich erwähnten Mitarbeitern, die mich durch ihre Arbeit unterstützt haben, wie verschiedenen Studenten, administrativen und technischen Mitarbeitern sowie dem Team aus der mechanischen und elektronischen Werkstatt der Universität Halle.

Dank gilt auch dem Fraunhofer Institut für Werkstoffmechanik Halle und dem Fraunhofer-Center für Silizium-Photovoltaik für die Kooperation und für die Möglichkeit deren Laboreinrichtungen als Gastwissenschaftlerin zu nutzen.

## *B. Acknowledgment*

Außerdem danke ich Prof. Dr. Jacqueline A. Johnson und ihrer Arbeitsgruppe dafür, dass sie mir zu einem erfolgreichen und unvergesslich schönen Forschungsaufenthalt am University of Tennessee Space Institute UTSI verholfen haben. Prof. Dr. Charles E. Johnson gilt hierbei mein besonderer Dank für die Einführungen in die Mössbauerspektroskopie, die entsprechenden Laboreinweisungen sowie die ausgezeichnete und sehr angenehme wissenschaftliche Zusammenarbeit. Auch für das Aufstöbern von Grammatikfehlern danke ich Sharon Gray, Lee Leonard, Prof. Dr. Jacqueline A. Johnson und Prof. Dr. Charles E. Johnson.

Für die finanzielle Unterstützung meiner Arbeit am Zentrum für Innovationskompetenz ZIK SiLi-nano danke ich dem Bundesministerium für Bildung und Forschung BMBF (Projektnummer 03Z2HN11). Weitere Teile der Arbeit wurden im Rahmen von Projekten der Fraunhofer Gesellschaft FhG (Fraunhofer Attract, Projektnummer 692 034), der National Science Foundation NSF (Projektnummer DMR1001381) und der National Institutes of Health NIH (Projektnummer 5R01EB006145) finanziert.

Großer Dank gilt meinen Freunden Anton, Jette, Tilmann, Lisa, Jana, Micha, Jule und Florian, die mir mit Geselligkeit und freundschaftlicher Unterstützung eine schöne WG-Zeit in Halle ermöglicht und erfolgreich für außeruniversitäre Zerstreuung gesorgt haben.

Insbesondere danke ich meiner Familie, die mir das Physikstudium ermöglicht hat und mir stets Rückhalt gibt.

Zu guter Letzt danke ich Matthias für die vielen Gespräche, seine bedingungslose Unterstützung und dafür, dass er mich glücklich macht.

## C. Lebenslauf

### Persönliche Daten

Name: Charlotte Pfau  
Geburtsdatum: 29. Dezember 1982  
Staatsangehörigkeit: deutsch  
Familienstand: ledig

### Bildungsweg

08/1989 - 07/1993: Besuch der Grundschule Neumarkt in Halle  
08/1993 - 06/2002: Besuch des Thomas-Müntzer-Gymnasiums in Halle  
Abschluss: Abitur  
10/2002 - 12/2008: Studium der Physik an der Universität Leipzig  
Abschluss: Diplom in Physik  
11/2007 - 12/2008: universitätsexterne Diplomarbeit  
am Forschungszentrum Dresden Rossendorf  
12/2008 - 07/2009: Anstellung als wissenschaftliche Hilfskraft  
am Forschungszentrum Dresden Rossendorf  
seit 08/2009: Anstellung als wissenschaftliche Mitarbeiterin  
am Zentrum für Innovationskompetenz SiLi-Nano



## **D. Eidesstattliche Erklärung**

Ich erkläre an Eides statt, dass ich die Arbeit selbstständig und ohne fremde Hilfe verfasst, keine anderen als die von mir angegebenen Quellen und Hilfsmittel benutzt und die den benutzten fremden Werken wörtlich oder inhaltlich entnommenen Stellen als solche kenntlich gemacht habe. Ich erkläre, diese Arbeit weder in gleicher noch in ähnlicher Form an einer anderen wissenschaftlichen Einrichtung zur Erlangung eines akademischen Grades eingereicht zu haben. Hiermit erkläre ich, keine anderweitigen Promotionsversuche unternommen zu haben. Weiterhin erkläre ich, dass ich weder vorbestraft bin noch dass gegen mich Ermittlungsverfahren anhängig sind.

Halle, den 31. Juli 2014

Charlotte Pfau